

IMPROVING TOMOGRAPHIC ESTIMATES OF SUBSURFACE
ELECTROMAGNETIC WAVE VELOCITY OBTAINED FROM
GROUND-PENETRATING RADAR DATA

A DISSERTATION
SUBMITTED TO THE DEPARTMENT OF GEOPHYSICS
AND THE COMMITTEE ON GRADUATE STUDIES
OF STANFORD UNIVERSITY
IN PARTIAL FULFILLMENT OF THE REQUIREMENTS
FOR THE DEGREE OF
DOCTOR OF PHILOSOPHY

James D. Irving
October, 2006

© Copyright by James D. Irving 2007

All Rights Reserved

I certify that I have read this dissertation and that, in my opinion, it is fully adequate in scope and quality as a dissertation for the degree of Doctor of Philosophy.

Rosemary Knight Principal Advisor

I certify that I have read this dissertation and that, in my opinion, it is fully adequate in scope and quality as a dissertation for the degree of Doctor of Philosophy.

Biondo Biondi

I certify that I have read this dissertation and that, in my opinion, it is fully adequate in scope and quality as a dissertation for the degree of Doctor of Philosophy.

Jerry M. Harris

Approved for the University Committee on Graduate Studies.

Abstract

Crosshole ground-penetrating radar (GPR) travel-time tomography is a popular geophysical technique for characterization of the shallow subsurface in environmental applications. With this technique, a critical factor determining the resolution of the velocity images obtained is the angular ray coverage of the subsurface region between the boreholes; when travel-time data representing a narrow range of ray angles are used for the tomographic reconstruction, the resulting images contain undesirable directional smearing. Here, I investigate the problem that, even when the crosshole GPR survey geometry offers the potential for high-resolution imaging due to wide angular ray coverage of the inter-borehole region, two significant issues are commonly encountered when attempting to take advantage of this coverage. First, travel times corresponding to high-angle ray paths are often extremely difficult to pick because of low signal-to-noise ratios in the data. Secondly, even when high-angle travel-time data can be reliably determined, they often appear to be incompatible with the lower-angle data available, and tend to cause strong numerical artifacts when included in inversions.

To address the high-angle picking problem noted above, I develop a method for determining first-break times in crosshole GPR data using cross-correlations. High-quality reference waveforms for this technique are obtained from the data through the stacking of common-ray-angle gathers. To address the incompatibility issue with high-angle data, I first develop finite-difference time-domain (FDTD) numerical modeling

codes that allow for the determination of realistic crosshole GPR antenna current distributions, and the modeling of transmitted and received waveforms in heterogeneous media. Using these codes, I then find that the high-angle incompatibility issue is likely the result of assuming that first-arriving energy always travels directly between the antenna centers; at high transmitter-receiver angles, this energy likely travels between the antenna tips. Using this knowledge, I develop an improved inversion methodology for crosshole GPR data. In addition to inverting for subsurface velocities, I estimate a small number of parameters that describe a travel-time correction curve as a function of ray angle. I then show the successful application of this improved inversion methodology to synthetic crosshole GPR data, and a data set collected at the Boise Hydrogeophysical Research Site.

Acknowledgements

First, I would like to thank my advisor, Dr. Rosemary Knight, for all of her support, advice, and encouragement over the course of my graduate career. Through Rosemary, I have learned much about science, about the importance of keeping in focus the big picture, and I have picked up many tips on how to successfully manage an active research group. More importantly, however, I am grateful to Rosemary for being the major force behind my acquiring a strong environmental conscience over the past few years. Working with her has instilled within me a desire to devote the next stage of my life to helping to solve some of the many environmental problems currently facing our planet.

I would also like to thank the other members of my reading committee, Drs. Jerry Harris and Biondo Biondi, for their helpful suggestions and advice over the course of my doctorate. I have learned much from both of these professors, and numerous conversations with them have shaped much of the research presented in this thesis. Thanks also to Jef Caers and Tapan Mukerji for chairing and serving as an examiner in my Ph.D. defense, respectively.

I have had the pleasure of working with an absolutely wonderful research group at Stanford. Many of these people have become very good friends, and I'm sure that we'll be in contact for years to come. Steve Moysey, Adam Pidlisecky, Kristina Keating, Jeetu Gulati, Vanessa Mitchell, Elliot Grunewald, David Robinson, Inma Lebron-Robinson, Nigel Crook: thanks to all of you for making life in the Environmental

Geophysics Research Group so enjoyable. Thanks also to my friends outside of the research group, who have made my time in California a lot of fun – a challenging task considering the fact that I was living away from my wife. Dave Shelly, Dave Wynn, Kamini Singha, Justin Rubinstein, Bill Curry, Amie Lucier, Hannah Ross, Ellen Mallman, Sang-Ho Yun, and the rest of the SEP group: it’s been great and I very much look forward to meeting up with all of you in the future.

I would also like to thank my family, both immediate and extended. Without the unconditional love, support, and encouragement from my parents, Doug and Sharon Irving, I would not be here today. They are wonderful role models, and I am forever grateful for the stable, loving upbringing that they provided. I am also extremely lucky to have a fantastic set of in-laws, Keith and Sheila Hipel, who have been a constant source of encouragement... and beer... throughout this degree.

Last, and most importantly, I would like to thank my wife, Melita. Completing this degree has been a challenge, not as much academically as personally because we lived largely apart during the time I spent at Stanford. Marrying Melita is, in short, the best thing that ever happened in my life, and I can’t express how much I appreciate her ‘holding on’ while we both finished our doctorates and looked forward to living together full-time again. Without her love and support, none of this would have been possible.

The research in this dissertation was supported by funding from the National Science Foundation, Grant Number EAR-0229896-002. I was also supported for one year during my doctorate by a Departmental Chair’s Fellowship at Stanford University.

Contents

Abstract	v
Acknowledgements	vii
1 Thesis overview	1
1.1 Motivation	1
1.2 Summary of research	4
2 Numerical modeling of GPR in 2-D using MATLAB	9
2.1 Abstract	9
2.2 Introduction	10
2.3 Theory	12
2.3.1 Governing equations	12
2.3.2 Finite-difference approximations	15
2.3.3 Numerical stability and dispersion criteria	19
2.3.4 PML absorbing boundaries	20
2.4 MATLAB implementation	22
2.5 Examples	24
2.6 Conclusions	34
3 Simulation of antenna transmission and reception for crosshole GPR	35

3.1	Abstract	35
3.2	Introduction	36
3.3	Development of the modeling algorithm	38
3.3.1	FDTD modeling in 2-D cylindrical coordinates	38
3.3.2	Simulation of antenna transmission and reception	40
3.3.3	Examples for standing-wave and Wu-King dipole antennas	46
3.3.4	Behavior of the antenna current for crosshole GPR	50
3.4	Comparison with analytical, numerical, and field results	54
3.5	Conclusions	58
4	Effect of antennas on crosshole GPR velocity estimates	61
4.1	Abstract	61
4.2	Introduction	62
4.3	Velocity along a borehole GPR antenna	63
4.4	Crosshole GPR modeling results	66
4.4.1	Homogeneous medium	66
4.4.2	Heterogeneous medium	69
4.5	Conclusions	71
5	Strategies for improving crosshole GPR travel-time tomography at close borehole spacings	73
5.1	Abstract	73
5.2	Introduction	74
5.3	Cross-correlation picking of travel times	77
5.4	Incompatibility of high-angle data	86
5.5	Improved inversion procedure	94
5.6	Examples	97
5.6.1	Synthetic data	97

5.6.2	BHRS field data	102
5.7	Conclusions	106
6	Directions for future research	111

List of Figures

2.1	Spatial arrangement of H_x , H_z , and E_y field components for TM-mode modeling	16
2.2	Examples of Blackman-Harris pulses fed into grid as sources in our FDTD modeling codes	23
2.3	Flowchart of FDTD modeling procedure	25
2.4	Electrical property model used for TM-mode reflection GPR example	26
2.5	Snapshots showing amplitude of E_y wavefield at different times during TM-mode FDTD modeling	28
2.6	Common-source gather for source located at $x = 10$ m, $z = 0$ m in Figure 2.4	29
2.7	Common-offset gather for TM-mode reflection GPR modeling example	30
2.8	Subsurface velocity model used for TE-mode crosshole GPR example	31
2.9	Snapshots showing amplitude of E_z wavefield at different times during TE-mode FDTD modeling	32
2.10	Common-source gather for source located at $x = 0.5$ m, $z = 5$ m in Figure 2.8	33
2.11	Straight-ray velocity tomogram obtained from synthetic crosshole data created using our TE-mode code	33
3.1	Basic schematic of a crosshole GPR experiment	42

3.2	Normalized antenna current impulse response, $A(z, t)$, for a 2-m-long, bare-wire, standing-wave dipole antenna embedded in a lossless $\kappa = 9$ medium	44
3.3	Radiated E_z field and received waveform determined for 2-m-long, standing-wave dipole antennas in a lossless $\kappa = 9$ medium	48
3.4	Radiated E_z field and received waveform determined for 2-m-long, resistively loaded (Wu-King) dipole antennas in a lossless, $\kappa = 9$ medium	49
3.5	Modeling domain used to determine the behavior of the current on a realistic borehole GPR antenna	52
3.6	Normalized transmitter antenna current for an insulated, 2-m-long, dipole antenna located in a 5-cm-diameter, air-filled borehole and surrounded by earth having $\kappa_{med} = 9$ and $\sigma_{med} = 1$ mS/m	53
3.7	Comparison of received waveforms computed using our approach and determined analytically using the method of Sato and Thierbach (1991)	55
3.8	Comparison of radiated E_z field computed using our approach and using finely discretized FDTD code with the transmitter antenna and borehole explicitly modeled	57
3.9	Comparison of received waveforms modeled using our approach and recorded in the field in an unsaturated sand-and-gravel aquifer deposit	59
4.1	Antenna-to-medium velocity ratio (v_{ant}/v_{med}) determined versus borehole diameter for a number of cases in the vadose and saturated zones	65
4.2	Velocity error versus transmitter-receiver angle determined from numerical simulations of finite antennas in a homogeneous medium having $\kappa = 25$	68
4.3	Heterogeneous medium example	70

5.1	Common-receiver gather showing the difficulties in picking first-break times at large transmitter-receiver offsets due to low S/N	78
5.2	Flowchart of our cross-correlation picking procedure	80
5.3	Common-ray-angle gather and mean trace for the 65 to 70 degree angle range in the BHRS data set	82
5.4	Mean traces determined for the BHRS data set by stacking the different common-ray-angle gathers	83
5.5	Four common-receiver gathers from the BHRS data set showing the results of our automatic picking procedure	85
5.6	Velocity-versus-angle plot for the BHRS field data set	86
5.7	Assumed and proposed travel paths of first-arriving energy at high transmitter-receiver angles	89
5.8	Geometrically determined velocity-versus-angle plot for the case where $v_{ant} > v_{med}$	90
5.9	Example waveform gathers and velocity-versus-angle plots for the case of short and long transmitter feed pulses	91
5.10	Example waveform gathers and velocity-versus-angle plots comparing the non-dispersive case from Figure 5.9 with the case of constant $Q = 15$ dispersion	94
5.11	Results of applying our modified inversion strategy to synthetic data	98
5.12	Angle-dependent travel-time correction parameters obtained in the inversion of the synthetic data in Figure 5.11d	102
5.13	Results of applying our modified inversion strategy to the field data set collected at the BHRS	103
5.14	Angle- and receiver-position-dependent travel-time corrections obtained in the inversion of the BHRS data in Figure 5.13d	107

Chapter 1

Thesis overview

1.1 Motivation

Groundwater is a precious resource that is being increasingly threatened around the world by contamination from human activities. In order to protect this resource, it is crucial that we develop effective and cost-efficient strategies for groundwater remediation in contaminated regions, and also strategies to avoid future contamination in areas where problems do not yet exist. A critical part of developing such strategies is the creation of numerical models for groundwater flow and contaminant transport. With these models, the potential impacts of human activities on groundwater resources can be examined, and the effectiveness of proposed remediation strategies can be evaluated before their implementation.

One key aspect of designing accurate numerical flow and transport models in a region is the adequate characterization of subsurface spatial heterogeneity. It is now well understood that, above and below the water table, this heterogeneity has a profound effect on the way that contaminants travel and spread, with the scale of heterogeneity that is most important being related to the scale of the flow phenomena being examined. Unfortunately, traditional methods for the estimation of hydraulic properties

in the subsurface, such as pumping tests and core measurements, are often unable to provide the degree of spatial detail that is required for accurate flow and transport modeling (e.g., Sudicky, 1986). Whereas pumping tests yield only average values of properties over a relatively large region, core measurements provide sparse, 1-D profiles of subsurface geology, and have the added disadvantage of being very costly and invasive. For these reasons, much interest has been shown over the past few years in the use of geophysical methods for subsurface hydrogeological characterization. Because changes in hydraulic and geophysical properties in the subsurface are both closely linked with changes in lithology, these methods offer the hope of providing a relatively cheap and non-invasive means of obtaining spatially dense hydrogeological information.

Ground-penetrating radar (GPR) is one geophysical method that has proven to be a powerful tool for hydrogeological characterization in electrically resistive geological environments. Similar to seismic except using electromagnetic (EM) energy, GPR allows us to learn about the structure of the shallow subsurface from short EM pulses that have traveled through the earth for many different configurations of a transmitter and receiver antenna. As with seismic, GPR surveying can be divided into two main modes of operation: surface-based reflection surveying and crosshole surveying. With surface-based reflection surveying, the most common means of incorporating the data into hydrogeological models is through a radar facies approach (e.g., Asprion and Aigner, 1999; Beres et al., 1999; Lesmes et al., 2002; McMechan et al., 2002; Moysey et al., 2003), whereby regions of a common-offset GPR image are distinguished from one another based on their external form and the configuration of their internal reflections, and the resulting radar facies are assumed to correspond to hydrogeologically distinct zones in the subsurface. A significant concern with this approach, however, is that the connection between radar facies and hydraulic properties is often very unclear. For example, how do we assign reasonable values of properties

to radar facies in a hydrogeological model, and how can we be certain that different radar facies represent regions of the subsurface having different hydraulic properties? Further, because a relatively large part of a radar image is often required to identify a particular radar facies, resolution with this technique is somewhat limited. As a result, tomographic radar methods have recently been the subject of much attention from hydrogeologists and hydrogeophysicists. Although more labour intensive than common-offset reflection techniques, these methods can provide high-resolution images of subsurface EM-wave velocity and attenuation, parameters that are strongly correlated with soil water content and clay fraction, respectively. Such estimates can then be used in combination with radar-facies methods to better estimate the hydraulic properties of the different facies, and to assess the degree of spatial variability within those facies. In addition, they allow for the improved processing of the reflection GPR data, such that the various facies boundaries are correctly positioned in the subsurface images obtained.

Both surface reflection and crosshole GPR tomographic methods have been used in recent studies to estimate the spatial distribution of hydraulic properties in the subsurface (e.g., Greaves et al., 1996; Hubbard et al., 1997; Eppstein and Dougherty, 1998; Hubbard et al., 2001; Pipan et al., 2002; Oldenborger et al., 2003; Tronicke et al., 2004). In all of these studies, ray-based tomographic techniques were employed for the simple reason that they are robust and have been proven to be very effective. Although work is currently underway on the application of waveform-based tomographic methods to GPR data (e.g., Ernst and Holliger, 2005), such work is still very preliminary. With all ray-based tomographic techniques, a critical factor that affects the resolution of the images that are obtained is the degree of angular ray coverage of the region under investigation (Menke, 1984; Rector and Washbourne, 1994; Tronicke et al., 2001). Without adequate angular coverage, smearing and ambiguity occur in the resulting tomograms. This dissertation focuses on increasing the angular

coverage available with crosshole GPR travel-time tomography, with the overall goal of obtaining the highest-possible-resolution images of subsurface EM-wave velocity for incorporation into hydrogeological models. More specifically, I address the problem that, although the crosshole GPR survey geometry often offers the potential for excellent angular coverage of the subsurface, a number of practical issues currently prevent us from taking full advantage of this coverage. A significant part of this thesis is devoted to the numerical modeling of GPR data, as such models were necessary to verify a number of hypotheses, and to create synthetic data sets upon which new processing and inversion strategies could be tested.

1.2 Summary of research

The research in this dissertation is divided into four chapters. Each chapter has been prepared as a stand-alone paper for submission to a peer-reviewed scientific journal. Chapters 2 through 4 are published, whereas Chapter 5 is currently in the process of being submitted for publication. For convenience, the references from each chapter have been consolidated and appear at the end of the thesis.

In Chapter 2, I present codes that I have developed for the numerical modeling of crosshole and surface GPR data in two dimensions. As mentioned, numerical models for GPR were required in my research to verify a number of hypotheses, and to create synthetic data sets upon which new processing and inversion strategies could be tested. Disappointingly, despite a considerable number of papers being published on GPR modeling over the past decade, there was a severe lack of corresponding codes available for public use. The major contribution of this research, therefore, is to present to the public a collection of well-commented, open-source, GPR modeling codes that are easy to implement, understand, and modify for the user's specific purpose. Although the focus of this dissertation is on crosshole GPR tomography, codes

were created for modeling both crosshole and surface-based GPR data because the original scope of the thesis included joint crosshole and surface tomographic imaging. The codes are written for the MATLAB environment, and apply the finite-difference time-domain (FDTD) method to Maxwell's curl equations in 2-D Cartesian coordinates to model EM-wave propagation. To prevent reflections at the edges of the modeling grid, the novel perfectly-matched layer (PML) absorbing boundaries (e.g., Berenger, 1994) are implemented, which allow for the almost complete absorption of outward-traveling waves, at any angle of incidence, using a very small number of boundary cells. In addition, although MATLAB is generally regarded as a very slow-running platform for modeling, all possible optimizations in notation were made in the codes so that they are efficient; their run time is actually comparable to C routines that I have written for the same purpose. This chapter (including the MATLAB algorithms) was published in the journal *Computers and Geosciences* (Irving and Knight, 2006a).

Chapter 3 of this thesis again focuses on numerical modeling. Here, however, I develop an efficient and novel means of simulating both antenna transmission and reception for crosshole GPR based on the general modeling concepts described in Chapter 2, but using a 2-D cylindrical (not Cartesian) coordinate system. The motivation behind this research was to investigate a common problem in crosshole GPR tomography: the inability to successfully incorporate high-angle ray data into inversions when the boreholes are spaced closely together. My hypothesis was that this problem is related to the length of the GPR antennas, which is currently ignored in all inversion strategies despite the fact that it often represents a significant fraction of the borehole spacing. To model transmission and reception, I derive an approach that uses a superposition of point-electric-dipole source and receiver responses to emulate realistic antenna current distributions in the boreholes. The major contribution of this research is that it represents the first numerical modeling algorithm that is able

to efficiently and accurately simulate the complete waveforms that are recorded in crosshole GPR surveys. This allows us to fully examine the effects of radar system and antenna details on crosshole GPR measurements (as is done in Chapters 4 and 5), but more importantly, it paves the way for the full-waveform inversion of the data. This chapter was published in the journal *Geophysics* (Irving and Knight, 2006b).

In Chapter 4, I use the antenna modeling algorithm described in Chapter 3 to examine in detail the high-angle-ray issue in crosshole GPR tomography. As mentioned, significant problems are often encountered when attempting to include high-angle ray data into crosshole GPR tomographic inversions. Specifically, the high-angle data often appear to be incompatible with the lower-angle data available, and commonly cause significant numerical artifacts in the resulting tomograms. Here, I investigate the idea that this problem is caused by an assumption that is common to all present crosshole GPR inversion strategies: that first-arriving energy always travels directly between the centers of the antennas. The work in this chapter shows that, at high transmitter-receiver angles, it is very likely that first-arriving energy actually travels via the antenna tips. This chapter was published in the journal *Geophysics* (Irving and Knight, 2005b).

Building on the results of Chapters 3 and 4, Chapter 5 of this thesis introduces two methods by which we can improve the resolution of crosshole GPR tomography at close borehole spacings. Both of these methods work towards increasing the angular ray coverage of the inter-borehole region by allowing the inclusion of high-angle data. First, I present a travel-time picking strategy for crosshole GPR data based on cross-correlations. With this technique, high-angle travel times, which are notoriously difficult to pick due to low signal-to-noise ratios, now become available for incorporation into crosshole GPR inversions. Next, I describe a number of mechanisms that I believe cause the problems experienced with high-angle data in crosshole GPR inversions (one of these being the tip-to-tip coupling issue discussed in Chapter 4).

Using the fact that all of these mechanisms produce errors in measured velocities that vary as a function of transmitter-receiver angle, I then develop an improved inversion methodology that involves estimating, in addition to subsurface velocities, a small number of parameters that describe a travel-time correction curve as a function of angle. The results of this chapter now allow us to successfully make use of the excellent angular coverage provided by close borehole spacings in crosshole GPR tomography, and thus obtain improved resolution tomograms. This chapter is currently in preparation for submission to the journal *Geophysics* (Irving et al., 2006).

Chapter 2

Numerical modeling of GPR in 2-D using MATLAB

2.1 Abstract

We present MATLAB codes for finite-difference time-domain (FDTD) modeling of ground-penetrating radar (GPR) in two dimensions. Surface-based reflection GPR is modeled using a transverse magnetic (TM-) mode formulation. Crosshole and vertical radar profiling (VRP) geometries are modeled using a transverse electric (TE-) mode formulation. Matrix notation is used in the codes wherever possible to optimize them for speed in the MATLAB environment. To absorb waves at the edges of the modeling grid, we implement perfectly matched layer (PML) absorbing boundaries. Although our codes are two dimensional and do not incorporate features such as dispersion in electrical properties, they capture many of the important elements of GPR surveying and run at a fraction of the computational cost of more elaborate algorithms. In addition, the codes are well commented, relatively easy to understand, and can be easily modified for the user's specific purpose.

2.2 Introduction

Ground-penetrating radar (GPR) is a popular geophysical method for high-resolution imaging of the shallow subsurface. The GPR technique can be divided into two main modes of operation: (i) surface-based reflection surveying, where the transmitter and receiver antennas are located on the surface of the earth and the subsurface is imaged in terms of changes in its electrical properties, and (ii) borehole surveying, where one or both antennas are located in boreholes and subsurface properties are estimated tomographically. Of interest in our research is the application of both surface and borehole GPR to hydrogeological problems. Specifically, we are interested in using these techniques to assist in the development of hydrogeological models that predict groundwater flow and contaminant transport. A critical step in using GPR for this purpose is determining the link between the hydrogeological properties that govern these processes, and the information contained in a GPR data set.

Numerical GPR models provide one means of exploring the link between subsurface properties and GPR data. We can create a model of a subsurface region of interest, where we define the subsurface in terms of its lithological or hydrogeological properties. We can then transform this model into one that represents the subsurface in terms of its electrical properties. GPR modeling can then be used to simulate the acquisition of data in this subsurface region. The synthetic data that are obtained can be used to advance our understanding of the way in which information about the spatial variability of subsurface properties is captured by, and can be extracted from, GPR data.

A number of approaches have been presented for the numerical modeling of GPR data. These include ray-based methods (Goodman, 1994; Cai and McMechan, 1995), frequency domain methods (Powers and Olhoeft, 1994; Zeng et al., 1995), integral methods (Ellefsen, 1999), and pseudospectral methods (Carcione, 1996; Casper and

Kung, 1996; Liu and Fan, 1999). What has become by far the most common approach for GPR modeling over the past decade, however, is the finite-difference time-domain (FDTD) technique (e.g., Wang and Tripp, 1996; Bourgeois and Smith, 1996; Bergmann et al., 1996; Teixeira et al., 1998; Holliger and Bergmann, 2002). Reasons for this include that the FDTD approach is relatively conceptually simple, accurate for arbitrarily complex models, and capable of accommodating realistic antenna designs and features such as dispersion in electrical properties (Taflove, 1995). What is lacking, however, are FDTD modeling codes for GPR, freely available for the public use, that are easy to understand and modify.

Here, we present FDTD codes, written in the MATLAB programming language, for basic surface reflection and borehole GPR modeling in two dimensions. Although 2-D modeling is limited in the sense that it cannot fully account for antenna behavior and out-of-plane variations in material properties, our codes capture many of the important features of GPR surveying and run at a fraction of the computational cost of fully 3-D algorithms. The codes feature perfectly matched layer (PML) absorbing boundaries to avoid reflections from the edges of the modeling grid. To optimize the programs for speed in MATLAB, matrix notation is used wherever possible. To begin, we discuss the theory behind our codes, including the governing analytical equations, their finite-difference approximations, numerical stability and dispersion criteria, and boundary conditions. Next, we briefly discuss how the FDTD equations are implemented in the MATLAB environment. Finally, we present two examples of the use of our codes, one showing modeling of a reflection GPR survey, and the other modeling of a crosshole GPR survey.

2.3 Theory

2.3.1 Governing equations

We begin the theory behind our GPR modeling codes with Maxwell's curl equations in the frequency domain, which are:

$$\nabla \times \mathbf{E} = -i\omega\mu\mathbf{H}, \quad (2.1)$$

$$\nabla \times \mathbf{H} = \sigma\mathbf{E} + i\omega\epsilon\mathbf{E}, \quad (2.2)$$

where $i = \sqrt{-1}$, ω is angular frequency, ϵ , μ , and σ are the dielectric permittivity, magnetic permeability, and electrical conductivity parameters, respectively, and \mathbf{E} and \mathbf{H} are the electric and magnetic field vectors. To implement PML absorbing boundaries in our codes, we consider the general case of a complex stretched coordinate space (e.g., Chew and Weedon, 1994; Gedney, 1998), where the ∇ operator takes the following form:

$$\nabla = \hat{x} \frac{1}{s_x} \frac{\partial}{\partial x} + \hat{y} \frac{1}{s_y} \frac{\partial}{\partial y} + \hat{z} \frac{1}{s_z} \frac{\partial}{\partial z}, \quad (2.3)$$

where

$$s_k = \kappa_k + \frac{\sigma_k}{\alpha_k + i\omega\epsilon_0}, \quad k = x, y, z \quad (2.4)$$

are complex coordinate stretching variables that vary only in the k direction (Kuzuoglu and Mittra, 1996). Here, ϵ_0 is the dielectric permittivity of free space, and σ_k, κ_k , and α_k are parameters that can be specified to allow for wave propagation in the interior of the modeling grid and wave absorption in the PML boundary regions. It should be stressed that σ_k , κ_k , and α_k are not true electrical properties. Rather they are parameters that, through complex coordinate stretching, add additional degrees of freedom to Maxwell's equations to allow for PML boundary implementation.

Taking the components of equations (2.1) and (2.2) using the identity in equation (2.3), and assuming that there is no variation in the y direction for 2-D modeling, we arrive at the following two decoupled sets of partial-differential equations involving the $\{H_x, H_z, E_y\}$ and $\{E_x, E_z, H_y\}$ field components:

$$i\omega\mu H_x = -\frac{1}{s_z} \frac{\partial E_y}{\partial z}, \quad (2.5a)$$

$$i\omega\mu H_z = \frac{1}{s_x} \frac{\partial E_y}{\partial x}, \quad (2.5b)$$

$$\sigma E_y + i\omega\epsilon E_y = \frac{1}{s_x} \frac{\partial H_z}{\partial x} - \frac{1}{s_z} \frac{\partial H_x}{\partial z}, \quad (2.5c)$$

and

$$\sigma E_x + i\omega\epsilon E_x = \frac{1}{s_z} \frac{\partial H_y}{\partial z}, \quad (2.6a)$$

$$\sigma E_z + i\omega\epsilon E_z = -\frac{1}{s_x} \frac{\partial H_y}{\partial x}, \quad (2.6b)$$

$$i\omega\mu H_y = \frac{1}{s_z} \frac{\partial E_x}{\partial z} - \frac{1}{s_x} \frac{\partial E_z}{\partial x}. \quad (2.6c)$$

Equations (2.5a-c) and (2.6a-c) are the transverse magnetic (TM-) and transverse electric (TE-) mode sets of equations in the stretched coordinate space, respectively. For surface-based reflection GPR modeling, where the antennas are oriented perpendicular to the $x - z$ survey plane, we use the TM-mode equations. For crosshole and vertical radar profiling (VRP) geometries, where the antennas are contained within the survey plane, the TE-mode equations are employed. It is important to note that, when the stretching parameters are set to unity, equations (2.5a-c) and (2.6a-c) become the standard TM- and TE-mode equations in an unstretched coordinate space. In the interior of the modeling grid, we therefore set $s_x = s_z = 1$. In the PML boundary regions of the grid, however, s_x and s_z are given complex values, which allows significant wave absorption to occur. Unlike in the simpler case of a change in

electrical conductivity in these regions (which would also cause absorption), altering the coordinate stretching variables does not result in a change in electromagnetic (EM) impedance from the interior of the grid, and thus no reflections are created at the edges of the PML domain.

We implement PML absorbing boundaries in our modeling codes using the convolutional PML (CPML) approach of Roden and Gedney (2000). This method makes use of time-domain expressions for $1/s_x$ and $1/s_z$ in the FDTD formulation, and avoids the splitting of the electric and magnetic field components common in other PML approaches (e.g., Berenger, 1994; Fang and Wu, 1996). For this reason, we find the CPML approach to be the most intuitive implementation of PML. Taking the inverse Fourier transform of the inverse of equation (2.4), we have:

$$\begin{aligned} s_k^{-1}(t) &= \frac{\delta(t)}{\kappa_k} - \frac{\sigma_k}{\epsilon_0 \kappa_k^2} \exp \left[-\frac{t}{\epsilon_0} \left(\frac{\sigma_k}{\kappa_k} + \alpha_k \right) \right] u(t) \\ &= \frac{\delta(t)}{\kappa_k} + \zeta_k(t), \end{aligned} \quad (2.7)$$

where $\delta(t)$ is the Dirac delta function and $u(t)$ is the Heaviside step function. Using this expression and assuming frequency-independent material properties, equations (2.5a-c) and (2.6a-c) are transformed into the time domain as follows:

$$\mu \frac{\partial H_x}{\partial t} = -\frac{1}{\kappa_z} \frac{\partial E_y}{\partial z} - \zeta_z(t) * \frac{\partial E_y}{\partial z}, \quad (2.8a)$$

$$\mu \frac{\partial H_z}{\partial t} = \frac{1}{\kappa_x} \frac{\partial E_y}{\partial x} + \zeta_x(t) * \frac{\partial E_y}{\partial x}, \quad (2.8b)$$

$$\sigma E_y + \mu \frac{\partial E_y}{\partial t} = \frac{1}{\kappa_x} \frac{\partial H_z}{\partial x} - \frac{1}{\kappa_z} \frac{\partial H_x}{\partial z} + \zeta_x(t) * \frac{\partial H_z}{\partial x} - \zeta_z(t) * \frac{\partial H_x}{\partial z}, \quad (2.8c)$$

and

$$\sigma E_x + \epsilon \frac{\partial E_x}{\partial t} = \frac{1}{\kappa_z} \frac{\partial H_y}{\partial z} + \zeta_z(t) * \frac{\partial H_y}{\partial z}, \quad (2.9a)$$

$$\sigma E_z + \epsilon \frac{\partial E_z}{\partial t} = -\frac{1}{\kappa_x} \frac{\partial H_y}{\partial x} - \zeta_x(t) * \frac{\partial H_y}{\partial x}, \quad (2.9b)$$

$$\mu \frac{\partial H_y}{\partial t} = \frac{1}{\kappa_z} \frac{\partial E_x}{\partial z} - \frac{1}{\kappa_x} \frac{\partial E_z}{\partial x} + \zeta_z(t) * \frac{\partial E_x}{\partial z} - \zeta_x(t) * \frac{\partial E_z}{\partial x}, \quad (2.9c)$$

where $*$ represents convolution. We now describe how equations (2.8a-c) are approximated using finite-differences in our TM-mode modeling code for GPR reflection profiling. The derivations for the TE-mode modeling code using equations (2.9a-c) are not included here, as they are performed in a nearly identical manner.

2.3.2 Finite-difference approximations

To numerically model equations (2.8a-c), we use a leap-frog, staggered-grid approach that involves offsetting the electric and magnetic field components in both space and time such that the finite-difference approximations of the partial derivatives in each equation are centered on the same spatiotemporal location (Yee, 1966). Figure 2.1 shows the configuration of H_x , H_z , and E_y in space for our TM-mode modeling code. All spatial derivatives are approximated using fourth-order-accurate finite-difference expressions. The time derivatives are approximated with second-order-accurate expressions. This O(2,4) scheme is identical to that described in Bergmann et al. (1996) for 1-D GPR modeling. The conduction current density term in equation (2.8c) is modeled using a semi-implicit approximation (e.g., Taflove, 1995, p. 64), which has been shown to have superior numerical properties over one-sided expressions for this term (Bergmann et al., 1996).

After substituting the appropriate finite-difference expressions into equations (2.8a-c) and solving for the updated electric and magnetic field components, we arrive at

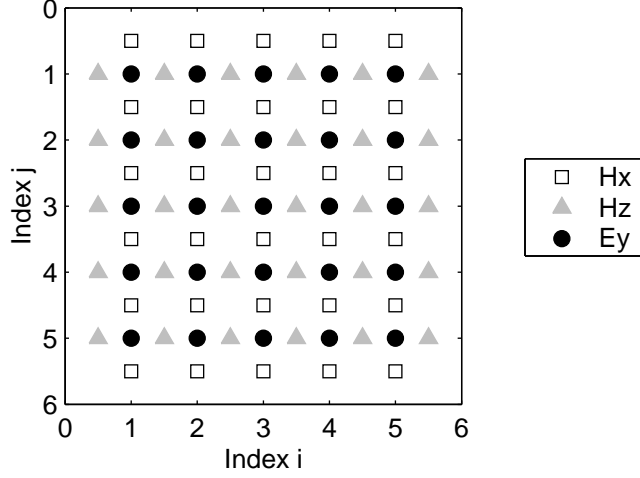


Figure 2.1: Spatial arrangement of H_x , H_z , and E_y field components for TM-mode modeling. Electric and magnetic field components are also staggered in time by $\Delta t/2$.

the following FDTD update equations:

$$\begin{aligned}
H_x|_{i,j+1/2}^{n+1/2} &= H_x|_{i,j+1/2}^{n-1/2} \\
&\quad - D_{b_z}|_{i,j+1/2} \left[-E_y|_{i,j+2}^n + 27E_y|_{i,j+1}^n - 27E_y|_{i,j}^n + E_y|_{i,j-1}^n \right] \\
&\quad - D_c|_{i,j+1/2} \left[\Psi_{H_{xz}}|_{i,j+1/2}^n \right], \tag{2.10a}
\end{aligned}$$

$$\begin{aligned}
H_z|_{i+1/2,j}^{n+1/2} &= H_z|_{i+1/2,j}^{n-1/2} \\
&\quad + D_{b_x}|_{i+1/2,j} \left[-E_y|_{i+2,j}^n + 27E_y|_{i+1,j}^n - 27E_y|_{i,j}^n + E_y|_{i-1,j}^n \right] \\
&\quad + D_c|_{i+1/2,j} \left[\Psi_{H_{zx}}|_{i+1/2,j}^n \right], \tag{2.10b}
\end{aligned}$$

$$\begin{aligned}
E_y|_{i,j}^{n+1} &= C_a|_{i,j} \left[E_y|_{i,j}^n \right] \\
&\quad + C_{b_x}|_{i,j} \left[-H_z|_{i+3/2,j}^{n+1/2} + 27H_z|_{i+1/2,j}^{n+1/2} - 27H_z|_{i-1/2,j}^{n+1/2} + H_z|_{i-3/2,j}^{n+1/2} \right] \\
&\quad - C_{b_z}|_{i,j} \left[-H_x|_{i,j+3/2}^{n+1/2} + 27H_x|_{i,j+1/2}^{n+1/2} - 27H_x|_{i,j-1/2}^{n+1/2} + H_x|_{i,j-3/2}^{n+1/2} \right] \\
&\quad + C_c|_{i,j} \left[\Psi_{E_{yx}}|_{i,j}^{n+1/2} - \Psi_{E_{yz}}|_{i,j}^{n+1/2} \right], \tag{2.10c}
\end{aligned}$$

where the subscripts indicate spatial position, and the superscripts indicate time (i.e., $H_x|_{i,j+1/2}^{n+1/2}$ represents the H_x field component at position $(x, z) = (i\Delta x, (j + 1/2)\Delta z)$ and time $t = (n + 1/2)\Delta t$, where Δx and Δz are the horizontal and vertical field discretization intervals, and Δt is the time step). FDTD modeling using these equations is accomplished by alternately updating the electric and magnetic fields. This moves forward in time since the two fields are temporally staggered by $\Delta t/2$. As can be seen from the equations, all field updates are fully explicit.

The update coefficients C_a , C_{b_x} , C_{b_z} , C_c , D_{b_x} , D_{b_z} , and D_c in equations (2.10a-c) are given in terms of the electrical properties and grid parameters as follows:

$$C_a = \left(1 - \frac{\sigma\Delta t}{2\epsilon}\right) \left(1 + \frac{\sigma\Delta t}{2\epsilon}\right)^{-1}, \quad (2.11a)$$

$$C_{b_k} = \frac{\Delta t}{\epsilon} \left(1 + \frac{\sigma\Delta t}{2\epsilon}\right)^{-1} (24\kappa_k\Delta k)^{-1}, \quad (2.11b)$$

$$C_c = \frac{\Delta t}{\epsilon} \left(1 + \frac{\sigma\Delta t}{2\epsilon}\right)^{-1}, \quad (2.11c)$$

$$D_{b_k} = \frac{\Delta t}{\mu} (24\kappa_k\Delta k)^{-1}, \quad (2.11d)$$

$$D_c = \frac{\Delta t}{\mu}. \quad (2.11e)$$

Although not explicitly indicated, these coefficients are all functions of position since ϵ , μ , σ , κ_x , and κ_z are, in general, spatially varying. The convolution terms in equations (2.8a-c) are modeled using the recursive convolution technique (Luebbers and Hunsberger, 1992), and are accounted for in equations (2.10a-c) through the

$\Psi_{H_{xz}}$, $\Psi_{H_{zx}}$, $\Psi_{E_{yx}}$, and $\Psi_{E_{yz}}$ terms. These are defined as:

$$\begin{aligned} \Psi_{H_{xz}}|_{i,j+1/2}^n &= B_z|_{i,j+1/2} \left[\Psi_{H_{xz}}|_{i,j+1/2}^{n-1} \right] \\ &+ A_z|_{i,j+1/2} \left[-E_y|_{i,j+2}^n + 27E_y|_{i,j+1}^n - 27E_y|_{i,j}^n + E_y|_{i,j-1}^n \right], \end{aligned} \quad (2.12a)$$

$$\begin{aligned} \Psi_{H_{zx}}|_{i+1/2,j}^n &= B_x|_{i+1/2,j} \left[\Psi_{H_{zx}}|_{i+1/2,j}^{n-1} \right] \\ &+ A_x|_{i+1/2,j} \left[-E_y|_{i+2,j}^n + 27E_y|_{i+1,j}^n - 27E_y|_{i,j}^n + E_y|_{i-1,j}^n \right], \end{aligned} \quad (2.12b)$$

$$\begin{aligned} \Psi_{E_{yx}}|_{i,j}^{n+1/2} &= B_x|_{i,j} \left[\Psi_{E_{yx}}|_{i,j}^{n-1/2} \right] \\ &+ A_x|_{i,j} \left[-H_z|_{i+3/2,j}^{n+1/2} + 27H_z|_{i+1/2,j}^{n+1/2} - 27H_z|_{i-1/2,j}^{n+1/2} + H_z|_{i-3/2,j}^{n+1/2} \right], \end{aligned} \quad (2.12c)$$

$$\begin{aligned} \Psi_{E_{yz}}|_{i,j}^{n+1/2} &= B_z|_{i,j} \left[\Psi_{E_{yz}}|_{i,j}^{n-1/2} \right] \\ &+ A_z|_{i,j} \left[-H_x|_{i,j+3/2}^{n+1/2} + 27H_x|_{i,j+1/2}^{n+1/2} - 27H_x|_{i,j-1/2}^{n+1/2} + H_x|_{i,j-3/2}^{n+1/2} \right], \end{aligned} \quad (2.12d)$$

where

$$A_k = \frac{\sigma_k}{\sigma_k \kappa_k + \alpha_k \kappa_k^2} (B_k - 1), \quad (2.13a)$$

$$B_k = \exp \left[-\frac{\Delta t}{\epsilon_0} \left(\frac{\sigma_k}{\kappa_k} + \alpha_k \right) \right] \quad (2.13b)$$

are PML update coefficients that, again, vary with location in the modeling grid. As can be seen from equations (2.12a-d), the values of the convolution terms at the current time step are computed from those at the previous time step. Therefore $\Psi_{H_{xz}}$, $\Psi_{H_{zx}}$, $\Psi_{E_{yx}}$, and $\Psi_{E_{yz}}$ must be stored, in addition to the H_x , H_z , and E_y field components, during the FDTD simulation. Throughout the above equations, we have kept our notation consistent with that of Roden and Gedney (2000) so that their paper can be consulted for further details on CPML implementation.

To introduce an electric field source into the grid during FDTD modeling using equations (2.10) through (2.13), we add a source pulse function to the update for the E_y field component at the desired spatial location. This amounts to adding

the source function to the y -component of the current density term in Maxwell's equations. To model receivers in our code, we simply record the E_y field component as a function of time at the receiver locations. It must be stressed that, because our modeling codes are two-dimensional, all such sources and receivers are actually line elements, extending to positive and negative infinity in the dimension perpendicular to the survey plane. As a result, the radiation patterns and geometrical spreading for realistic, dipole-type GPR antennas cannot be properly modeled with our codes; this would require either a fully or pseudo 3-D approach (e.g., Moghaddam et al., 1991; Xu and McMechan, 1997). Nevertheless, as stated previously, our 2-D codes capture many of the important features of reflection GPR surveying, and can provide much insight into the interaction of EM waves with a complex subsurface. They should be used with caution, however, when antenna radiation patterns play a critical role in how the data are analyzed. A key example is crosshole GPR attenuation tomography.

2.3.3 Numerical stability and dispersion criteria

An important step in FDTD modeling is choosing appropriate time and spatial discretization intervals for a simulation. Ideally, we would like to have Δx , Δz , and Δt as large as possible to make the simulation run most quickly. However, if Δt is too large, the FDTD scheme presented above will become numerically unstable. In addition, if Δx or Δz are too large, the electric and magnetic fields will be inadequately sampled in space and numerical dispersion will be the result. For the O(2,4) scheme presented here, the maximum time step that can be used, in order for the scheme to remain numerically stable, is (Georgakopoulos et al., 2002):

$$\Delta t_{max} = \frac{6}{7} \sqrt{\frac{\mu_{min} \epsilon_{min}}{\left(\frac{1}{\Delta x^2} + \frac{1}{\Delta z^2}\right)}}, \quad (2.14)$$

where μ_{min} and ϵ_{min} are the minimum magnetic permeability and dielectric permittivity values present in the modeling grid. To control numerical dispersion, the O(2,4) scheme must allow for 5 field samples per minimum wavelength (Bergmann et al., 1996; Georgakopoulos et al., 2002). The MATLAB programs `finddt.m` and `finddx.m` determine the maximum possible Δt , Δx , and Δz given a model's electrical properties as input, and should be run prior to starting any simulation.

2.3.4 PML absorbing boundaries

Compared with other absorbing boundary types, PML boundaries possess a number of significant advantages. First, the PML approach offers superior attenuation of reflections from the edges of the modeling grid, and requires only a small number of cells to be very effective (Gedney, 1998). Second, to implement PML, only the coordinate stretching variables need to be changed in the boundary regions, and not the FDTD update equations (i.e., the same update equations are used everywhere in the grid). For this reason, PML is well suited to parallel implementations. Finally, the CPML approach that we have chosen for our codes has the advantage of being media independent (Roden and Gedney, 2000). That is, the approach is implemented in the same manner no matter what the properties of the materials being modeled. For example, our FDTD formulation could be modified to allow for dispersion in ϵ , μ , and σ (say, using the technique of Bergmann et al. (1998)), and the Ψ terms for invoking CPML in equations (2.10a-c) would remain unchanged.

As mentioned previously, in the interior of the modeling grid, the coordinate stretching variables, s_x and s_z , are set to unity such that equations (2.10) through (2.13) become the standard, TM-mode, FDTD update equations in an unstretched coordinate space. This requires that $\kappa_x = \kappa_z = 1$ and $\sigma_x = \sigma_z = 0$ in these regions (see equation (2.4)). In the PML boundary regions, however, these parameters are given different values. Setting σ_x and σ_z greater than zero (which makes the stretching

variables complex) allows propagating waves to be absorbed. Making κ_x and κ_z greater than one, on the other hand, allows the PML regions to absorb evanescent waves. Setting α_x and α_z greater than zero may also improve the absorption of evanescent modes (Kuzuoglu and Mittra, 1996; Roden and Gedney, 2000), although by default these parameters are set to zero in our codes.

In theory, because there is no change in electromagnetic impedance associated with a change in s_x and s_z , values for κ_x , κ_z , σ_x , and σ_z should be set as high as possible in the PML regions to achieve the most complete absorption of propagating and evanescent waves. In practice, however, in the discrete FDTD space, numerical reflections occur when electrical properties change too much between nodes. Consequently, the PML parameters must be set to gradually increase from their values in the interior of the grid to some maximum value at the grid edges. For κ_x and κ_z , we have:

$$\kappa_k = \begin{cases} 1 & \text{in grid interior} \\ 1 + \left(\frac{d}{\delta}\right)^m (\kappa_{k_{max}} - 1) & \text{inside PML region,} \end{cases} \quad (2.15)$$

where d is the distance into the PML region from the interior/PML boundary, δ is the thickness of the PML region, m is known as the PML exponent, and $\kappa_{k_{max}}$ is the maximum value. Similarly, for σ_x and σ_z , we have:

$$\sigma_k = \begin{cases} 0 & \text{in grid interior} \\ \left(\frac{d}{\delta}\right)^m \sigma_{k_{max}} & \text{inside PML region,} \end{cases} \quad (2.16)$$

where $\sigma_{k_{max}}$ is the maximum value. Here, κ_k and σ_k vary only along the k direction since the coordinate stretching variables are one-dimensional functions. For example, σ_x will be zero throughout the interior of the modeling grid and non-zero only in the left and right PML regions. The κ_z parameter, on the other hand, will be one

throughout the interior of the grid and greater than one only in the top and bottom PML regions. In our codes, we use $m = 4$ and set $\kappa_{x_{max}} = \kappa_{z_{max}} = 5$ by default, which we have found is adequate for the effective absorption of evanescent waves. The maximum value for σ_k is determined using the following criterion (Gedney, 1998):

$$\sigma_{k_{max}} = \frac{m + 1}{150\pi\sqrt{\epsilon_r}\Delta k}, \quad (2.17)$$

where ϵ_r is the relative dielectric permittivity (i.e., the permittivity normalized to its value in free space) in the interior of the grid nearest to the PML boundary. In other words, in a heterogeneous medium, $\sigma_{k_{max}}$ may vary depending on the permittivity values bounding the interior of the modeling domain. The natural boundaries in the grid interior are extended into the PML region by padding with PML cells before running a simulation (Chen et al., 1997).

2.4 MATLAB implementation

The 2-D, TM-mode, finite-difference formulation presented above has been implemented in the MATLAB environment in the code `TM_model12d.m`, for reflection GPR modeling. The MATLAB code for TE-mode modeling, suitable for crosshole and VRP surveys, is `TE_model12d.m`. To perform the FDTD simulations in MATLAB, we use matrices to store all field components and electrical properties. The property matrices are double the size of the field matrices because ϵ , μ , and σ are required at every electric and magnetic field component location (see Figure 2.1). As inputs, `TM_model12d.m` and `TE_model12d.m` require the electrical property matrices, all source and receiver locations, a time vector and corresponding source pulse sampled with the appropriate Δt , and the number of PML boundary cells to use. All finite-differences in the FDTD update equations are computed using matrix notation instead of loops

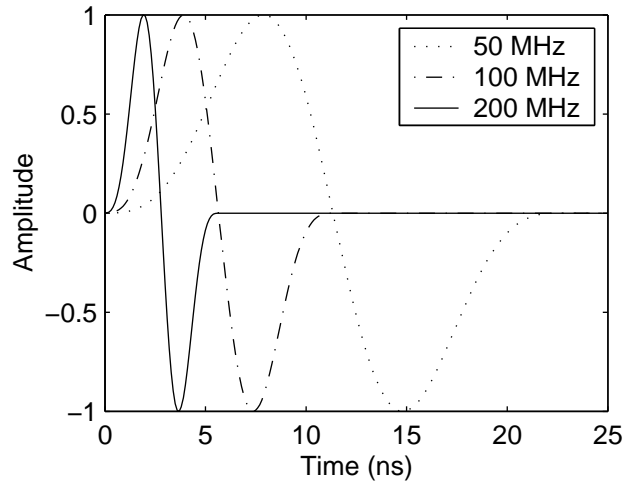


Figure 2.2: Examples of Blackman-Harris pulses fed into grid as sources in our FDTD modeling codes.

to optimize the codes for speed in MATLAB. In addition, the FDTD and PML update coefficients are calculated and stored in matrices the same size as the electrical property matrices before starting a simulation, so that the number of calculations required during each iteration is reduced. Finally, the Ψ terms in equations (2.10a-c) are computed and added to the electric and magnetic fields only in the PML regions, as in the interior of the modeling grid, these terms become zero.

For the source pulse in our codes, we use the normalized first derivative of a Blackman-Harris window function (Harris, 1978), which is described in Chen et al. (1997) for geophysical FDTD modeling. This pulse is created using the program `blackharrispulse.m`. Figure 2.2 shows Blackman-Harris pulses having dominant frequencies of 50, 100, and 200 MHz. When fed into the E_y field component at the desired source location in our TM-mode code, the resulting pulse that travels through the grid and is recorded at the receiver locations roughly resembles a Ricker wavelet.

Figure 2.3 is a flowchart showing the sequence of steps involved in simulating a

reflection GPR survey with our TM-mode modeling code. First, the maximum spatial discretization intervals that can be used, in order to control numerical dispersion, are determined using `finddx.m` given the electrical properties in the model and the source pulse as inputs. Next, the code `finddt.m` is used to determine the maximum time step that ensures numerical stability given the model's electrical properties, Δx , and Δz . If necessary, the electrical property matrices are interpolated at half the spatial discretization interval, since they are double the size of the field matrices, using the code `gridinterp.m`. As a final step before running a simulation, the property matrices are then padded around the edges with the proper number of PML absorbing boundary cells using the program `padgrid.m`. The values of σ , ϵ , and μ in the PML regions are set to be simply an extension of those in the interior of the grid.

In the code `TM_model2d.m`, an outer loop runs over the number of sources and an inner loop over the number of FDTD iterations required for each source. In each FDTD iteration, the H_x , H_z , and E_y field matrices are first updated, in that order, using equations (2.10) through (2.13). The appropriate time sample of the source pulse function is then fed into the E_y field component at the current source location, and the E_y wavefield is recorded at all of the receiver locations. The output from our codes is a data cube containing a series of stacked common-source gathers (i.e., we record multi-offset data). Extraction of common-offset data, which is typically acquired during reflection GPR profiling, from the multi-offset data cube is a trivial matter in MATLAB.

2.5 Examples

We now show examples of reflection and crosshole GPR modeling using the codes `TM_model2d.m` and `TE_model2d.m`, respectively. The programs are called with the example run scripts `TM_run_example.m` and `TE_run_example.m`. Figure 2.4 shows

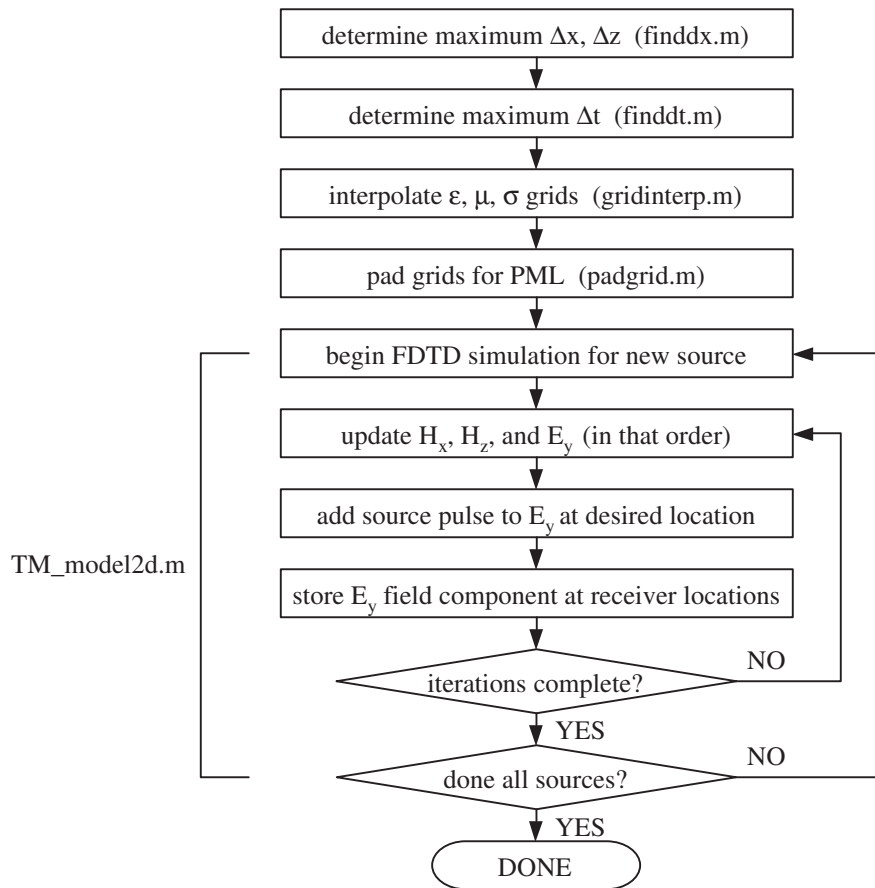


Figure 2.3: Flowchart of FDTD modeling procedure.

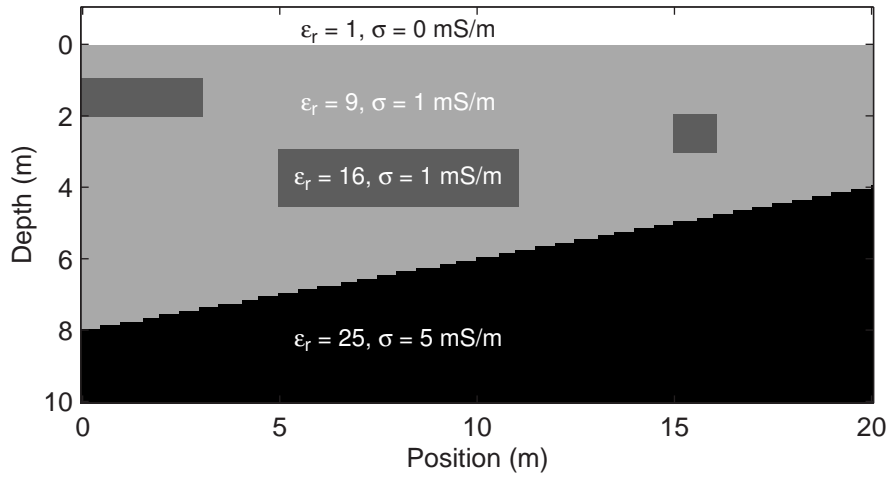


Figure 2.4: Electrical property model used for TM-mode reflection GPR example.

the electrical property model used for the TM-mode, reflection GPR example. The subsurface consists of two layers separated by a dipping boundary. The upper layer, representative of vadose zone sediment, has $\epsilon_r = 9$ and $\sigma = 1$ mS/m. The lower layer, representative of material in the saturated zone, has $\epsilon_r = 25$ and $\sigma = 5$ mS/m. Within the upper layer there are three anomalous blocks of different sizes having $\epsilon_r = 16$ and $\sigma = 1$ mS/m. For all materials, μ was set equal to its free space value, μ_0 . An air-earth interface is included in the model at $z = 0$; this was accomplished by simply adding a thin upper layer with $\epsilon_r = 1$ and $\sigma = 0$ to the grid. Sources and receivers were located along the air-earth interface every 0.2 m for the reflection survey. The Blackman-Harris source pulse had a dominant frequency of 100 MHz. For this pulse and the electrical properties in the model, `finddx.m` yielded a maximum possible spatial discretization of 0.0423 m. We used $\Delta x = \Delta z = 0.04$ m. The maximum possible time step, determined using `finddt.m`, was 0.0801 ns. We used $\Delta t = 0.08$ ns.

Figure 2.5 shows snapshots of the E_y field component at various times during the

FDTD simulation for the source located at $x = 10$ m. Because of the PML absorbing boundaries implemented in our code, no reflections can be seen coming from the edges of the modeling domain in any of the panels. At $t = 30$ ns, we capture the wavefield as it is spreading outwards from the source before it has encountered any heterogeneities within the earth. Head waves link the energy traveling more rapidly through the air with that traveling through the ground. At $t = 50$ ns, the wavefield has clearly encountered the large anomalous block in the middle of the upper layer, and has been partly reflected back towards the surface. The direct wave traveling through the air from the source location has also left the boundaries of the modeling domain at this point. At $t = 70$ ns, the energy reflected from the block in the upper layer has reached the air-earth interface. At $t = 90$ ns, we see the wavefield being reflected from the dipping boundary between the top and bottom layers. Figure 2.5 clearly shows that, even for the relatively simple earth model shown in Figure 2.4, the propagating wavefield becomes quite complicated very quickly.

Figure 2.6 shows one of the common-source gathers (consisting of the recorded E_y field component in time at all of the receiver locations) for the source located at $x = 10$ m in Figure 2.4. This is one slice of the output multi-offset data cube. The linear events in the image are the direct air and ground arrivals. The events with hyperbolic moveout are reflections from the top and bottom of the block anomaly in the middle of the upper layer, and the dipping boundary between the upper and lower layers. Figure 2.7, on the other hand, shows the common-offset reflection GPR data that were extracted from the data cube. The source-receiver offset for this image is 1 m. In the image, diffractions are clearly seen originating from each corner of the block anomalies. Also, the dipping boundary between the upper and lower layers is strongly visible, although it is not a perfectly straight interface in the GPR section because of time shifts caused by the velocity anomalies in the upper layer. Finally, the direct air and ground waves are merged together and present at the top of Figure 2.7.

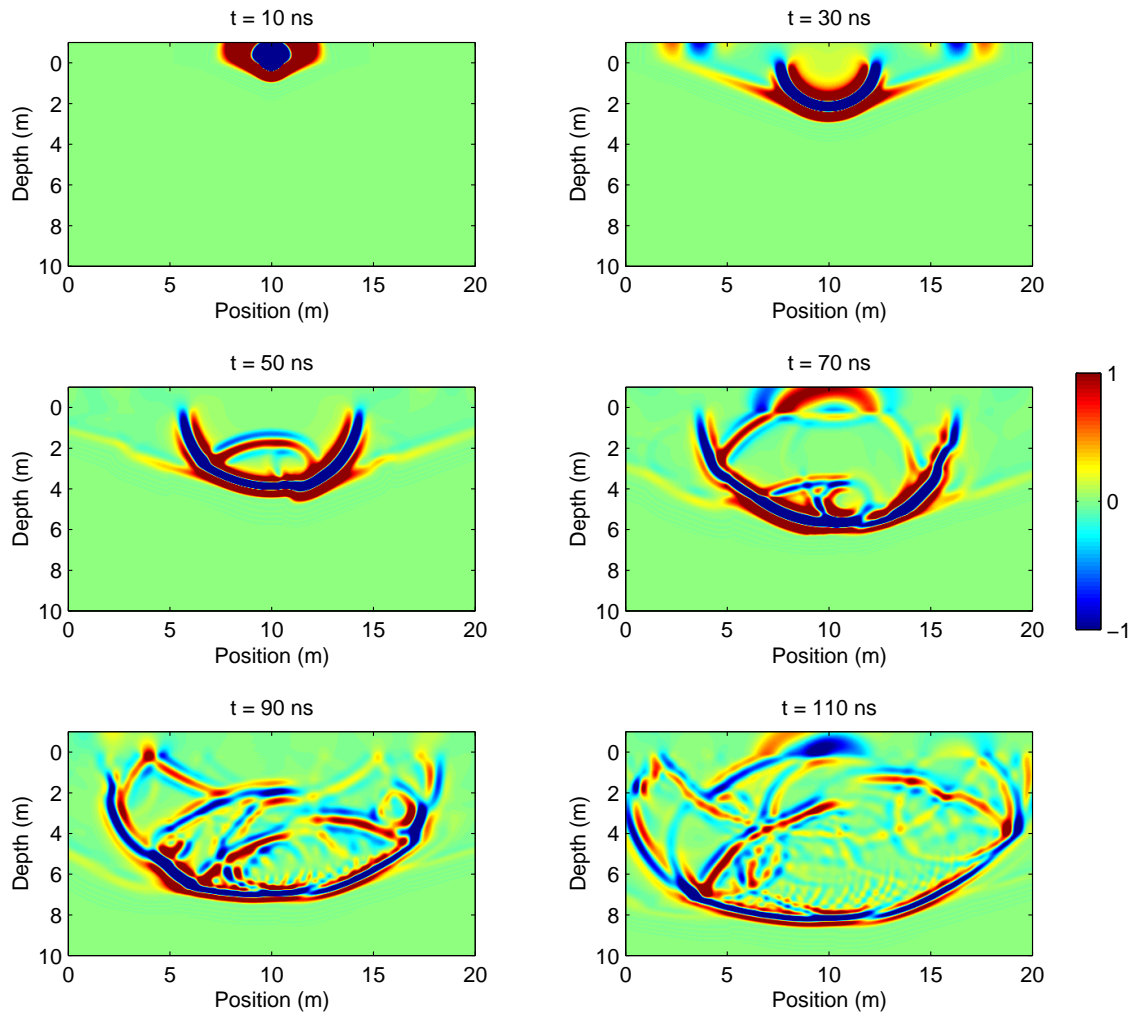


Figure 2.5: Snapshots showing amplitude of E_y wavefield at different times during TM-mode FDTD modeling. Source is located at $x = 10$ m, $z = 0$ m.

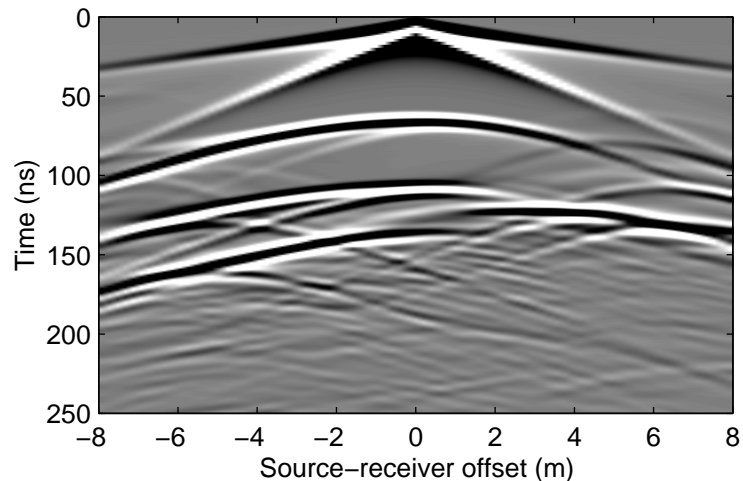


Figure 2.6: Common-source gather for source located at $x = 10$ m, $z = 0$ m in Figure 2.4.

In our second example, we demonstrate FDTD modeling of a crosshole GPR survey using `TE_model12d.m`. Figure 2.8 shows the subsurface EM-wave velocity of the survey plane, which was obtained from the distribution of relative dielectric permittivity using the following low-loss approximation:

$$v = \frac{c}{\sqrt{\epsilon_r}}, \quad (2.18)$$

where c is the velocity of EM waves in free space (0.3 m/ns). The permittivity model was constructed using the GSLIB geostatistical software package (Deutsch and Journel, 1992). Relative permittivity values were set to vary between 20 and 32, a range which is typical of materials in the saturated zone. A constant conductivity of 5 mS/m was assumed, and μ was again set equal to its value in free space. Sources were located every 0.25 m from 0.5 to 10.5 m depth down a borehole located at $x = 0.5$ m. Receivers were located at the same depths in a borehole located at

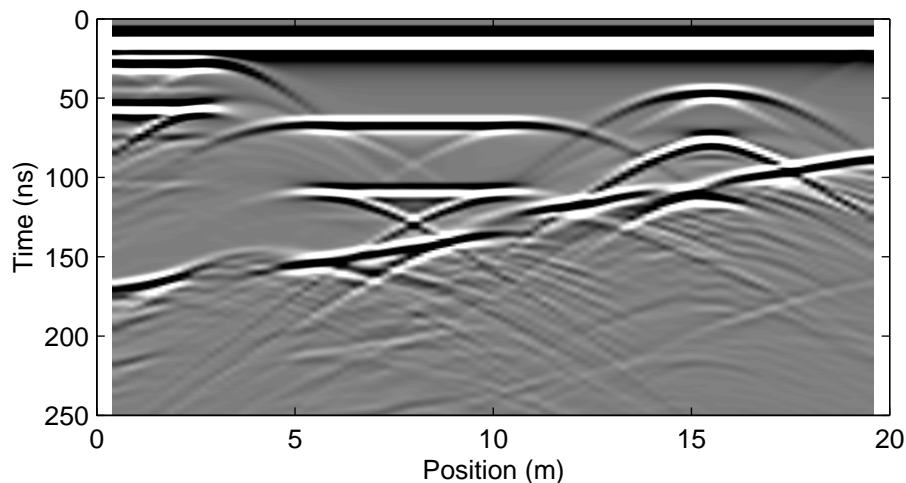


Figure 2.7: Common-offset gather for TM-mode reflection GPR modeling example.

$x = 5.5$ m. Again, a Blackman-Harris pulse with a dominant frequency of 100 MHz was used as a source function. For this example, `finddx.m` yielded a maximum spatial discretization interval of 0.0374 m. We used $\Delta x = \Delta z = 0.025$ m. The maximum possible time step determined using `finddt.m` was 0.0226 ns. We used $\Delta t = 0.02$ ns. The air-earth interface was not modeled in this example to facilitate the automatic picking of travel times through the earth in the resulting data.

Figure 2.9 shows snapshots of the E_z field component at various times during the crosshole modeling when the E_z source was located at $z = 2$ m. The propagating wavefront in this case is much more circular than that shown in Figure 2.5 because the magnitudes of the velocity heterogeneities in this example are quite small. Small variations in velocity were purposely used in this example so that the resulting travel time data could be inverted reasonably accurately using a simple, straight-ray tomography code. Despite this, low-amplitude reflections are clearly seen in Figure 2.9, which arise from the velocity heterogeneities.

Figure 2.10 shows one of the common-source gathers that was obtained in this

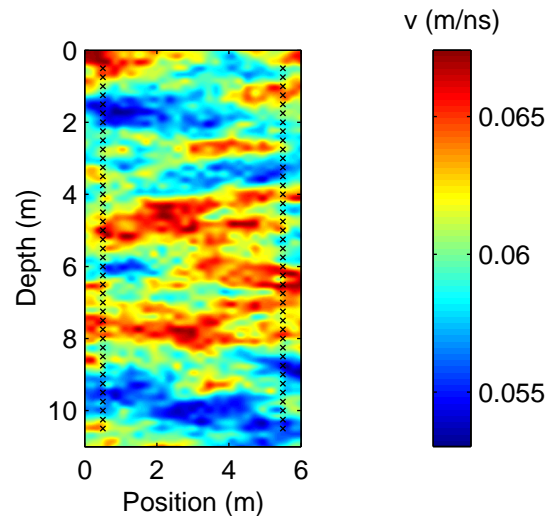


Figure 2.8: Subsurface velocity model used for TE-mode crosshole GPR example. Source and receiver locations are marked by an ‘x’.

example for the E_z source located at $z = 5$ m in Figure 2.8. The first-arrival times in each common-source gather (i.e., the arrival times for each source-receiver configuration in the survey) were picked automatically from the data based on the first point in each trace where the amplitude exceeded 1% of the trace maximum. These noise-free travel-time data were then inverted using a straight-ray, least-squares, tomography algorithm with a small amount of second derivative smoothness regularization added for stability. Figure 2.11 shows the resulting velocity tomogram. Compared with Figure 2.8, we see that the inversion of the noise-free travel-time data, as expected, produces a very good image of the subsurface velocity field. There is a small amount of smearing in the image along some of the high-angle raypath directions. Also, the resolution of the inversion result is slightly worse than that of the true velocity model, due to the resolution limits of ray-based tomography, the aperture-limited nature of the survey, and errors resulting from our straight ray approximation.

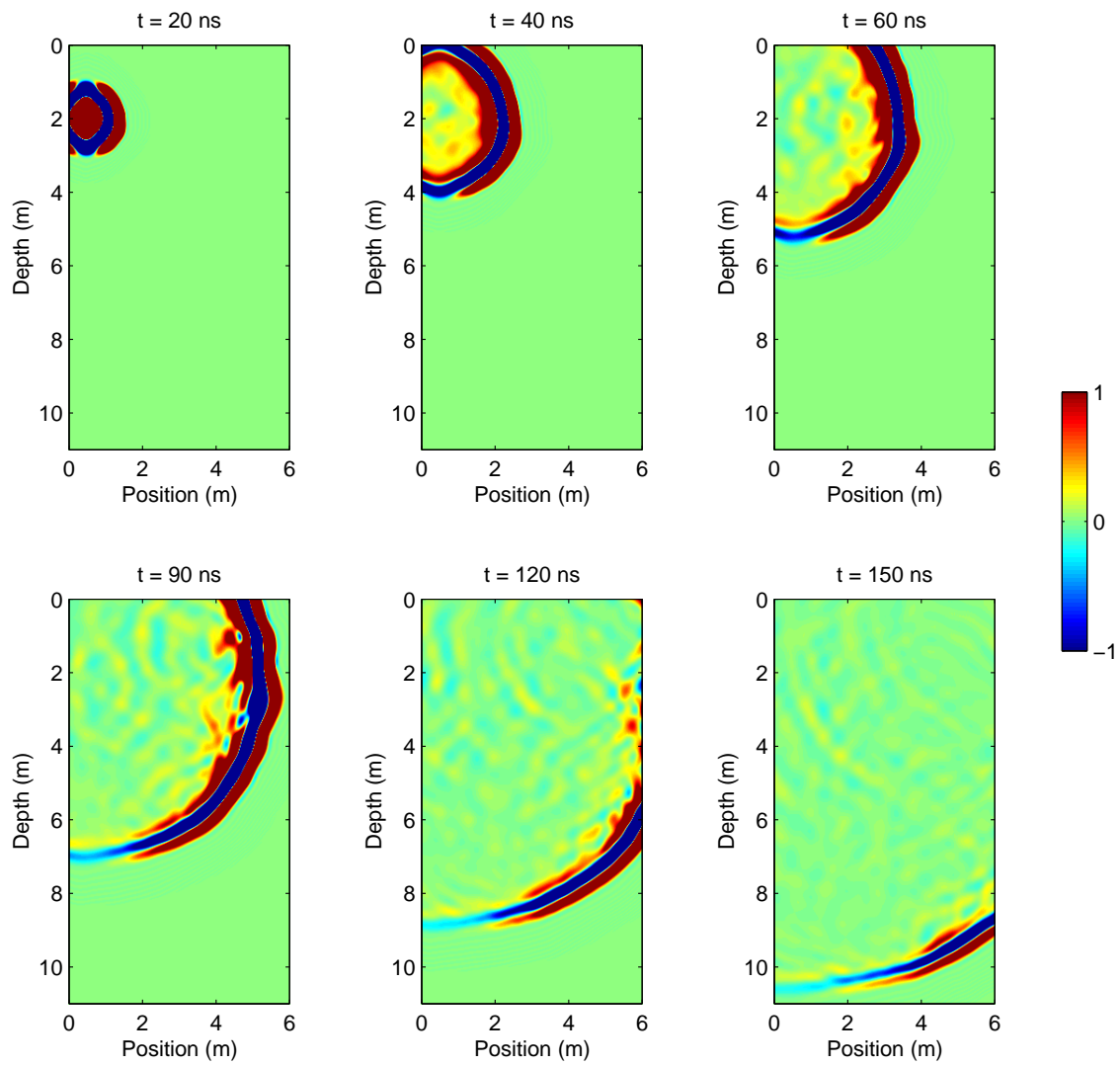


Figure 2.9: Snapshots showing amplitude of E_z wavefield at different times during TE-mode FDTD modeling. Source is located at $x = 0.5$ m, $z = 2$ m.

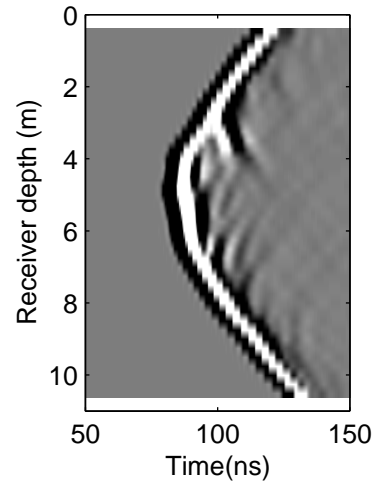


Figure 2.10: Common-source gather for source located at $x = 0.5$ m, $z = 5$ m in Figure 2.8.

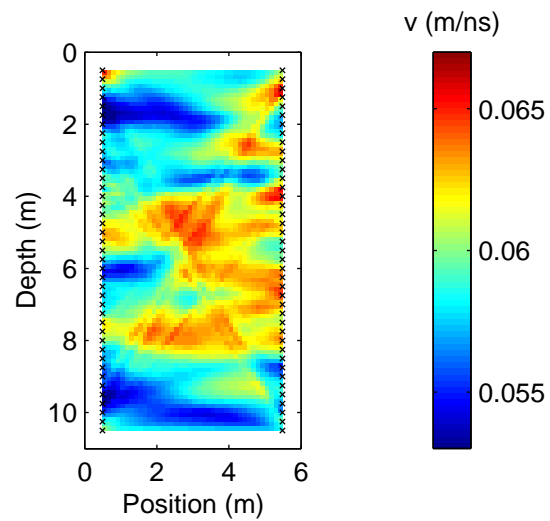


Figure 2.11: Straight-ray velocity tomogram obtained from synthetic crosshole data created using our TE-mode code.

2.6 Conclusions

The codes presented here provide a relatively easy-to-understand, flexible package for 2-D GPR modeling in MATLAB. Although the use of MATLAB means that our codes are slightly slower than similar compiled C or Fortran routines, the MATLAB environment offers significant benefits over these other programming languages such as increased code readability and easier plotting and manipulation of data. Our codes are well suited to be modified for more complex modeling if desired, an example being to alter them to allow for dispersion in electrical properties. The possibility also exists, for very long reflection GPR surveys, for the run scripts that we have provided to be modified so that only the subsurface region contributing to the traces being recorded is considered. This could be done without altering the main code, `TM_model2d.m`, and could significantly decrease the modeling time for very long survey lines.

Chapter 3

Simulation of antenna transmission and reception for crosshole GPR

3.1 Abstract

To develop waveform-based inversion methods for crosshole ground-penetrating radar (GPR) data, numerical models that account for realistic transmitter and receiver antenna behavior are required. A challenge in developing such models is simulating the antennas in a computationally efficient manner such that inversions can be performed in a reasonable amount of time. We present an approach to efficiently simulate crosshole GPR transmission and reception in heterogeneous media. The core of our approach is a finite-difference time-domain (FDTD) solution of Maxwell's equations in 2-D cylindrical coordinates. First, we determine the behavior of the current on a realistic GPR antenna in a borehole through detailed FDTD modeling of the antenna and its immediate surroundings. To model transmission and reception, we then replicate this antenna current behavior on a much coarser grid using a superposition of point electric dipole source and receiver responses. Results obtained with our technique are in excellent agreement with analytical results, numerical modeling results

where the transmitter antenna and borehole are explicitly accounted for using a fine discretization, and crosshole GPR field data.

3.2 Introduction

Over the past decade, crosshole ground-penetrating radar (GPR) has gained increasing popularity as a tool for high-resolution imaging of the shallow subsurface. Applications of this technique include delineation of orebodies (Fullagar et al., 2000), location of underground tunnels and voids (Olhoeft, 1988; Moran and Greenfield, 1993), mapping fractures in bedrock (Olsson et al., 1992; Day-Lewis et al., 2003), and estimation of subsurface lithology and hydrogeological properties using field or laboratory-derived petrophysical relationships (Alumbaugh and Chang, 2002; Moysey and Knight, 2004; Tronicke et al., 2004). Of interest in our research is the use of tomographic images obtained from crosshole GPR data in the development of subsurface hydrogeological models.

Crosshole GPR tomography is identical in principle to crosswell seismic tomography. A transmitter antenna, moved to numerous locations in one borehole, radiates high frequency electromagnetic (EM) pulses that are recorded by a receiver antenna, which is moved down a second borehole. Most commonly, inversion of the resulting data is accomplished by assuming that the propagating radar energy can be modeled by infinite-frequency rays that join the centers of the antennas. Under this assumption, the first-break travel times and amplitudes of the data can be used to determine the distribution of subsurface EM wave velocity and attenuation. The ray-based tomographic images of the subsurface obtained in this manner, however, are limited in resolution to approximately the width of the first Fresnel zone associated with the propagating pulse bandwidth (Williamson and Worthington, 1993). In order to improve resolution, modeling algorithms that account for more detailed physical aspects

of the crosshole GPR experiment, such as wave propagation and antenna behavior, are required. These algorithms can be employed in waveform-based inversion strategies that use all of the recorded data to determine subsurface properties (e.g., Pratt and Worthington, 1988; Zhou et al., 1995).

A number of approaches have been presented for crosshole GPR modeling. None of these, however, allow for the simulation of both antenna transmission and reception in heterogeneous media. Sato and Thierbach (1991), for example, modeled a crosshole GPR experiment analytically using an expression for the current on an insulated dipole antenna derived by King and Smith (1981). Although their approach gives much insight into the effects of antenna and system parameters on recorded GPR wavelets, it requires a homogeneous medium between the boreholes, and that the antennas be in the far field of one another. In addition, the expression that they used for the antenna current is not valid for the case of water-filled boreholes, and is thus only suitable for modeling in the vadose zone. Holliger and Bergmann (2002), on the other hand, modeled crosshole GPR numerically using a finite-difference time-domain (FDTD) approach in 2-D cylindrical coordinates. In their formulation, only the transmitter borehole was included in the model, and the antennas were simulated as point vertical electric dipoles. Ernst et al. (2005) further developed this algorithm to allow for detailed modeling of a realistic, finite-length transmitter antenna. Ellefsen and Wright (2005) employed a similar approach to examine the radiation patterns of realistic borehole GPR antennas. With these methods, much can be learned about the effects of the borehole, subsurface heterogeneity, and antenna characteristics on crosshole GPR radiation. However, only half of the antenna problem can be addressed; explicit modeling of both the transmitter and receiver antennas and boreholes is not possible using 2-D cylindrical coordinates, and would require a fully 3-D approach. Considering the many FDTD simulations that are necessary to forward model a crosshole GPR data set, and the numerous forward model calculations that

are required for inversion, such an approach remains too computationally intensive for most computers.

We present an algorithm to efficiently simulate crosshole GPR transmission and reception in heterogeneous media. This is accomplished using FDTD modeling in 2-D cylindrical coordinates through a superposition of point dipole source and receiver responses. Our technique replicates the behavior of the antenna current in the boreholes, without the need for explicit modeling of the antennas and boreholes. To begin, we develop the basis for our approach using analytical expressions for transmission and reception between dipole antennas located in a homogeneous medium. After demonstrating the approach for two simple cases where ideal antenna current distributions are assumed, we next discuss a means of determining the current distribution on a realistic GPR antenna located in an air- or water-filled borehole. Finally, we compare results obtained using our technique with analytical results, numerical modeling results where the transmitter antenna and borehole have been explicitly included in the modeling grid, and crosshole GPR field data.

3.3 Development of the modeling algorithm

3.3.1 FDTD modeling in 2-D cylindrical coordinates

The core of our modeling approach is the FDTD solution of Maxwell's equations in 2-D cylindrical coordinates presented by Holliger and Bergmann (2002). In this formulation, rotational symmetry about the vertical z -axis is assumed such that Maxwell's equations can be separated into the transverse magnetic (TM) and transverse electric (TE) modes, which are two sets of coupled partial-differential equations involving the $\{E_\phi, H_r, H_z\}$ and $\{E_r, E_z, H_\phi\}$ electric and magnetic field components, respectively. For crosshole GPR modeling where the antennas are oriented parallel to the z -axis,

only the TE-mode equations are required. These are solved numerically in the time domain using a leapfrog, staggered-grid approach, which involves offsetting the electric and magnetic field components such that the finite-difference approximations of all partial derivatives are centered in both space and time (Yee, 1966). Stepping forward in time is accomplished by alternately updating the electric and magnetic fields. All updates are fully explicit. For approximate modeling of the radiation from an infinitesimal vertical electric dipole, a source current function is added to the update for the E_z field component at the desired spatial location. This amounts to adding the source function to the z -component of the current density term in Maxwell's equations (Buechler et al., 1995).

We locate our field components in space in an identical manner to Holliger and Bergmann (2002) to avoid singularity problems on the z -axis. We also use second-order-accurate finite-difference approximations for all derivatives, which means that 10 grid points per minimum wavelength are required to control numerical dispersion. The time step is chosen according to the Courant numerical stability criterion (Holliger and Bergmann, 2002). Higher-order approximations could be used for the spatial and/or temporal derivatives in our code, with a moderate increase in code complexity, to decrease the number of field points needed and thus reduce computing time (e.g., Bergmann et al., 1999). We have implemented perfectly matched layer (PML) absorbing boundaries in cylindrical coordinates to prevent reflections from the top, bottom, and right-hand side of the simulation grid (Berenger, 1994; Teixeira and Chew, 1997).

With the assumed cylindrical symmetry the transmitter antenna and its borehole, which are centered on the z -axis, can be explicitly and accurately represented with the above approach. However, as mentioned previously, explicit modeling of both antennas and their boreholes to account for transmission and reception is not possible using 2-D cylindrical coordinates, and would require a fully 3-D approach. Next, we

describe how this basic code can be adapted to model both antenna transmission and reception using a superposition of point source and receiver responses.

3.3.2 Simulation of antenna transmission and reception

Borehole GPR antennas are generally center-fed, linear dipoles. We begin with the far-field analytical expressions for radiation and reception between two such antennas aligned parallel to the z -axis and located in a homogeneous medium. A schematic of this situation is shown in Figure 3.1. Both antennas have half-length l and are terminated by loads having impedance Z_0 . The transmitter antenna is excited by the generator voltage pulse $V_g(t)$. Electromagnetic waves incident upon the receiver antenna induce the voltage V_r in the receiver load. In the far field, the frequency-domain expression for the radiated electric field is (Sato and Thierbach, 1991)

$$E_\theta(r, \theta, \omega) = -i\xi k \frac{e^{-ikr}}{4\pi r} h_{eff}(\omega) I(0, \omega), \quad (3.1)$$

where r and θ are defined in Figure 3.1, E_θ is the total electric field in the direction of unit vector $\hat{\theta}$, ω is angular frequency, ξ and k are the electromagnetic impedance and wave number in the surrounding medium respectively, $I(0, \omega)$ is the frequency-domain antenna current at the feed point $z = 0$, and $h_{eff}(\omega)$ is the θ component of the vector antenna effective height, given by (Sengupta and Tai, 1976)

$$h_{eff}(\omega) = -\frac{\sin \theta}{I(0, \omega)} \int_{-l}^l I(z, \omega) e^{ikz \cos \theta} dz. \quad (3.2)$$

The parameters ξ and k are given in terms of the dielectric permittivity, ϵ , magnetic permeability, μ , and electrical conductivity, σ , of the surrounding medium as follows:

$$\xi = \sqrt{\frac{\mu}{\epsilon - i\sigma/\omega}}, \quad (3.3)$$

$$k = \omega \sqrt{\mu (\epsilon - i\sigma/\omega)}. \quad (3.4)$$

Substituting equation (3.2) into equation (3.1), we obtain

$$E_\theta(r, \theta, \omega) = \int_{-l}^l \left[-i\xi k \frac{e^{-ikr}}{4\pi r} I(z, \omega) \sin \theta \right] e^{ikz \cos \theta} dz. \quad (3.5)$$

The term in brackets in equation (3.5) is the far-field response of an infinitesimal vertical electric dipole having current $I(z, \omega)$ (e.g., Balanis, 1997). This equation thus shows that the electric field radiated by the transmitter antenna could be approximated by a superposition of the responses of a number of infinitesimal electric dipoles located along the length of the antenna, each excited by some current function $I(z, t)$. This fact was used by Arcone (1995) to numerically examine the radiation patterns of resistively loaded dipoles. The delay in phase by the exponential term outside the brackets in equation (3.5) accounts for the differences in path length between the far-field measurement point and different points on the antenna.

Consider now the frequency-domain current at the transmitter feed point, which is related to the generator voltage as follows (Sato and Thierbach, 1991):

$$I(0, \omega) = \frac{V_g(\omega)}{Z_0 + Z_{in}(\omega)}, \quad (3.6)$$

where $Z_{in}(\omega)$ is the antenna input impedance. Defining

$$A(z, \omega) = \frac{I(z, \omega)}{I(0, \omega)} \left(\frac{1}{Z_0 + Z_{in}(\omega)} \right), \quad (3.7)$$

we have

$$I(z, \omega) = A(z, \omega) V_g(\omega), \quad (3.8)$$

or in the time domain,

$$I(z, t) = A(z, t) * V_g(t). \quad (3.9)$$

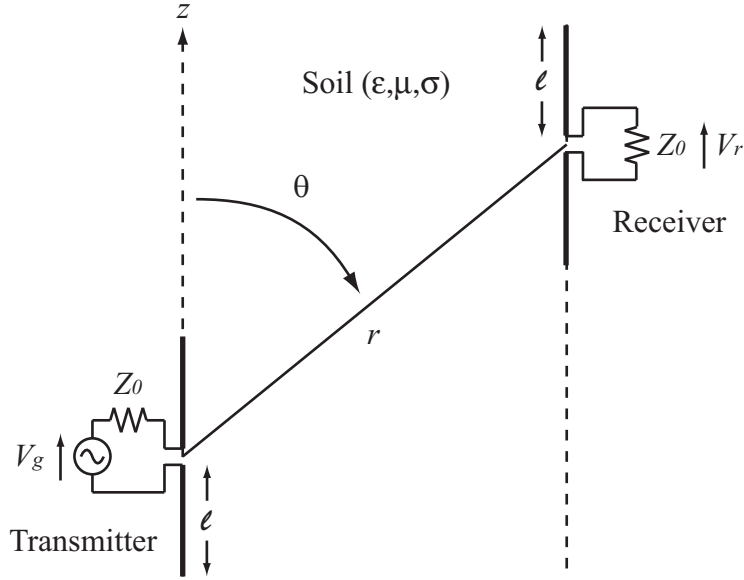


Figure 3.1: Basic schematic of a crosshole GPR experiment. For simplicity, the boreholes and antenna cross-sectional details have not been included. After Sato and Thierbach (1991).

Here, we see that the current at each point on the transmitter antenna can be expressed as the convolution of the generator voltage pulse with the function $A(z, t)$. We call $A(z, t)$ the antenna current impulse response because it represents the current that results on the antenna in response to a delta voltage excitation.

As an example, we calculated $A(z, t)$ using the inverse Fourier transform of equation (3.7) for the case of a 2-m-long, bare-wire dipole antenna attached to a 50Ω load and embedded in a lossless medium having dielectric constant $\kappa = 9$ (Figure 3.2). For the antenna current and input impedance, we used the familiar standing-wave expressions (e.g., Smith, 2001),

$$I(z, \omega) = I(0, \omega) \frac{\sin k(l - |z|)}{\sin kl} \quad (3.10)$$

and

$$Z_{in} = -iZ_c \cot kl, \quad (3.11)$$

which are obtained by approximating the antenna as a short-circuited transmission line having characteristic impedance Z_c . For the wave number on the antenna, we used the low-loss expression

$$k = \frac{\omega\sqrt{\kappa}}{c} \quad (3.12)$$

where c is the velocity of light in free space. We set $Z_c = 150 \Omega$ to yield a feed point reflection coefficient of 0.5. Figure 3.2 shows that, in response to an input voltage pulse, a current pulse is created on each arm of the transmitter antenna. These two pulses travel back and forth between the antenna feed and end points. For this simple example, we assumed that the velocity of the current pulses on the antenna is the same as that of the external medium. In addition, the pulses were assumed to travel without any distortion and become reduced in amplitude only upon reflection at the feed point. In the next section, we evaluate the suitability of assuming this type of simple current behavior for the crosshole GPR case.

At the receiver antenna, we are interested in an expression for V_r , the voltage induced in the receiver load by the radiated electric field. In the far field, this is given in the frequency domain by (Sato and Thierbach, 1991)

$$V_r(r, \theta, \omega) = -E_\theta(r, \theta, \omega) h_{eff}(\omega) \left(\frac{Z_0}{Z_0 + Z_{in}(\omega)} \right). \quad (3.13)$$

Substituting equation (3.2) for the antenna effective height into the above expression, and using our definition for $A(z, \omega)$, we obtain:

$$V_r(r, \theta, \omega) = \int_{-l}^l [E_\theta(r, \theta, \omega) \sin \theta e^{ikz \cos \theta}] A(z, \omega) Z_0 dz, \quad (3.14)$$

where integration is now along the length of the receiver antenna. The term in

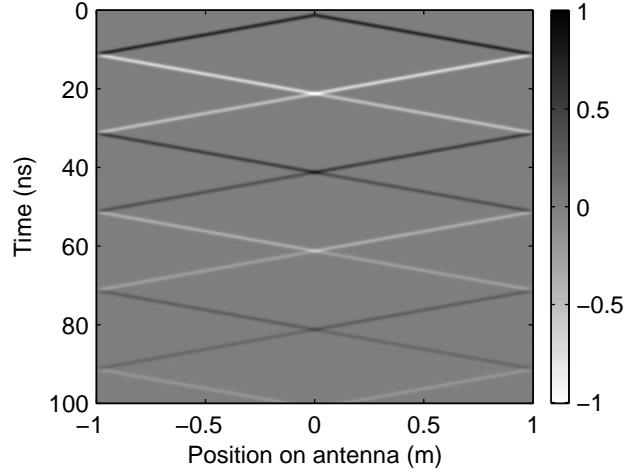


Figure 3.2: Normalized antenna current impulse response, $A(z, t)$, for a 2-m-long, bare-wire, standing-wave dipole antenna embedded in a lossless $\kappa = 9$ medium. Results were obtained using the inverse Fourier transform of equation (3.7).

brackets in equation (3.14) is simply the z -component of the electric field at location z on the antenna. Defining this quantity as $E_z(z, \omega)$, we obtain in the time domain

$$V_r(r, \theta, t) = \int_{-l}^l [E_z(z, t) * A(z, t)] Z_0 dz. \quad (3.15)$$

Equation (3.15) shows that, similar to the transmission case, the voltage induced in the receiver load can also be approximated as a superposition of the responses of infinitesimal elements along the receiver antenna. Specifically, we can obtain $V_r(t)$ by summing the convolution of $E_z(z, t)$ and $A(z, t)$ along the antenna, and multiplying this result by the load impedance, Z_0 . Intuitively, this can be understood as follows. At each point on the receiver antenna, the E_z component of the incident EM pulse from the transmitter antenna induces current pulses that travel in both directions away from that point. As in the transmission case, these pulses reverberate along the antenna arm. Just as $A(z, t)$ describes how an impulsive voltage at the transmitter

antenna feed is related to the current experienced at each point along the antenna, it also describes how an impulsive voltage excitation at each point on the receiver antenna is related to the current experienced at the center. Thus we convolve $E_z(z, t)$ with $A(z, t)$ and sum along the antenna to obtain the total current in the receiver load. The multiplication by Z_0 transforms this current into voltage.

Based on the above results, we can numerically simulate crosshole GPR transmission and reception using the previously described FDTD code in 2-D cylindrical coordinates. To model transmission, we first obtain the antenna current distribution by convolving the excitation voltage pulse with $A(z, t)$. To the update for the E_z field at each point in the simulation grid corresponding to a location on the transmitter antenna, we then add the appropriate current function, which simulates infinitesimal vertical electric dipole radiation from that point. Together, the responses of the infinitesimal dipoles emulate the radiation of the finite-length antenna. To model reception, the E_z field at all nodes collocated with the receiver antenna is stored during the finite-difference simulation. After the time stepping is complete, the recorded data are convolved with the appropriate values of $A(z, t)$ and then summed and multiplied by Z_0 to obtain the receiver load voltage. In simulating transmission and reception in this manner, we avoid explicit, detailed modeling of the antennas and their boreholes, and instead account for these features through the antenna current behavior. As a result, modeling can be performed very efficiently on a relatively coarse grid. In addition, although we used far-field expressions to derive this approach, it is not restricted to the far field, and is thus perfectly valid for the small borehole separations that are typically encountered in crosshole GPR.

3.3.3 Examples for standing-wave and Wu-King dipole antennas

As basic examples of our modeling approach, Figures 3.3 and 3.4 show the radiated E_z field and receiver load voltage determined for two cases that represent the end members of commercial borehole GPR antennas. In Figure 3.3, we used the antenna current impulse response function from Figure 3.2 to model radiation and reception between 2-m-long, standing-wave dipole antennas embedded in a lossless, homogeneous medium having $\kappa = 9$. The transmitter antenna was placed at a depth of 10 m, and the horizontal antenna separation was 4 m. For the excitation voltage, we used a Gaussian pulse, given by

$$V_g(t) = \exp \left[- \left(\frac{t - t_0}{\tau} \right)^2 \right], \quad (3.16)$$

where the characteristic time τ was set equal to 1 ns, and t_0 was chosen such that $V_g(0)$ is the first point in the Gaussian where the amplitude reaches 0.1% of its maximum value. The radiated E_z field for the standing-wave dipole can be seen to consist of a series of positive and negative pulses, each of which represents radiation from either the antenna feed or end points in accordance with time-domain antenna theory (Smith, 1997, 2001). That is, although we have superimposed the responses of infinitesimal dipoles along the entire length of the antenna to model the radiated wavefield, these responses cancel everywhere on the dipole except at the feed and end points, where charge acceleration and deceleration take place. We purposely chose a short excitation pulse and long antennas for this example to demonstrate this effect. If the antennas were shortened, the current pulse velocity along the antennas were increased, or the excitation pulse were lengthened, then the discrete arrivals seen in Figure 3.3 would merge. This typically occurs in crosshole radar data (Sato and

Thierbach, 1991). There is also a significant difference between the E_z and received voltage waveforms in Figure 3.3. Whereas E_z consists of distinct pulses in time, the received voltage waveform appears more like an integrated pulse sequence. This is also in accordance with time-domain antenna theory (Shlivinski et al., 1997; Smith, 2004), and illustrates the importance of properly accounting for reception, in addition to transmission, when modeling crosshole GPR data.

In Figure 3.4, we used the same modeling parameters and experimental geometry as Figure 3.3, but altered $A(z, t)$ to simulate transmission and reception between resistively loaded, Wu-King dipole antennas (Wu and King, 1964). Specifically, the amplitude of the original standing-wave dipole impulse response shown in Figure 3.2 was linearly tapered to zero at the ends of the antenna such that (Smith, 1997)

$$A_{wk}(z, t) = \begin{cases} A_s(z, t) (1 - |z|/l) & \text{if } t \leq l/v_{ant} \\ 0 & \text{otherwise,} \end{cases} \quad (3.17)$$

where v_{ant} is the velocity of the current pulses on the antenna, $A_{wk}(z, t)$ is the Wu-King dipole impulse response, and $A_s(z, t)$ is the standing-wave dipole impulse response. Whereas a standing-wave antenna sustains pulses of current that travel back and forth along the antenna arms, a Wu-King dipole is loaded with resistance in such a manner to be reflectionless. For this reason, the pulses of current on a Wu-King dipole travel only from the feed point to the ends of the antenna before they decay to zero amplitude. Figure 3.4 shows that, in contrast to the standing-wave case, the radiated and received waveforms for the Wu-King dipole are very compact. Because there are no reflections on the antenna, radiation comes largely as an initial pulse from the feed point (Smith, 1997). The results in Figure 3.4 are in accordance with those obtained by Sengupta and Liu (1974), who analytically investigated the response of Wu-King dipoles to Gaussian pulse excitation.

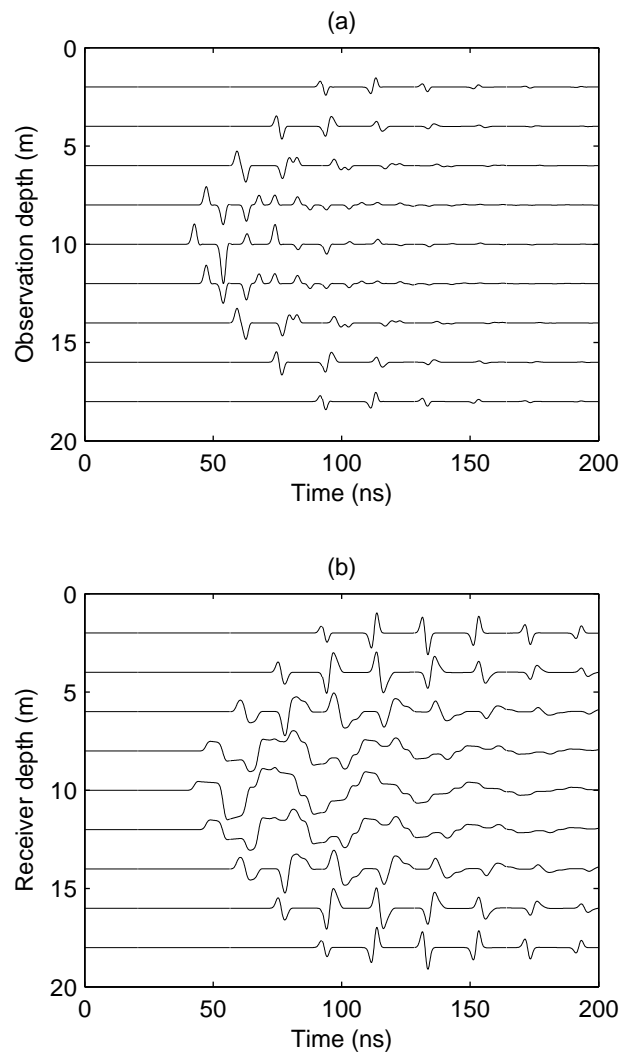


Figure 3.3: (a) Radiated E_z field and (b) received waveform determined for 2-m-long, standing-wave dipole antennas in a lossless $\kappa = 9$ medium.

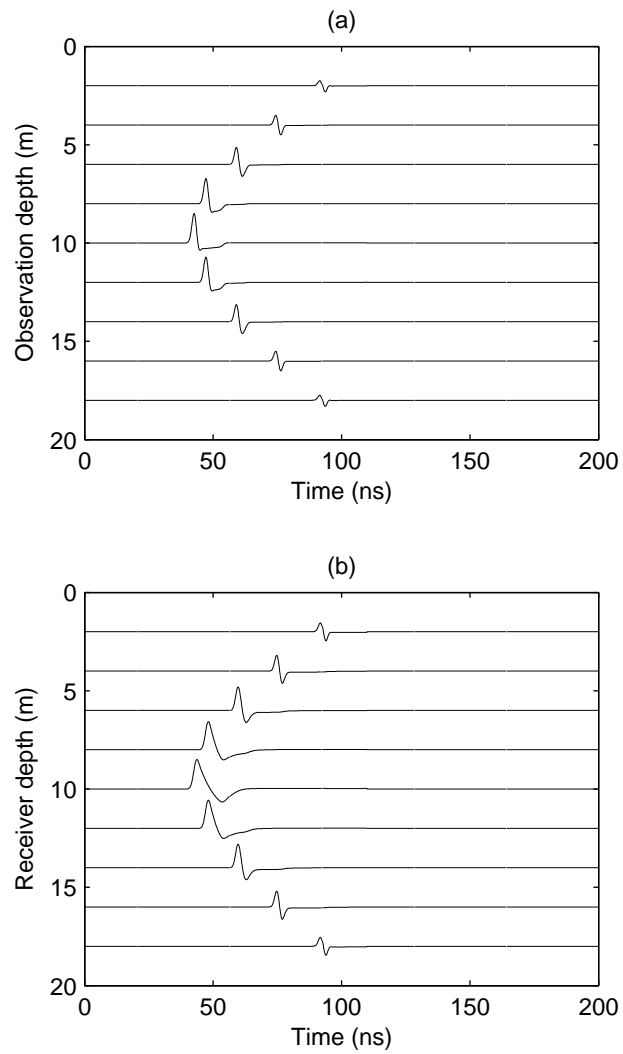


Figure 3.4: (a) Radiated E_z field and (b) received waveform determined for 2-m-long, resistively loaded (Wu-King) dipole antennas in a lossless, $\kappa = 9$ medium.

In practice, commercial borehole GPR antennas lie somewhere between the undamped, standing-wave dipoles of Figure 3.3 and the Wu-King dipoles of Figure 3.4. That is, these antennas tend to be lightly resistively loaded to achieve a compromise between power radiated into the ground and pulse width, which ideally should be short. Indeed, crosshole GPR waveforms that we have recorded in the field tend to contain more peaks and troughs than the waveforms displayed in Figure 3.4b, but significantly less of these than the waveforms shown in Figure 3.3b.

3.3.4 Behavior of the antenna current for crosshole GPR

To model antenna transmission and reception using a superposition of point source and receiver responses, we require prior knowledge of the antenna current behavior, contained in $A(z, t)$. For the examples shown in Figures 3.3 and 3.4, ideal $A(z, t)$ functions were assumed. In using these functions, the velocity of the current pulses on the antennas was assumed to be the same as the EM wave velocity of the surrounding medium, and the pulses were assumed to undergo no change in shape as they traveled along the antenna arms. For the simple case of a thin, bare-wire antenna embedded in a homogeneous medium, this behavior may be a reasonable approximation to reality (Balanis, 1997). However, in the crosshole radar case, the antennas are insulated and located in air- or water-filled boreholes. As a result, such simple $A(z, t)$ functions are generally not valid.

In the situation where the materials between the antenna wire and the external medium (i.e., the antenna insulation and borehole-filling material for the crosshole GPR case) have significantly lower dielectric permittivities than the external medium, a realistic current distribution on an insulated antenna may be obtained analytically (King and Smith, 1981; King et al., 1983). Under these conditions, the antenna can be treated as a short-circuited transmission line and characterized by equations (3.10) and (3.11), but with a characteristic impedance that is complex

and frequency-dependent, and a wave number different from that of the surrounding medium. These results were used by Sato and Thierbach (1991) in their analytical formulation of crosshole GPR transmission and reception. However, as mentioned previously, this approach is valid only for modeling in the vadose zone, as in the saturated zone, the material present in the borehole (water) has a significantly higher dielectric permittivity than the surrounding earth.

To determine realistic current behavior for crosshole GPR antennas in both air- and water-filled boreholes, without any assumptions or approximations, we use a detailed FDTD modeling approach in 2-D cylindrical coordinates. In a similar manner to Ernst et al. (2005) and Ellefsen and Wright (2005), we model explicitly the transmitter antenna and borehole using a fine spatial discretization. We then simulate transmission on the antenna and examine the current distribution. To reduce computing time, we limit the extent of our model to a small region around the borehole. Figure 3.5 shows the modeling domain that we consider for this approach. The antenna wire, with diameter d_{wire} and electrical conductivity σ_{wire} , contains a small, 1 mm feed gap at the center. The wire is surrounded by lossless insulation having external diameter d_{ins} and dielectric constant κ_{ins} . The borehole, with diameter d_{bh} , is characterized by either $\kappa_{bh} = 1$ and $\sigma_{bh} = 0$ mS/m (air-filled), or $\kappa_{bh} = 80$ and $\sigma_{bh} = 1$ mS/m (water-filled). The surrounding medium has electrical properties κ_{med} and σ_{med} . For all materials, we assume that the magnetic permeability equals its free space value, μ_0 . To feed the antenna and represent the correct impedance contrast at the input terminals, we attach a 1-D transmission line that is terminated at the far end with an absorbing boundary condition (Maloney et al., 1994; Lampe et al., 2003). The voltage excitation function is then introduced into the line through a one-way injector. To obtain the current on the antenna from the FDTD modeling results, we apply the integral formulation of Ampere's Law to the H_ϕ field nodes located just outside the antenna wire.

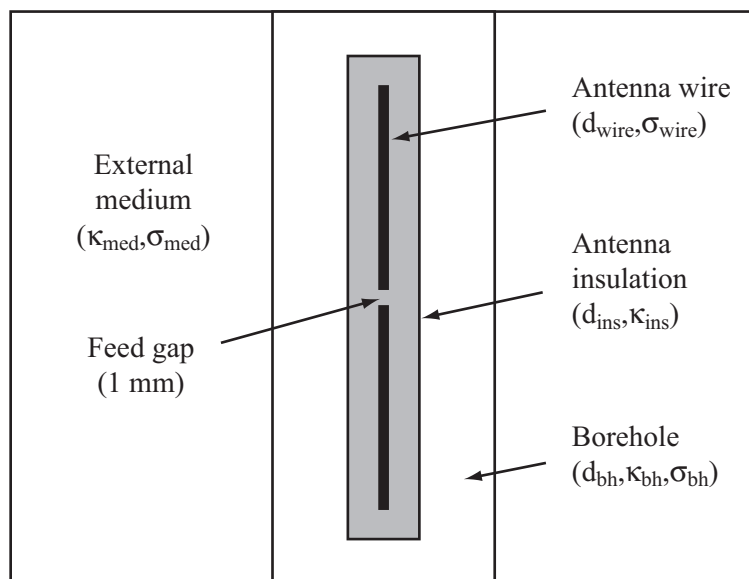


Figure 3.5: Modeling domain used to determine the behavior of the current on a realistic borehole GPR antenna.

Figure 3.6 shows the antenna current that we obtained using this approach for a 2-m-long, insulated dipole located in a 5-cm-diameter, air-filled borehole and excited by a Gaussian pulse with $\tau = 1$ ns. This borehole diameter is typical of the PVC-cased piezometer wells that we commonly use for our crosshole GPR work. The surrounding earth had $\kappa_{med} = 9$ and $\sigma_{med} = 1$ mS/m. The antenna wire was modeled as a copper cylinder with $d_{wire} = 5$ mm and $\sigma_{wire} = 5 \times 10^7$ S/m. For the insulation, we used $d_{ins} = 30$ mm and $\kappa_{ins} = 4$. These specifications approximately model the cross-section of our commercial borehole GPR antennas. The characteristic impedance of the 1-D feeding transmission line was set to 50Ω . Figure 3.6 shows that, as described previously, a pulse of current travels back and forth on each arm of the antenna in response to the excitation voltage pulse. In contrast to the simple cases considered earlier, however, these pulses can be seen to undergo significant broadening as they propagate due to the presence of the antenna insulation and borehole. This shows that we cannot ignore dispersion that occurs along the antennas when modeling crosshole

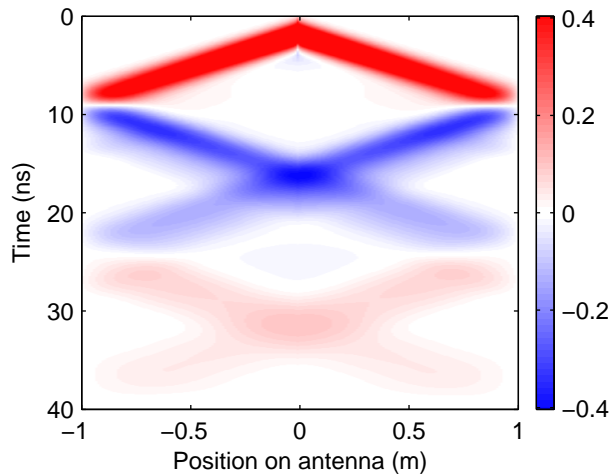


Figure 3.6: Normalized transmitter antenna current for an insulated, 2-m-long, dipole antenna located in a 5-cm-diameter, air-filled borehole and surrounded by earth having $\kappa_{med} = 9$ and $\sigma_{med} = 1$ mS/m. Results were determined using a finely discretized FDTD simulation with the outer boundary set 0.5 m away from the antenna axis.

GPR. For the case of a water-filled borehole, the dispersion was found to be even more significant than shown here. Also important in Figure 3.6 is the fact that the velocity of the current pulses on the antenna is 0.14 m/ns, which is significantly greater than the EM-wave velocity of the surrounding earth (approximately 0.1 m/ns). Clearly, the antenna insulation and borehole have a marked effect on the antenna current distribution, and thus transmission and reception.

To model crosshole GPR using our approach, the actual current on the antennas is not required, but rather the antenna current impulse response $A(z, t)$. However, FDTD modeling using a true impulse voltage excitation to obtain $A(z, t)$ would require an extremely fine spatial discretization because of the high frequency components involved and the fact that 10 grid points per minimum wavelength are required to control numerical dispersion. To obtain a reasonable approximation to $A(z, t)$ for our purposes, we compute the antenna current as described above using a Gaussian

excitation pulse whose frequency spectrum is essentially white over the bandwidth of the transmitter excitation pulse of interest. We have found that setting $\tau = 0.1$ ns in equation (3.16) yields a good approximation to $A(z, t)$ for crosshole GPR modeling. In addition, we have found that $A(z, t)$ is relatively insensitive to moderate fluctuations in the electrical properties of the earth surrounding the antennas; that is, the antenna current behavior is much more dependent upon the properties of the insulation and material filling the borehole. As a result, $A(z, t)$ often need be computed only once, using an average value for the earth's electrical properties, to adequately model an entire crosshole GPR survey.

3.4 Comparison with analytical, numerical, and field results

To validate our modeling approach, we now compare results that we have obtained using our code with analytical results, numerical modeling results where the transmitter antenna and borehole have been explicitly discretized, and crosshole GPR field data. For all cases, 0.8-m-long dipole antennas were considered, which is the length of the frequently employed 100-MHz center frequency antennas in our crosshole GPR system. The transmitter antenna for all cases was located at 10 m depth, and the antenna wire was assumed to be a 5-mm-diameter copper cylinder. A Gaussian excitation pulse with $\tau = 2$ ns (e.g., Sato and Thierbach, 1991) was used for all of the simulations. We believe this to be a good approximation to the voltage pulse delivered by our commercial system transmitter. We normalized each trace in the gathers presented below by the maximum value in order to allow for easier comparison of the individual waveforms, whose amplitudes decrease significantly at high propagation angles. In each case, the absolute amplitudes of the data being compared were in

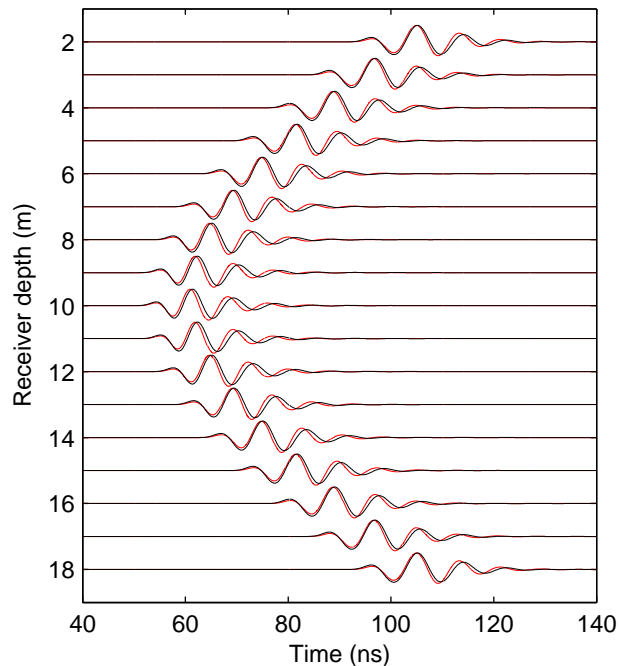


Figure 3.7: Comparison of received waveforms computed using our approach (black) and determined analytically using the method of Sato and Thierbach (1991) (red).

excellent agreement.

Figure 3.7 compares the receiver load waveforms obtained using our code with the analytical results of Sato and Thierbach (1991) for the case where the antennas were situated in 5-cm-diameter, air-filled boreholes and surrounded by a homogeneous medium having $\kappa_{med} = 9$ and $\sigma_{med} = 1$ mS/m. For this example, the borehole separation was 5 m. The modeled antennas were not insulated (i.e., $d_{ins} = d_{wire}$) because the formulation presented by Sato and Theirbach considers only one material between the antenna wire and the surrounding earth. Their approach could be extended to include both the antenna insulation and borehole-filling material using the results of King et al. (1983). As seen in Figure 3.7, there is excellent agreement between our results and the analytical solution.

In Figure 3.8, we compare the radiated E_z field determined using our approach with that obtained by explicitly modeling the transmitter antenna and its borehole using a very fine spatial discretization, in a similar manner to Ernst et al. (2005) and Ellefsen and Wright (2005). We examined four cases, which represent 5-cm- and 10-cm-diameter boreholes in vadose- and saturated-zone environments. In all of these cases, the insulated antenna profile used for Figure 3.5 was employed. The E_z field was recorded at points along a vertical line 3 m away from the transmitter borehole. In the vadose-zone examples (Figures 3.8a and 3.8b), the borehole was air-filled and surrounded by a homogeneous medium having $\kappa_{med} = 9$ and $\sigma_{med} = 1$ mS/m. Here, we see that our results are nearly identical to those determined through detailed FDTD modeling. In the saturated zone examples (Figures 3.8c and 3.8d), the borehole was filled with water and the surrounding medium had $\kappa_{med} = 25$ and $\sigma_{med} = 5$ mS/m. Again, the results obtained using the two approaches are in excellent agreement. Clearly, in accounting for the transmitter antenna and borehole by replicating the antenna current behavior on a significantly coarser grid, we are able to obtain the radiated wavefield very accurately.

Recent work has shown that, in addition to affecting the current distribution on an antenna, a water-filled borehole may distort antenna radiation through guided-wave effects (Holliger and Bergmann, 2002; Tronicke et al., 2004; Tronicke and Holliger, 2004). Indeed, there is slightly less agreement between our code and the detailed modeling results for the 10-cm-diameter, water-filled borehole case shown in Figure 3.8d, which we believe is related to this phenomenon. Although the differences between our code and the finely discretized results in Figure 3.8d are minor, it is important to emphasize that our methodology can only account for guided-wave effects to the extent that they affect the antenna current distribution. For some combinations of antenna excitation pulse and borehole diameter in water-filled boreholes, it is possible that guided-wave effects that cannot be modeled with our approach may be more

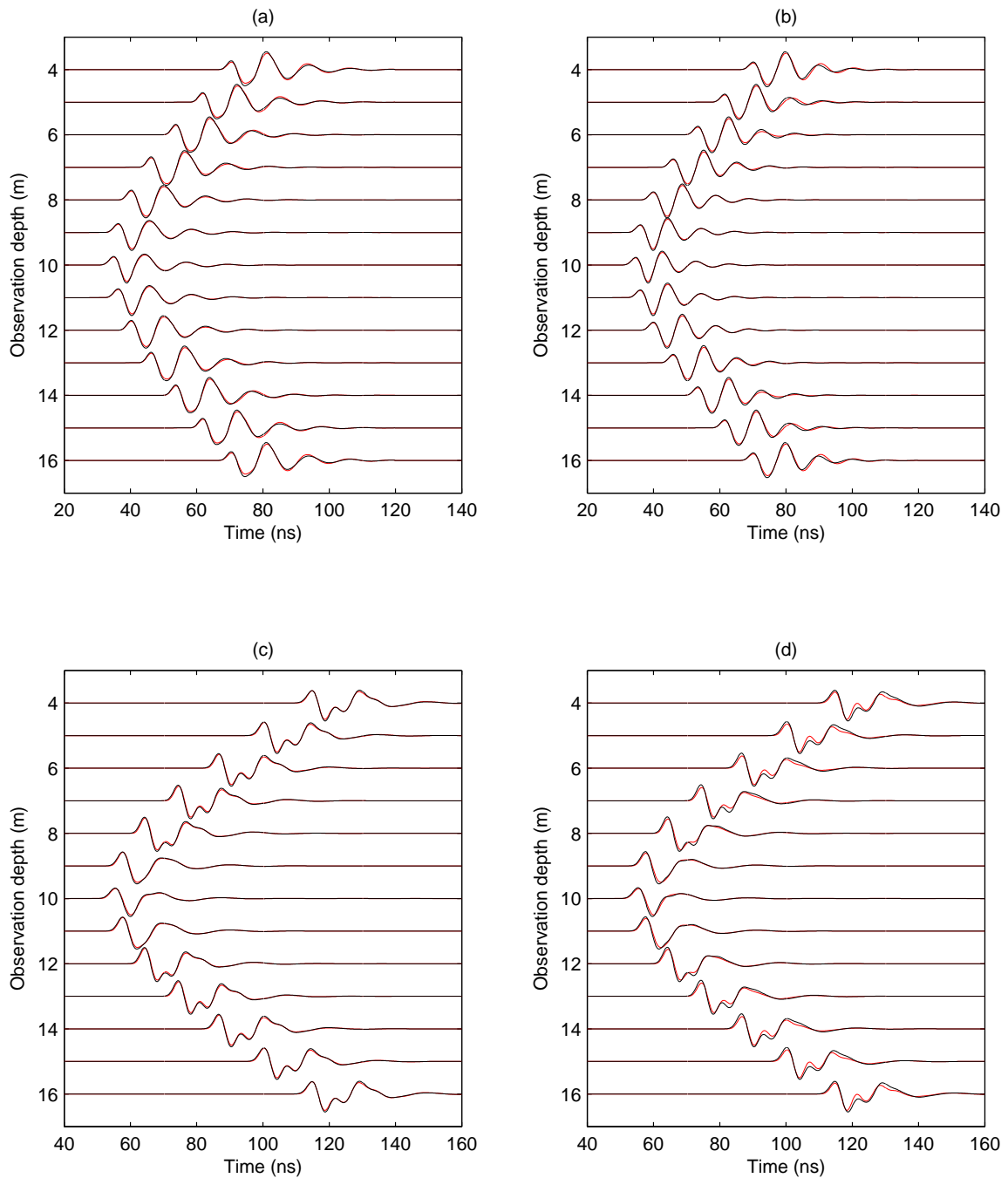


Figure 3.8: Comparison of radiated E_z field computed using our approach (black) and using finely discretized FDTD code with the transmitter antenna and borehole explicitly modeled (red). (a) vadose zone, 5-cm-diameter borehole; (b) vadose zone, 10-cm-diameter borehole; (c) saturated zone, 5-cm-diameter borehole; (d) saturated zone, 10-cm-diameter borehole.

significant than shown here.

As a final example, Figure 3.9 compares results obtained using our code with crosshole GPR field data collected between 5-cm-diameter, air-filled piezometer wells located in a relatively homogeneous, unsaturated, glaciofluvial sand-and-gravel deposit near Abbotsford, BC, Canada. The boreholes were 6 m apart. Again, we modeled the antennas using the insulated antenna profile from Figure 3.5. In addition, to obtain the best match with the field data, constant resistive loading was included along the antennas. This was accomplished by increasing the resistivity of the antenna wire cells in the detailed FDTD simulation that we used to obtain $A(z, t)$. We used an average value of $\kappa_{med} = 6$, which was obtained from first-arrival times in the crosshole data. The conductivity of the sand and gravel was estimated to be 1 mS/m. Figure 3.9 shows our modeling results and the field data to be in good agreement. The received waveforms are very similar except for a slightly broader received pulse in the field data, especially at high angles (i.e., longer travel paths), which we suspect is related to intrinsic dispersion in the sand and gravel. We have not accounted for frequency-dependent material properties in our FDTD code, but including dispersion into the algorithm would be straightforward (e.g., Bergmann et al., 1998).

3.5 Conclusions

Through a relatively simple modification of the FDTD algorithm of Holliger and Bergmann (2002), we can simulate both antenna transmission and reception for cross-hole GPR in heterogeneous media. A significant advantage of our approach is that modeling can be performed very efficiently on a relatively coarse, 2-D grid. In addition, our method allows us to simulate the current behavior on realistic borehole

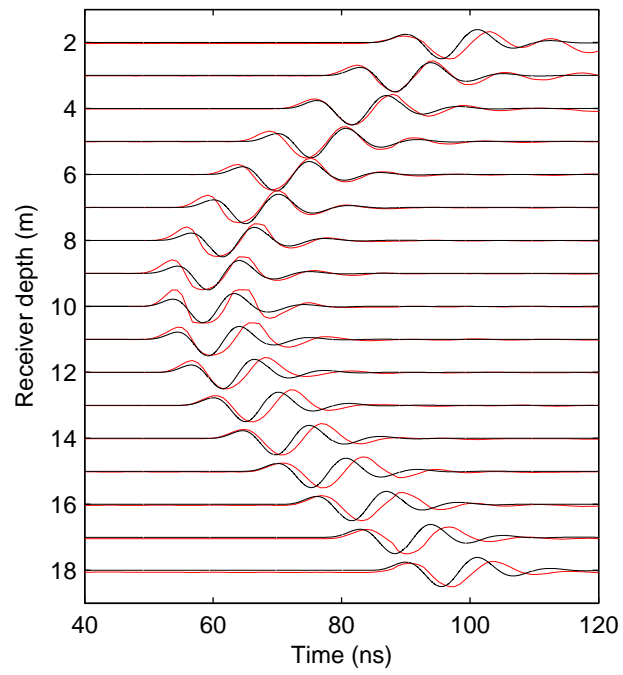


Figure 3.9: Comparison of received waveforms modeled using our approach (black) and recorded in the field in an unsaturated sand-and-gravel aquifer deposit (red).

GPR antennas very accurately because we obtain $A(z, t)$ from a detailed FDTD simulation where the antenna and borehole features are explicitly included. Our next step is to use this modeling approach to develop a full-waveform inversion strategy for crosshole GPR data. Although it has been shown recently that guided-wave effects may significantly affect antenna radiation in water-filled boreholes, our method was able to model radiation in both 5-cm- and 10-cm-diameter, water-filled boreholes very accurately. However, some combinations of borehole diameter and transmitter excitation pulse may produce guided-wave effects that cannot be completely accounted for through the antenna current distribution. If these effects are determined to be important, they could at least be partly accounted for with our code by explicitly modeling the transmitter borehole. Finally, it is likely that our formulation could also be used, with a few modifications, to model transmission and reception in a vertical radar profile (VRP) configuration. This is a topic of future research.

Chapter 4

Effect of antennas on crosshole GPR velocity estimates

4.1 Abstract

In order to obtain tomographic images with the highest possible resolution from cross-hole ground-penetrating radar (GPR) data, raypaths covering a wide range of angles between the boreholes are required. In practice, however, the inclusion of high-angle ray data in crosshole GPR inversions often leads to tomograms so dominated by inversion artifacts that they contain little reliable subsurface information. Here, we investigate the problems that arise from the standard assumption that all first-arriving energy travels directly between the centers of the antennas. Through numerical modeling, we show that this assumption is often incorrect at high transmitter-receiver angles, and can lead to significant errors in tomographic velocity estimates when the antenna length is a significant fraction of the borehole spacing.

4.2 Introduction

Crosshole ground-penetrating radar (GPR) tomography is a popular method for high-resolution imaging of the shallow subsurface. Applications include determination of the location of underground tunnels and voids (Moran and Greenfield, 1993), delineation of orebodies (Fullagar et al., 2000), mapping fractures in bedrock (Olsson et al., 1992), and estimation of subsurface lithology and hydrogeological properties using field- or laboratory-derived petrophysical relationships (Tronicke et al., 2004). The spatial resolution of tomographic images obtained from crosshole GPR data is a critical parameter that determines both the way in which the data are used, and the value of the data, for a specific application.

Of interest in our research is the use of GPR images to quantify the spatial variability of the subsurface for the purpose of predicting contaminant fate and transport. This application requires that our images have the best possible resolution in all directions. In order to obtain tomographic images with such high resolution from crosshole GPR data, raypaths covering a wide range of angles between the boreholes are required. This is a direct consequence of the Fourier projection slice theorem, which states that each set of rays passing through an object at a particular angle (which constitutes a projection) yields one slice of that object's 2-D Fourier spectrum (Rector and Washbourne, 1994). In practice, however, the inclusion of high-angle ray data in crosshole GPR inversions can be problematic (Peterson, 2001; Alumbaugh and Chang, 2002). That is, the inclusion of these data often results in tomograms so dominated by inversion artifacts that they contain little, if any, reliable subsurface information. For this reason, common practice is to limit the aperture of crosshole GPR data sets prior to inversion by discarding rays at angles greater than a particular threshold value (e.g., Alumbaugh and Chang, 2002).

The process of aperture limitation tends to yield reasonable tomographic images

from crosshole GPR data. In our experience, however, it typically requires that we discard all rays at angles above 40 degrees from the horizontal, which is often well below the maximum angle at which first-arrival data can be reliably picked. We are therefore degrading the potential resolution of our images by discarding these rays. We are interested in determining *why* the high angle rays have such a negative effect on the images. Once this has been resolved, it may be possible to find a means of properly incorporating these data into crosshole GPR inversions.

In this study, we explore the idea that a key assumption, currently employed in the inversion of all crosshole GPR data, is invalid for high-angle rays. Crosshole GPR inversion strategies treat the antennas as point sources and receivers whose locations are given by the antenna midpoints. That is, these strategies effectively ignore the length of the antennas, and assume that all first-arriving energy travels directly between the antenna centers. In many cases, however, the antenna length is a significant fraction of the separation distance between the boreholes. Here, we use numerical modeling to investigate whether, for large vertical offsets between the transmitter and receiver antennas, first-arriving energy can sometimes travel between the antenna tips.

4.3 Velocity along a borehole GPR antenna

A key parameter in assessing the travel path of electromagnetic (EM) waves in a crosshole GPR experiment is the velocity at which energy travels along the borehole antennas, v_{ant} , relative to the velocity of EM waves through the medium between the boreholes, v_{med} . Because the borehole antenna wires are not simply embedded within the earth in a crosshole GPR experiment, but rather are surrounded first by the antenna insulation and then the borehole filling material, these two velocities are usually quite different. If $v_{ant} \leq v_{med}$, then the first-arriving energy at all transmitter-receiver

angles should be that traveling directly between the antenna centers. In contrast, if $v_{ant} > v_{med}$, then the possibility exists at high transmitter-receiver angles for the first-arriving energy to travel between the tips of the antennas. More specifically, it is possible in this case that the first-arriving energy (i) travels from the center feed point along the transmitter antenna to the tip at velocity v_{ant} , (ii) is radiated from the tip of the transmitter antenna, (iii) travels through the subsurface at velocity v_{med} , (iv) is received at the opposite tip of the receiver antenna, and (v) travels along the receiver antenna from the tip to the center input terminal at velocity v_{ant} .

The physics governing the propagation of energy along an insulated antenna in a borehole are very complex, and involve the solution of Maxwell's equations in cylindrical coordinates subject to boundary conditions at the various interfaces surrounding the antenna wire. In general, the velocity of energy traveling along a borehole GPR antenna will be most sensitive to the material closest to the antenna wire (i.e., the antenna insulation) and less sensitive to material further away. For an excellent treatment of the theory of insulated antennas, along with a derivation of the propagation constant on such an antenna under certain limiting assumptions, the reader is referred to King and Smith (1981) and King et al. (1983). Unfortunately, the assumptions required for the propagation constant derivation are too restrictive for our purposes. We therefore determine the velocity of energy along a borehole GPR antenna using a numerical modeling approach.

Figure 4.1 shows the ratio of the antenna velocity to external medium velocity (v_{ant}/v_{med}) that we have calculated for a realistic borehole GPR antenna in a variety of vadose and saturated zone situations. To create this plot, we first constructed a finely discretized finite-difference time-domain (FDTD) model of the antenna and its immediate surroundings in 2-D cylindrical coordinates, based on the approach presented by Holliger and Bergmann (2002). This model was then used to obtain the current distribution on the antenna during transmission when it was placed in

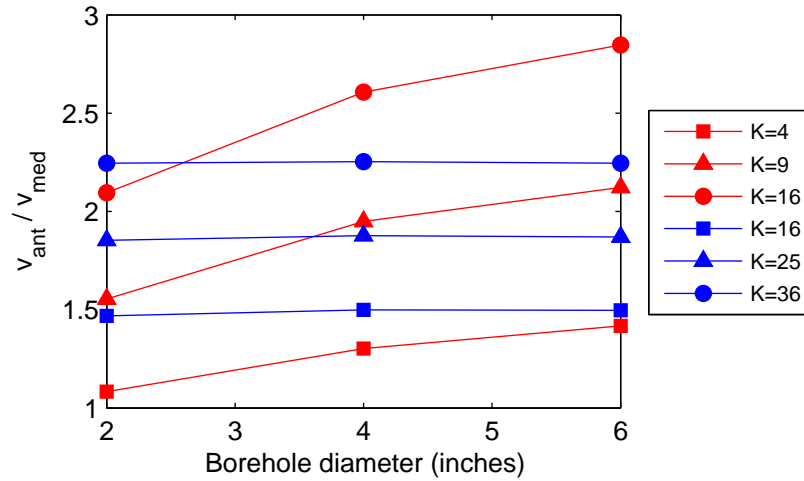


Figure 4.1: Antenna-to-medium velocity ratio (v_{ant}/v_{med}) determined versus borehole diameter for a number of cases in the vadose zone (red, air-filled borehole) and saturated zone (blue, water-filled borehole). κ values represent the dielectric constant of the medium surrounding the boreholes.

air- and water-filled boreholes of various diameters. The boreholes were surrounded by media having different values of the dielectric constant κ . The antenna design used for the simulations was based on the borehole antennas in our commercial GPR system, and consisted of a 5 mm diameter copper cylinder with electrical conductivity $\sigma = 5 \times 10^7$ S/m, surrounded to 30 mm diameter by non-conductive insulation having $\kappa = 4$. To feed the antenna, we applied a Gaussian voltage pulse, having a -20 dB width of approximately 5 ns, to a 1 mm feed gap located at the center of the antenna wire. The antenna velocity was obtained by determining the first-arrival time of the resulting current pulse as it traveled to each point along the antenna.

As shown in Figure 4.1, v_{ant}/v_{med} is much more dependent upon borehole diameter in the vadose zone than in the saturated zone. This is because, in the case of a water-filled borehole, the borehole acts as a dielectric waveguide and thus the external medium has little influence on the velocity of energy along the antenna (Holliger and Bergmann, 2002). More important, however, is the fact that for most of

the cases considered, Figure 4.1 clearly shows that v_{ant}/v_{med} is significantly greater than 1. Surprisingly, this is even the case in a water-filled borehole. The antenna insulation (a fast dielectric) is evidently thick enough to allow energy to propagate along the antenna at a velocity greater than that of the saturated external medium, despite being surrounded by water (a very slow dielectric). Figure 4.1 thus indicates that, for the insulated antenna that we have considered, it will often be possible at high transmitter-receiver angles for energy traveling between the tips of the antennas to arrive before that traveling directly between their centers. In the next section, we evaluate the implications of this result for crosshole GPR tomography, and find that significant errors in velocity estimates can occur when this phenomenon is not addressed.

4.4 Crosshole GPR modeling results

4.4.1 Homogeneous medium

We first consider a crosshole GPR experiment where the medium between the boreholes is homogeneous with $\kappa = 25$. This is a typical value of the dielectric constant for earth materials located in the saturated zone. We generate synthetic crosshole GPR data through this medium using finite-length antennas. We then examine the errors that can result in velocity estimates obtained from the synthetic data when it is assumed that first-arriving energy always travels directly between the antenna centers.

To numerically simulate transmission and reception between realistic, finite-length, borehole GPR antennas, we use a superposition of point dipole source and receiver responses in 2-D cylindrical coordinates (Irving and Knight, 2006b). Results obtained using this technique have been shown to be in excellent agreement with analytical,

field, and finely discretized numerical modeling results. For all of the examples in this study, we also simulated moderate resistive loading on the antennas such that the waveforms produced were similar to crosshole waveforms that we have recorded with our commercial GPR system. Borehole GPR antennas tend to be resistively loaded, but only lightly, in order to obtain a compromise between a short radiated pulse and maximum power transfer into the ground.

Figure 4.2 shows the velocity error that results at different transmitter-receiver angles when it is assumed that first-arriving energy travels directly between the centers of the antennas. This error was determined using the following equation:

$$\% \text{ error} = \frac{v_{meas} - v_{true}}{v_{true}} \times 100, \quad (4.1)$$

where v_{meas} is the velocity measured from the synthetic data using the picked first-arrival time, and v_{true} is the known velocity of the medium between the boreholes (in this case, 0.06 m/ns).

Modeling was performed for a number of different cases corresponding to variations in v_{ant}/v_{med} , the borehole separation distance, and the length of the transmitter and receiver antennas. The flat-lying solid red curve in Figure 4.2 corresponds to the case where the velocity along the antennas was set equal to the velocity of the surrounding medium (i.e., $v_{ant}/v_{med} = 1$). As expected, there is no error in the measured velocity with angle. A very different behavior is observed, however, for all of the other curves shown in Figure 4.2. In these cases, there are no errors in the measured velocities for low propagation angles between the antennas, but errors clearly exist at higher angles as a result of our assumption that first-arriving energy travels directly between the antenna centers. For low transmitter-receiver angles, this assumption is valid. At higher angles, however, energy traveling between the antenna tips arrives first, which results in a measured velocity that is greater than the true velocity of the medium.

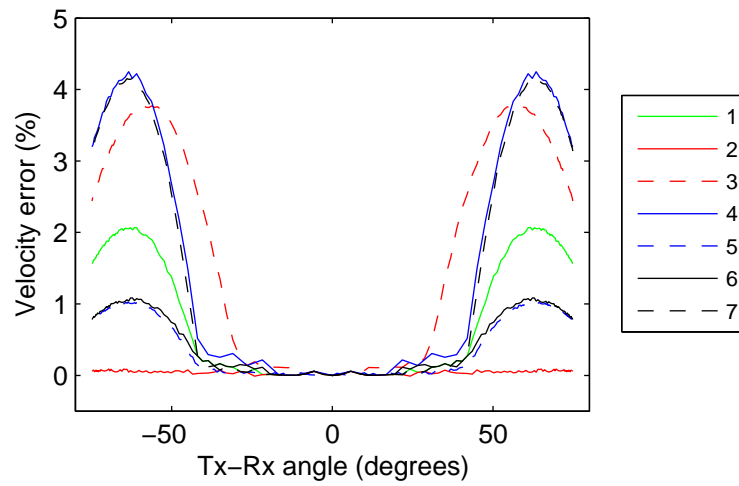


Figure 4.2: Velocity error versus transmitter-receiver angle (measured from the horizontal) determined from numerical simulations of finite antennas in a homogeneous medium having $\kappa = 25$. (1) $v_{ant}/v_{med} = 1.5$, borehole separation = 4 m, antenna length = 0.8 m; (2) $v_{ant}/v_{med} = 1.0$; (3) $v_{ant}/v_{med} = 2.0$; (4) borehole separation = 2 m; (5) borehole separation = 8 m; (6) antenna length = 0.4 m; (7) antenna length = 1.6 m.

We now consider the magnitude of the errors in Figure 4.2. The green curve in the figure was created using a conservative antenna-to-medium velocity ratio of 1.5, 0.8 m long antennas (which is the length of the 100 MHz antennas in our commercial borehole GPR system), and a borehole separation of 4 m. These parameters are typical of many crosshole GPR surveys, and result in an error in velocity of 2% at some transmitter-receiver angles. As we will see in the next section, a consistent error of this magnitude can have significant effects on the tomograms obtained from crosshole GPR data. All of the other curves shown in Figure 4.2 represent a perturbation of one of the three parameters described above from the values used for the green curve. From these results, we see that the velocity error associated with high-angle rays is greatest for large values of v_{ant}/v_{med} , small borehole separations, and longer (i.e., lower frequency) antennas.

4.4.2 Heterogeneous medium

We now consider crosshole GPR data acquired through the heterogeneous medium shown in Figure 4.3a. This velocity model was constructed using the geostatistical software package GSLIB (Deutsch and Journel, 1992). A range of $20 \leq \kappa \leq 32$ was chosen to represent earth materials in the saturated zone. The boreholes located on either side of the model are 4 m apart and 12 m deep. The transmitter and receiver locations were spaced every 0.25 m down the boreholes from 0.5 m to 11.5 m. To produce all of the tomograms for this example, we again assumed that all first-arriving energy travels directly between the antenna centers. In addition, straight rays were assumed in all of the inversions and a Laplacian smoothness operator was employed for regularization purposes. The same parameters were used in each inversion so that differences between the resulting tomograms could be fully attributed to differences between the antennas and apertures used.

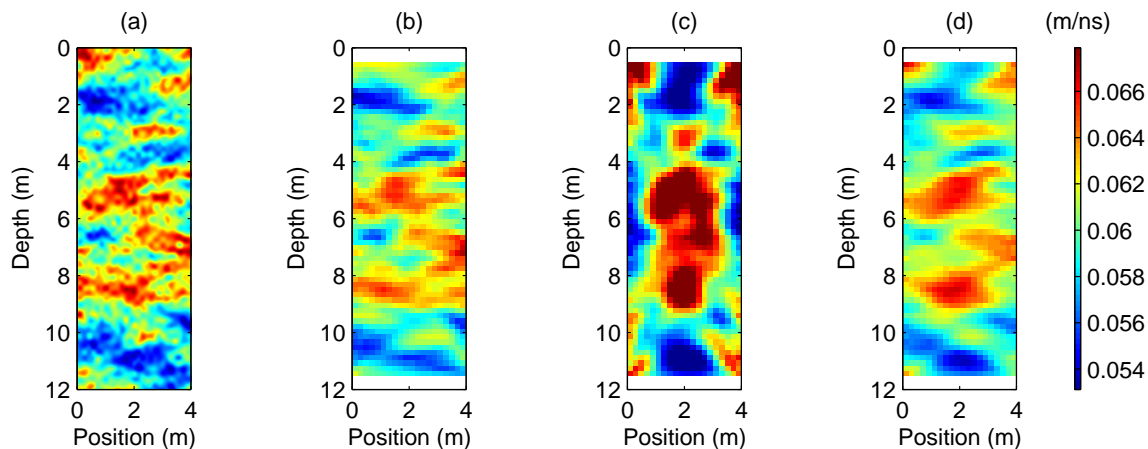


Figure 4.3: Heterogeneous medium example. (a) true velocity model; (b) velocity tomogram obtained from synthetic data created using point dipole antennas; (c) velocity tomogram obtained from synthetic data created using realistic, finite-length antennas; (d) velocity tomogram obtained from aperture-limited finite-antennas data, where rays at angles greater than 40 degrees from the horizontal were discarded.

We first generated synthetic crosshole data through the velocity model in Figure 4.3a using point dipole sources and receivers, so that all first-arriving energy would truly travel between the antenna centers. This was done using the modeling approach of Holliger and Bergmann (2002) with a 100 MHz Ricker wavelet source function. Figure 4.3b shows the inversion result for the point source and receiver data using all available travel times, which involved rays at angles up to 70 degrees from the horizontal. There is excellent agreement between Figure 4.3b and the true velocity model in Figure 4.3a due to the agreement between our forward model and inversion procedure on the path taken by first-arriving energy, and the wide angular coverage provided by the data set.

We next generated synthetic crosshole GPR data through the velocity model in Figure 4.3a using 0.8 m long, finite-length antennas with $v_{ant} = 0.09$ m/ns, which is 1.5 times the average subsurface velocity of 0.06 m/ns. These parameters, along

with the borehole separation of 4 m, are the same as those used to create the green curve in Figure 4.2. Figure 4.3c shows the tomogram obtained from the finite-length antennas data. Here, we see that the tomogram is dominated by inversion artifacts to the extent that no reliable information about the subsurface can be inferred. As in Figure 4.3b, rays at all available angles were included in this inversion. It is the velocity errors associated with the high-angle rays, due to the incorrect assumption about first-arriving energy, that cause the severe artifacts seen in Figure 4.3c.

Figure 4.3d clearly illustrates the impact of the velocity errors at high transmitter-receiver angles on the tomogram. For this figure, all rays at angles greater than 40 degrees from the horizontal were discarded from the finite-length antennas data before inversion. Notice that we now obtain a reasonable tomographic image because we avoid the errors associated with the high-angle rays. However, the resolution of this image is reduced when compared to Figure 4.3b because of the decreased angular aperture. For many applications, this loss of resolution may be critical. To further quantify the accuracy of the recovered velocity models in Figures 4.3d and 4.3b, we calculated the root-mean-square (RMS) error between each tomogram and the true velocity model shown in Figure 4.3a. Figure 4.3b has an RMS velocity error of 1.1×10^{-3} m/ns, whereas the RMS error for Figure 4.3d is greater at 1.5×10^{-3} m/ns.

4.5 Conclusions

Through numerical modeling we have shown that, at high propagation angles between the transmitter and receiver antennas in crosshole GPR tomography, energy traveling between the tips of the antennas can often arrive before that traveling between their centers. This can occur in both the vadose and saturated zones, and contradicts the assumption of present inversion strategies that first-arriving energy always travels directly between the antenna centers. Consequently, significant errors in tomographic

velocity estimates can result when high-angle ray data are included in inversions. These errors will be greatest for small borehole separations and lower-frequency antennas.

It should be noted that the results shown here are not restricted to perfectly electrically conducting (PEC) type antennas. As stated previously, moderate resistive loading along the antennas was included for all of the examples presented, such that the modeled waveforms were similar to those that we have recorded with our commercial borehole GPR system. However, we acknowledge that greater resistive loading in a progressive manner, such as in a Wu-King configuration (Wu and King, 1964), would likely reduce the magnitude of the errors shown here, as antennas loaded in this manner tend to act as very short dipoles. To our knowledge, this type of resistive loading is uncommon in commercial borehole GPR antennas because it does not permit sufficient energy transfer into the ground.

Finally, we do not suggest that all difficulties associated with high-angle ray data in crosshole GPR tomography are related to the assumption that first-arriving energy travels directly between the antenna centers. There are lower signal-to-noise ratios associated with these data that will contribute to greater picking errors and thus less accurate inversion results as well. However, the errors resulting from the assumption about first-arriving energy can, alone, have a major impact on the quality of tomograms obtained from crosshole GPR data. Now that we understand the effect of the antennas on inversion results, finding a way to properly include the high-angle ray data becomes a feasible and important objective for future research.

Chapter 5

Strategies for improving crosshole GPR travel-time tomography at close borehole spacings

5.1 Abstract

Crosshole ground-penetrating radar (GPR) travel-time tomography between closely spaced boreholes presents a number of significant challenges to the GPR practitioner. One of these is that the accurate picking of high-angle ray data, which are necessary to obtain the highest resolution tomographic images, is often extremely difficult because of low S/N in the data. Another challenge is that, even when high-angle travel times are available, they often appear to be incompatible with lower-angle ones at close borehole spacings, and cause significant numerical artifacts when included in inversions. Although an easy solution to both of these problems is to simply ignore the high-angle ray data, such a strategy effectively limits the horizontal resolution of the images that are obtained, which may be critical depending on the end use of

the data. Here, we attempt to deal with these problems more completely, and first present a travel-time picking strategy based on cross-correlations that is suitable for noisy, high-angle data. High-quality reference waveforms for the cross-correlations are obtained by stacking aligned common-ray-angle gathers. Next, we discuss how tip-to-tip antenna coupling, interference between feed- and end-radiated pulses, and propagation dispersion can result in problems experienced with high-angle rays at close borehole spacings, and using the fact that all of these mechanisms cause errors in velocity as a function of angle, we develop a modified inversion procedure: In addition to estimating subsurface EM-wave velocities, we invert for a small number of parameters that describe a travel-time correction curve as a function of angle. Using this methodology, we show the improved inversion of synthetic crosshole GPR data, and also field data collected between closely spaced wells at the Boise Hydrogeophysical Research Site (BHRS).

5.2 Introduction

Crosshole ground-penetrating radar (GPR) travel-time tomography is a popular geophysical method for high-resolution imaging of the subsurface in terms of its electromagnetic (EM) wave velocity. With this method, a short EM pulse is radiated from a transmitter antenna, located in one borehole, and recorded at a receiver antenna, which is located in an adjacent borehole. The first-break travel times of energy for various configurations of the two antennas are then picked and inverted to obtain an image of the distribution of velocity between the boreholes. Because of the strong contrast that exists between the EM-wave velocity of water (0.33 m/ns) and that of dry earth materials (~ 0.15 m/ns), the velocities obtained with crosshole GPR tomography are highly correlated with water content in the subsurface. For this reason, the technique is commonly used to detect differences in porosity in the saturated zone,

and differences in soil water retention (and thus grain size) in the vadose zone. Of interest in our research is the use of such information in the development of numerical models for groundwater flow and contaminant transport. For this application, the resolution of the crosshole GPR images we obtain is critical.

In environmental applications, crosshole GPR tomography is commonly performed between boreholes that are spaced quite closely together (on the order of a few meters) (e.g., Peterson, 2001; Alumbaugh and Chang, 2002; Tronicke et al., 2002). At such borehole spacings, the potential exists in theory for excellent tomographic resolution. This is because, even for the relatively shallow (~ 20 m) borehole depths typical of environmental applications, close borehole spacings allow for wide angular coverage of the inter-borehole region, which is a key requirement for high-resolution imaging with ray-based tomography. In practice, however, two significant problems are encountered when trying to take advantage of this wide angular coverage. First, the arrival times of energy traveling at high transmitter-receiver angles are often very difficult to pick because of low S/N in the data. This results not only because of an increased amount of attenuation at high angles due to longer travel paths, but also because of the radiation patterns of the GPR antennas, which approximately follow a half-cosine distribution with the maximum perpendicular to the antenna elements. Secondly, when high-angle travel times are available at close borehole spacings, difficulties are commonly encountered when attempting to incorporate these data into crosshole GPR inversions. Specifically, the high-angle data often appear to be incompatible with travel times corresponding to lower transmitter-receiver angles, and cause significant numerical artifacts in the resulting tomograms (Peterson, 2001; Alumbaugh and Chang, 2002; Irving and Knight, 2005b). As we will show, this incompatibility cannot be simply explained by decreased picking accuracy at high angles, reasonable geological anisotropy, or survey measurement errors.

At the present time, the strategy for dealing with the two problems mentioned

above is quite simple. Because travel times at high transmitter-receiver angles are often difficult to pick and can cause significant inversion artifacts at close borehole spacings, they are generally excluded from the tomographic imaging process. Doing this allows for reasonable tomograms to be obtained from the data; however, it comes at the expense of horizontal resolution. Because, without the high-angle rays, we have little information constraining lateral variability in the subsurface, the tomograms obtained in this manner tend to be significantly smoothed in the horizontal direction. For some applications of the images such as ours, this lack of horizontal resolution may be a serious drawback. As a result, it has been our goal to understand in more detail the high-angle problem at close borehole spacings, and develop improved picking and inversion methods for crosshole GPR data in order to obtain higher-resolution tomograms.

In this paper, to address the high-angle picking problem, we present a strategy for determining first-break times in crosshole GPR data using cross-correlations. Our methodology allows for the robust and automatic picking of first breaks in data having very low S/N, and is best suited to subsurface environments lacking extreme velocity contrasts (interference between the direct and scattered arrivals in such environments is minimal). We show the application of this picking methodology to crosshole GPR data collected at the Boise Hydrogeophysical Research Site (BHRS) near Boise, Idaho. Next, we address the nature of the incompatibility problem with high-angle ray data, and discuss a number of factors, other than simple coordinate mislocations and transmitter fire-time errors, that can result in apparent variations in measured velocities as a function of angle. Although these factors have a minimal effect at large borehole offsets, they can cause significant problems when boreholes are spaced closely together. Finally, using this information, we develop an inversion algorithm for data collected at close borehole spacings that allows all of the available travel times (high- and low-angle) to be effectively used. We show the results of successfully

applying this inversion technique to synthetic crosshole GPR data, and also to the picked field data set from the BHRS.

5.3 Cross-correlation picking of travel times

As mentioned, one theoretical advantage of crosshole GPR data collected between closely spaced boreholes is that high-angle raypaths are available, and the potential thus exists for wide angular coverage of the inter-borehole region. However, often the S/N in data acquired along such raypaths is very low and it is extremely difficult, if not impossible, to determine the first breaks manually or using automated techniques such as finding where the amplitude on a trace first reaches some threshold value, and then backing off by a prescribed amount. As an example, Figure 5.1 shows a common-receiver gather from a 250 MHz crosshole GPR data set that was collected between wells A1 and B2 (~ 3.5 m apart and cased with 4-inch-diameter PVC) at the BHRS. In this gather, the receiver antenna was located at a depth of 5.33 m, and the transmitter antenna was moved from 3.72 to 18.04 m depth. All traces in the gather have been normalized by their maximum amplitudes for easier comparison. Notice in the figure that, when the depths of the antennas are similar (near the top of the plot), the recorded waveforms have a very strong S/N and picking of the first breaks is straightforward; on the uppermost trace, the first break occurs just before the small positive peak located at approximately 55 ns. However, as the transmitter depth (and thus the angle between the antennas) increases, the S/N worsens to the point where, near the bottom of Figure 5.1, this first-arriving peak cannot even be seen, let alone picked. Although low-pass filtering may be of some help in attempting to pick such noisy data, the large amount of filtering required for very noisy traces can often significantly affect the apparent onset of signal. Another idea might be to pick the point of maximum amplitude on the traces and then back off to obtain the first

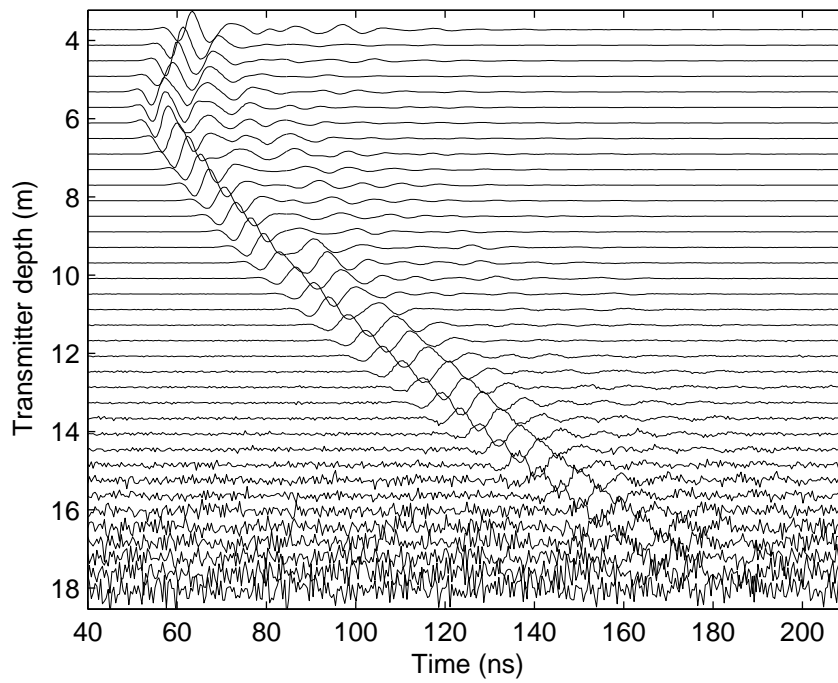


Figure 5.1: Common-receiver gather showing the difficulties in picking first-break times at large transmitter-receiver offsets due to low S/N. Receiver depth is 5.33 m. All traces have been normalized by their maximum value.

breaks. However, such picking is not robust, and more importantly the position of the first break with respect to the trace maximum will vary with transmitter-receiver angle because the GPR waveform changes with angle. Clearly, signal is present in the lower traces of Figure 5.1; its onset is simply overshadowed by noise. The question is: how do we use what signal is there to estimate the first arrivals?

One solution for the robust estimation of travel times in the presence of significant noise, that has been widely used in earthquake and other studies, is the cross-correlation technique (e.g., Peraldi and Clement, 1972; VanDecar and Crosson, 1990; Woodward and Masters, 1991; Molyneux and Schmitt, 1999). With this method, the discrete cross-correlation of a trace and a high-quality reference waveform (having known arrival time) is determined, and the difference in travel time between the two signals is then obtained from the time shift at which the value of the cross-correlation is a maximum. Ideally, the reference waveform used with this technique should be noise-free and have the same shape as the waveform present on the trace in question. Although synthetics are often used to obtain such a waveform in earthquake studies, we instead choose to obtain reference waveforms for the cross-correlation picking of GPR data from the data themselves. We have found that synthetic modeling requires too much knowledge about system, antenna, and earth parameters to yield waveforms that are sufficiently close enough to those in field data for effective cross-correlation analysis. To obtain the reference waveforms from the data, we stack traces that have been aligned on the first arrival. Because the GPR pulse changes with transmitter-receiver angle (a result of variations in antenna radiation and reception with angle, and also propagation dispersion along travel paths having different lengths), we determine a number of different reference waveforms that represent ranges in angle where the arriving pulses have similar shape.

Figure 5.2 is a flowchart illustrating the sequence of steps involved in our cross-correlation picking procedure. The crosshole GPR data are first pre-processed by

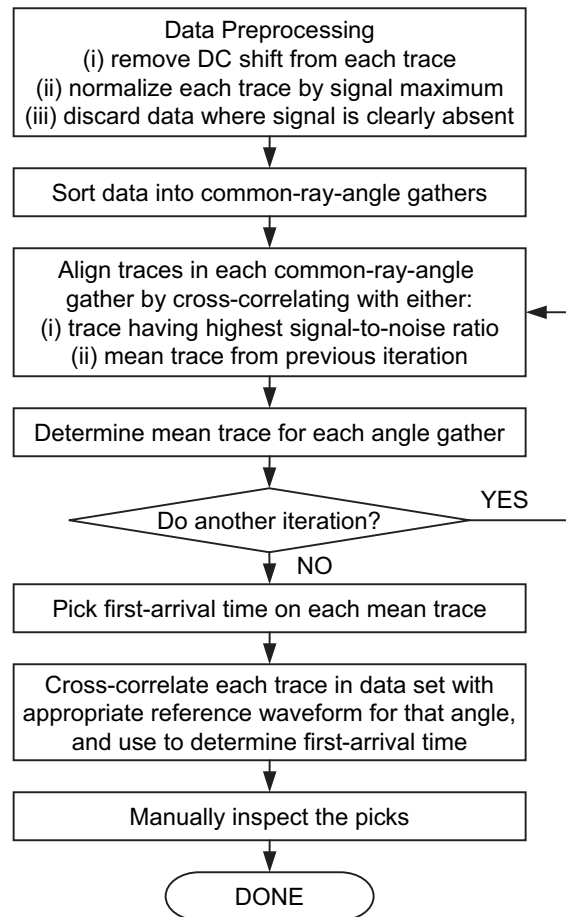


Figure 5.2: Flowchart of our cross-correlation picking procedure.

removing any DC offset from each trace (determined from the mean value of the trace before the onset of signal) and by normalizing each trace by the signal maximum (estimated by low-pass filtering the data and finding the maximum value). If desired, extremely noisy traces with no apparent signal can be discarded straightaway to reduce the number of bad picks obtained with our technique. Next, the crosshole data are sorted into common-ray-angle gathers (e.g., Pratt and Worthington, 1988; Pratt and Gouly, 1991). To do this, we create a set of angle bins and place each trace into the appropriate bin based on the transmitter-receiver angle. To determine a high-quality reference waveform for each angle bin, the waveforms in each gather must be aligned and then stacked. Since aligning the traces requires some means of estimating the relative time shifts between the waveforms, we use cross-correlations, but in an iterative manner as follows: Initially, the traces in a common-ray-angle gather are aligned by cross-correlating them with the trace in the gather having the highest S/N. This places the majority of traces into proper alignment, which then allows for a higher quality waveform to be obtained through stacking. In the second iteration, the traces in the gather are aligned again, but this time by cross-correlating them with the mean trace from the previous iteration. This process is continued until the vast majority of traces in a gather are properly aligned. In practice, we have found that 2 iterations are usually sufficient for this. Once the reference waveforms for each angle range have been determined, their first arrivals are picked manually. The entire crosshole data set is then picked automatically by cross-correlating each trace with the appropriate reference waveform. To increase the robustness of our algorithm, we limit the number of lags used in the cross-correlations to reasonable values (i.e., differences in arrival time between traces and the reference trace should not be too great). As a final step, all of the automatic picks made with our method should be visually checked for accuracy. Bad picks are generally quite obvious, as they tend to be caused by the cross-correlation being maximized when the two signals are

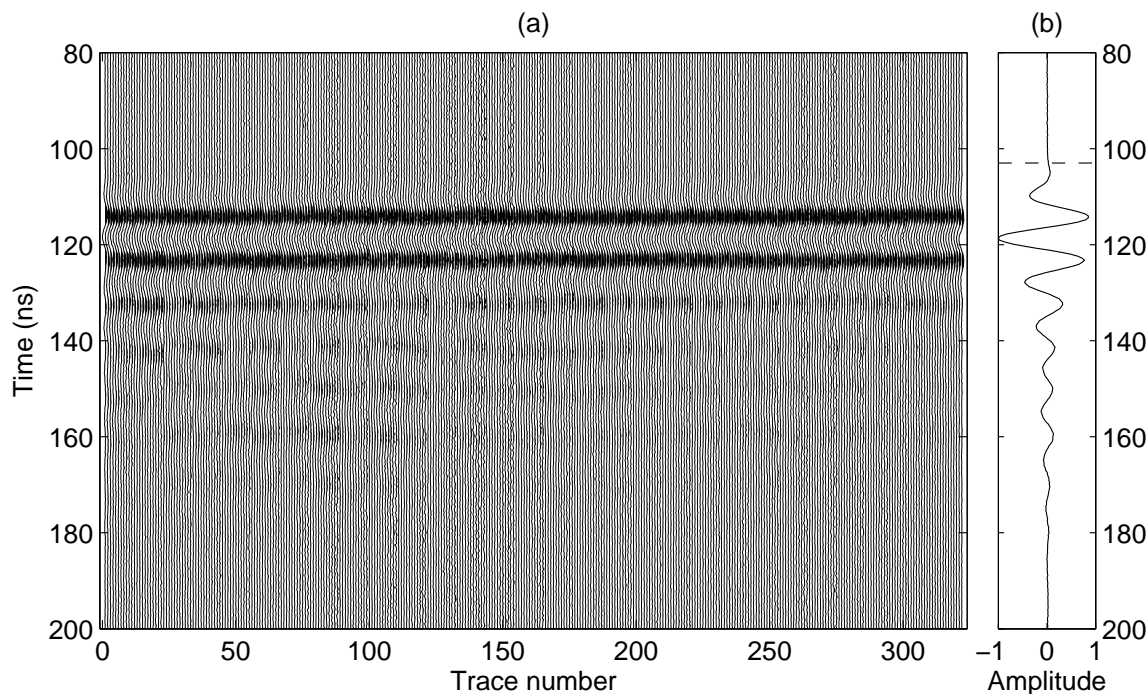


Figure 5.3: (a) Common-ray-angle gather and (b) mean trace for the 65 to 70 degree angle range in the BHRS data set. The picked first-arrival time on the mean trace is indicated with a horizontal dashed line.

mismatched by a full cycle.

As an example, we now show the application of our cross-correlation picking technique to the full BHRS data set from Figure 5.1. Figure 5.3a shows one of the common-ray-angle gathers obtained from the data set for the 65 to 70 degree angle range. Here, transmitter-receiver angle is measured from the horizontal with positive angles representing the case where the receiver is located above the transmitter. Two iterations of cross-correlating were used to align the traces in this high-angle gather. The waveforms in the gather are clearly visible and have very similar shapes, but they are contaminated by significant amounts of noise which makes picking the first breaks extremely difficult. Figure 5.3b, on the other hand, shows the mean trace that was obtained by stacking the 322 traces in Figure 5.3a together. Here, we see that

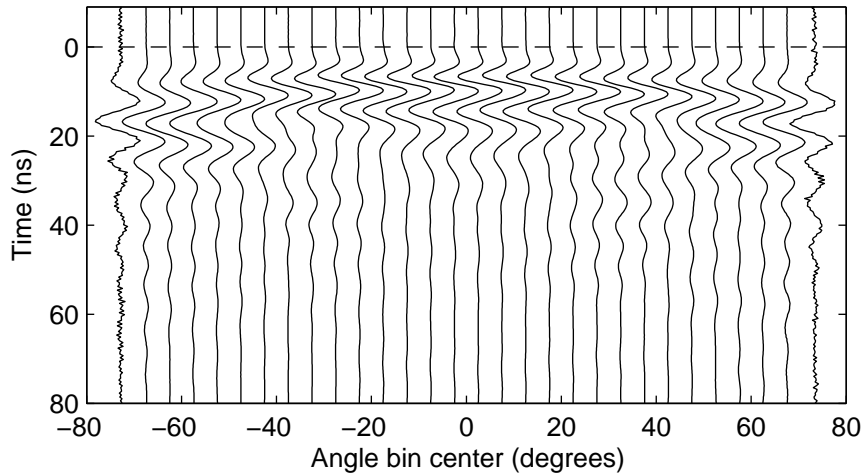


Figure 5.4: Mean traces determined for the BHRS data set by stacking the different common-ray-angle gathers. The traces have been aligned at $t = 0$ on their picked first arrivals and normalized by their maximum value.

the S/N has been greatly increased and that a small, positive, first-arrival peak, not clearly visible on any individual trace, is now easily identified. The much higher S/N of this mean trace, and the fact that its first break can be easily picked, make it an excellent reference waveform for cross-correlation analysis.

Figure 5.4 shows the mean traces that were obtained in the above manner for each angle group in the BHRS data set. The waveforms have been aligned on their manually picked first arrivals for easier comparison. For the BHRS data, angle bins were created for every 5-degree increment from -75 to 75 degrees, which yielded 31 reference waveforms. Figure 5.4 clearly shows why we must determine these waveforms as a function of angle when picking crosshole GPR data, as opposed to using a single reference waveform for the entire data set; there is a significant change in shape of the GPR pulse with angle that must be accounted for. Also notice that all of the reference waveforms in Figure 5.4, including the ones on both ends if scaled enough in amplitude, have first-arrival times that are easily identified.

Finally, Figure 5.5 shows four example receiver gathers from the BHRS data set upon which the first-break times, all determined automatically with our technique, have been superimposed in red. In all of the gathers, the picks are seen to be very reasonable. This is despite the fact that significant noise is present at high transmitter-receiver angles, and in many cases the positive first-arrival peak at these angles cannot even be visually identified. We conclude that picking of the BHRS data using cross-correlations was an effective means of determining first-arrival times.

It is important to note that the picking method described above assumes that waveforms recorded at similar transmitter-receiver angles have similar shapes, and are thus suitable for stacking to obtain useful, high-quality reference waveforms for the cross-correlations. This assumption is only truly valid in the absence of very sharp velocity contrasts in the subsurface, as such velocity contrasts can give rise to strongly scattered arrivals that interfere with the direct-arriving pulse. Indeed, the BHRS data shown in Figures 5.3 through 5.5 were collected entirely below the water table (located at approximately 3 m depth) and were void of any strongly scattered arrivals. Had the survey region spanned the water table (a very large velocity contrast) or had the antenna positions been nearer to the very reflective air-earth boundary, problems could have been encountered with the picking of some traces; such problems could likely be overcome through a modification of our algorithm, or by filtering the data beforehand to remove the strongly scattered arrivals. For the case where very sharp velocity contrasts in the subsurface are minimal, we have found that the cross-correlation algorithm presented here works extremely well. In addition, with the technique, the effects of moderate scattering are suppressed in the mean traces through the stacking of the common-ray-angle gathers (Pratt and Goulyt, 1991).

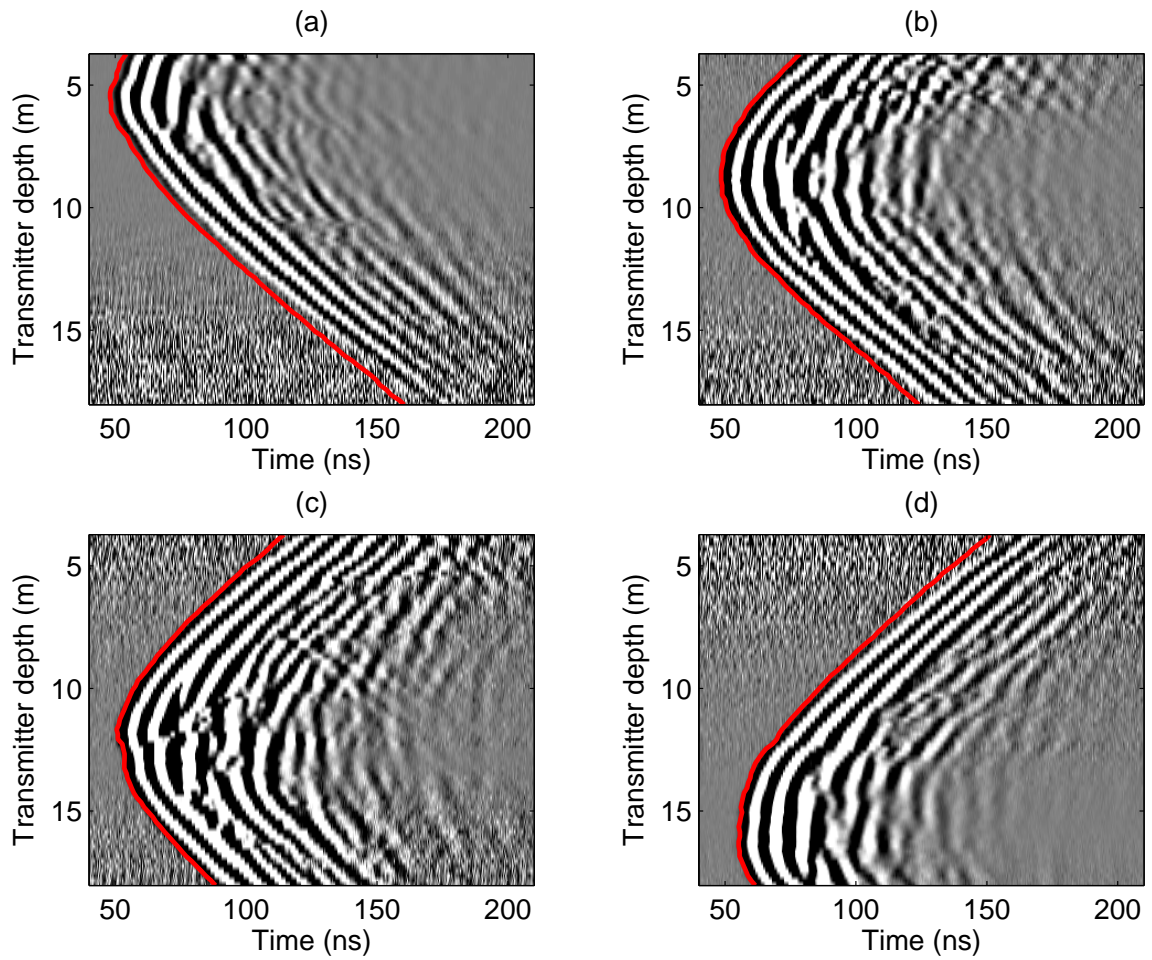


Figure 5.5: Four common-receiver gathers from the BHRS data set showing the results of our automatic picking procedure. Picked first breaks are shown in red. (a) receiver depth = 5.33 m; (b) receiver depth = 8.73 m; (c) receiver depth = 12.33 m; (d) receiver depth = 15.53 m.

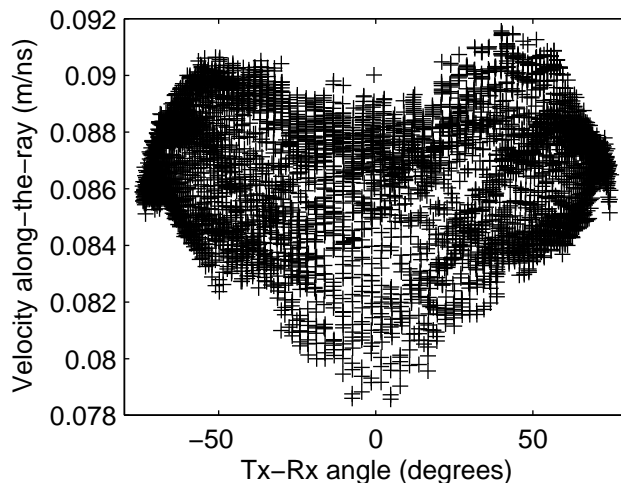


Figure 5.6: Velocity-versus-angle plot for the BHRS field data set.

5.4 Incompatibility of high-angle data

As discussed previously, a second problem that exists when attempting to take advantage of the wide angular coverage afforded by close borehole spacings is that, even when high-angle-ray data can be reliably picked (such as with our cross-correlation technique), they often appear to be incompatible with the lower-angle data available. Significant insight can be gained into this phenomenon through velocity-versus-angle plots, where the average velocity calculated along each ray in a data set (assuming a straight path between the centers of the antennas) is plotted as a function of transmitter-receiver angle. Figure 5.6 shows such a plot for the BHRS data picked in the previous section. Notice the general trend that exists in velocity with angle for these data; the along-the-ray velocities at high transmitter-receiver angles are markedly greater than those determined for lower angles. It is this trend that clearly illustrates why problems are encountered when the high- and low-angle travel times are inverted together; reasonable subsurface velocity models (that do not possess significant amounts of anisotropy) should not give rise to such large-scale trends in

velocity with angle.

We have found that the trend seen in Figure 5.6 is typical of crosshole GPR data collected between closely spaced boreholes (see also Peterson, 2001; Alumbaugh and Chang, 2002). Although Peterson (2001) attributes such a trend to refracted waves that travel partly through air-filled boreholes and arrive before the direct pulse, we also see this trend in data collected between water-filled wells (e.g., the BHRS data shown here). Further, we have not observed such refracted arrivals in finite-difference time-domain (FDTD) simulations of crosshole GPR radiation where the borehole is explicitly included. It is also very difficult to explain the trend shown in Figure 5.6 by the other factors discussed in Peterson's paper that can cause apparent variations in velocity with angle in crosshole GPR data. For example, although errors in the calculation of the transmitter fire time and inaccurate borehole locations could result in a plot resembling Figure 5.6, every step was taken to ensure that these measurements were very accurate for the BHRS data set. More importantly, such errors do not explain the consistency of the trend in Figure 5.6 across different data sets. In addition, although the presence of anisotropy can give rise to general trends in velocity with angle, geologically reasonable anisotropy (i.e., due to thin horizontal layering) results in velocities that are greater at low angles, which is the opposite of what we observe. Finally, it is unlikely that the inversion problems experienced with high-angle data are the simple result of having less-accurate travel-time picks at high angles due to decreased S/N; this again does not explain why we have a general trend in velocity with angle in Figure 5.6.

Recently, Irving and Knight (2005b) addressed the high-angle incompatibility issue in crosshole GPR tomography, and suggested that the problem may result from a common assumption made during the inversion of the data: that first-arriving energy always travels directly between the centers of the antennas. They proposed that, at high transmitter-receiver angles, first-arriving energy may actually travel via the

antenna tips. Figure 5.7 shows a schematic of this situation. In Figure 5.7a, we have the travel paths of energy that are currently assumed by all crosshole GPR inversion strategies. Energy is thought to travel from the center of the transmitter antenna, through the subsurface at some medium velocity v_{med} , to the center of the receiver antenna. Figure 5.7b, on the other hand, shows the path of energy at high angles proposed by Irving and Knight (2005b). Here, first-arriving energy travels between the antenna tips with a velocity along the antenna of v_{ant} . Geometrically, the travel path in Figure 5.7b will be faster than that shown in Figure 5.7a when $v_{ant} > v_{med}$ and the transmitter-receiver angle is beyond some threshold value. Using numerical modeling and considering a number of different borehole diameters and external medium properties, Irving and Knight (2005b) showed that v_{ant} will often be significantly greater than v_{med} , in both air- and water-filled boreholes, for a common commercial GPR antenna design.

Figure 5.8 shows the geometrically calculated trend in velocity with angle that occurs if $v_{ant} > v_{med}$, when it is assumed that all first-arriving energy travels directly between the centers of the antennas. Here, the antennas considered are 0.8-m-long, center-fed dipoles that are separated by a horizontal distance of 4 m. The homogeneous medium velocity is 0.06 m/ns, and the velocity along the antennas is 0.11 m/ns. These two velocities are typical of a saturated zone scenario (Irving and Knight, 2005b). Figure 5.8 shows that, at low angles when the assumption about the travel path of first-arriving energy is valid, there is no error in the calculation of the medium velocity (i.e., the velocity curve is flat and equal to the correct value of 0.06 m/ns). However, above some threshold angle when first arrivals actually represent tip-to-tip antenna coupling, errors result because this assumption is invalid. These errors reach some peak value with angle, and then begin to decrease in magnitude as the length of the travel path increases.

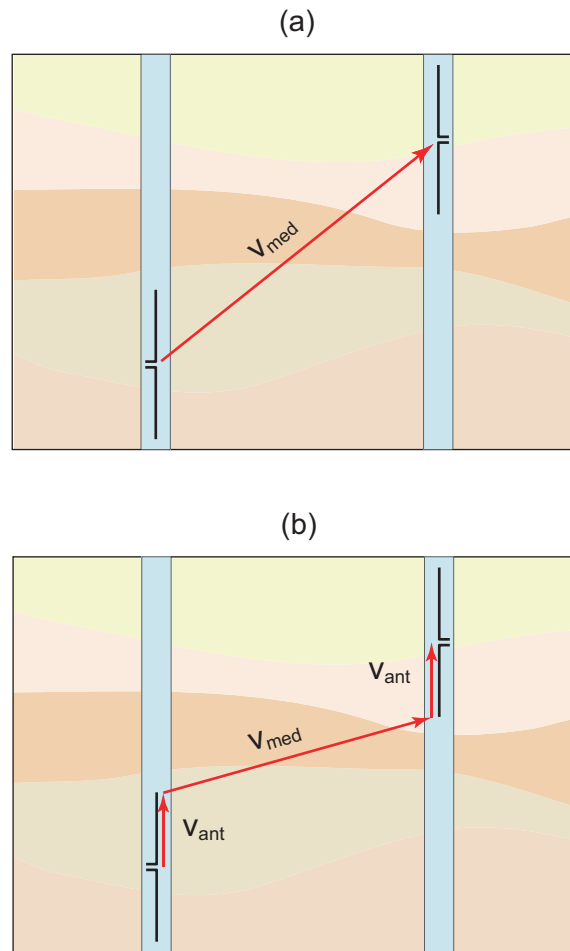


Figure 5.7: (a) Assumed and (b) proposed travel paths of first-arriving energy at high transmitter-receiver angles (Irving and Knight, 2005b).

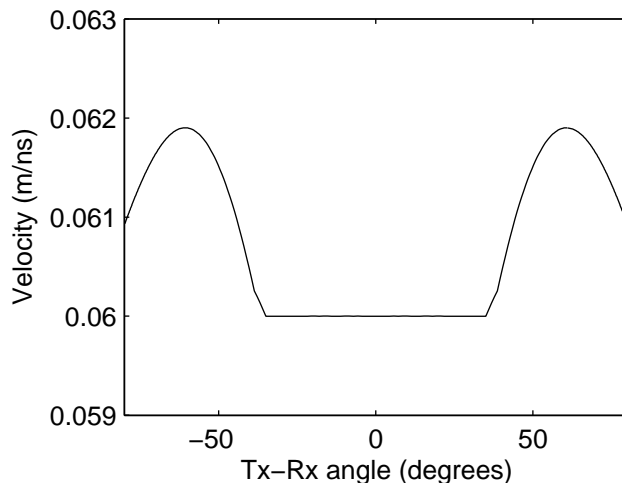


Figure 5.8: Geometrically determined velocity-versus-angle plot for the case where $v_{ant} > v_{med}$. Borehole separation = 4 m, antenna length = 0.8 m, $v_{med} = 0.06$ m/ns, and $v_{ant} = 0.11$ m/ns.

Although velocity-versus-angle plots similar in character to Figure 5.8 were generated by Irving and Knight (2005b) using the antenna modeling approach of Irving and Knight (2006b), we have found that such curves are too simplistic to describe all crosshole GPR behavior. Specifically, the exact trend in velocity with angle seen in Figure 5.8 will occur only when the excitation pulse feeding the transmitter antenna is short in comparison to the length of time required to travel along the antenna arms; this is not likely a realistic scenario in all cases (e.g., Sato and Thierbach, 1991; Ellefsen and Wright, 2005; Liu and Sato, 2005). To illustrate, Figure 5.9 shows two synthetic waveform gathers generated using the technique of Irving and Knight (2006b) for short and long transmitter feed pulses, and the corresponding velocity-versus-angle plots obtained by picking the gathers and assuming center-to-center antenna coupling. All parameters used to create this figure were the same as those used in Figure 5.8, except that a waveform modeling code was employed instead of geometrical ray theory to determine first-arrival times. Constant resistive loading was added along the

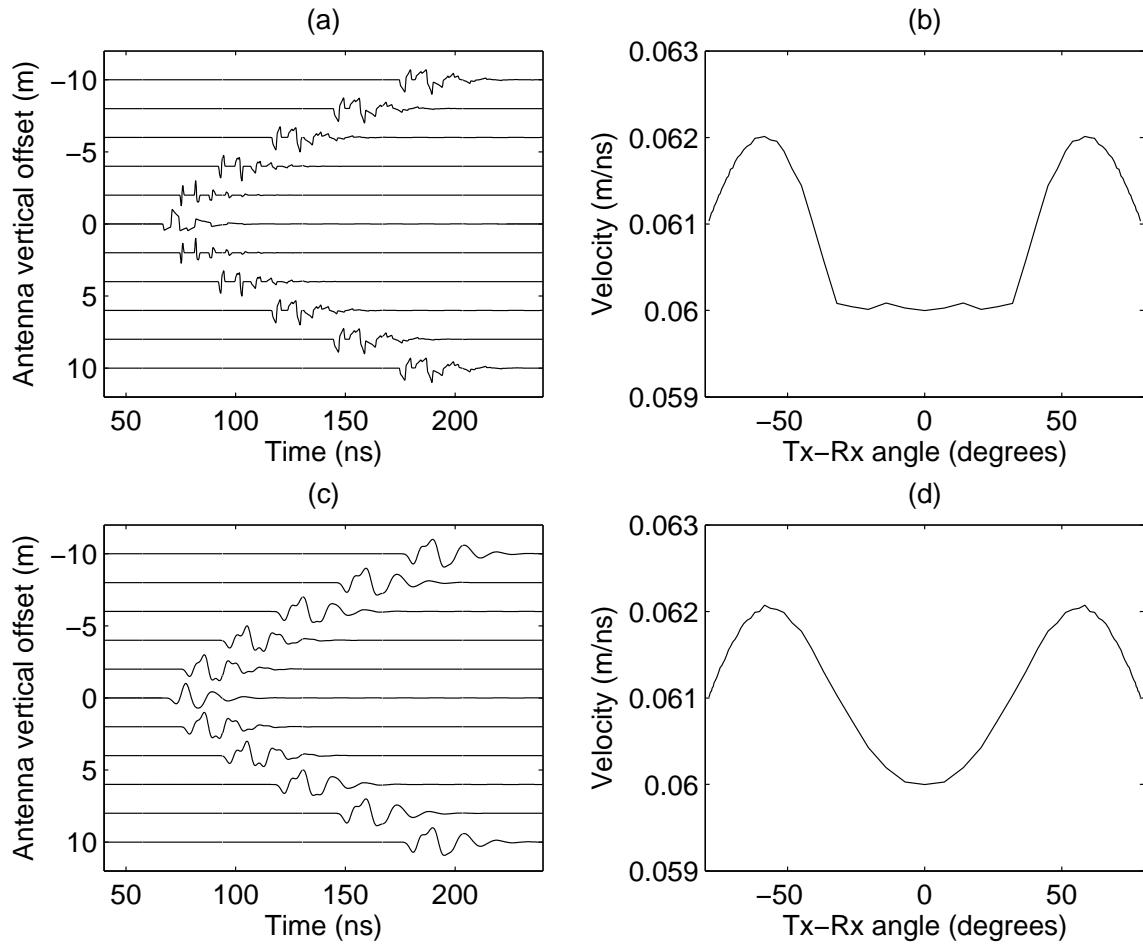


Figure 5.9: Example waveform gathers and velocity-versus-angle plots for the case of short (top) and long (bottom) transmitter feed pulses. Antenna and medium parameters are the same as those used in Figure 5.8.

antennas in the numerical simulations to reduce the width of the emitted pulses and better represent commercial GPR antennas.

Figure 5.9a shows the waveforms produced at various transmitter-receiver offsets using an extremely short (and unrealistic) Gaussian feed pulse having a -20 dB width of approximately 1 ns. Here we see that a number of distinct pulses are visible in the received waveforms, representing radiation and reception at the antenna feed and end points. Because the pulses are well separated in time and do not interfere with one another, we see behavior almost identical to that in Figure 5.8 in the corresponding velocity-versus-angle plot (Figure 5.9b). Figure 5.9c, on the other hand, shows the waveform gather for the more realistic case where the transmitter feed pulse is long compared to the length of time needed to travel along the antenna arms. In this case, a Gaussian pulse having a -20 dB width of approximately 10 ns was used for the simulation. Here, we see that the individual pulses from Figure 5.9a have now merged together. As a result of this interference, the behavior in the corresponding velocity-versus-angle plot (Figure 5.9d) also changes; there is now variation in the calculated velocity across the entire angle range because the arrival time of the first pulse is effectively altered by the presence of subsequent pulses. The behavior shown in Figure 5.9d is clearly very similar to the trend shown for the BHRS data set.

It is important to note that the above results, and those of Irving and Knight (2005b), are based on the fundamental assumption that commercial crosshole GPR antennas radiate (and receive) significant pulses of energy at both the antenna feed and end points. That is, although we acknowledge that commercial GPR antennas are resistively loaded to produce a compact, broadband waveform, we assume that this loading is such that the input feed pulse (radiated first at the center of the antenna) is still able to reach the antenna tips and be radiated there as well. We base this assumption upon the following observations: First, although they are compact, the waveforms produced by crosshole GPR antennas contain a number of peaks and

troughs that could not be produced if the antennas were loaded in a manner so as to be reflectionless. As shown by Irving and Knight (2006b), resistive loading of a dipole antenna using a true Wu-King reflectionless profile (Wu and King, 1964) results in received waveforms with significantly less ringing than the crosshole GPR pulses that we record in the field. Secondly, it is well known that true Wu-King resistive loading of antennas significantly decreases their radiation efficiency (Lampe and Holliger, 2005). As a result, resistive loading in commercial antennas tends to be less severe than this, such that there is an adequate compromise between pulse width and power transfer into the ground (A.P. Annan, personal communication, 2005).

Another factor that may affect measured velocities as a function of angle in crosshole GPR tomography is dispersion. GPR pulses are well known to undergo significant frequency dispersion when traveling through the subsurface (Turner and Siggins, 1994; Baño, 1996; Irving and Knight, 2003). This broadening of the pulses during propagation results from frequency-dependent electrical properties and scattering. It also occurs when the combination of GPR frequency and earth conductivity is such that the radar operates near the boundary between the wave propagation and diffusion regimes (Annan, 1996; Cai et al., 1996). Figure 5.10 illustrates the effect of dispersion on velocities measured from crosshole GPR data. For this figure, we took the synthetic gather shown in Figure 5.9c and introduced constant $Q = 15$ dispersion into each trace. This Q value falls in the middle of the range suggested for GPR by Turner and Siggins (1994) of 2 to 30. The non-dispersed waveforms and velocity-versus-angle plot are shown in red in Figures 5.10a and 5.10b, respectively, whereas the results for the dispersed gathers are shown in black. All traces have been normalized by their maximum values for easier comparison. Notice that, because of the broadening of the GPR pulse due to dispersion, the picked first breaks are delayed more at high angles (i.e., longer travel paths) which causes a relatively sharp pull-down on the velocity-versus-angle plot. Given that the representative waveforms

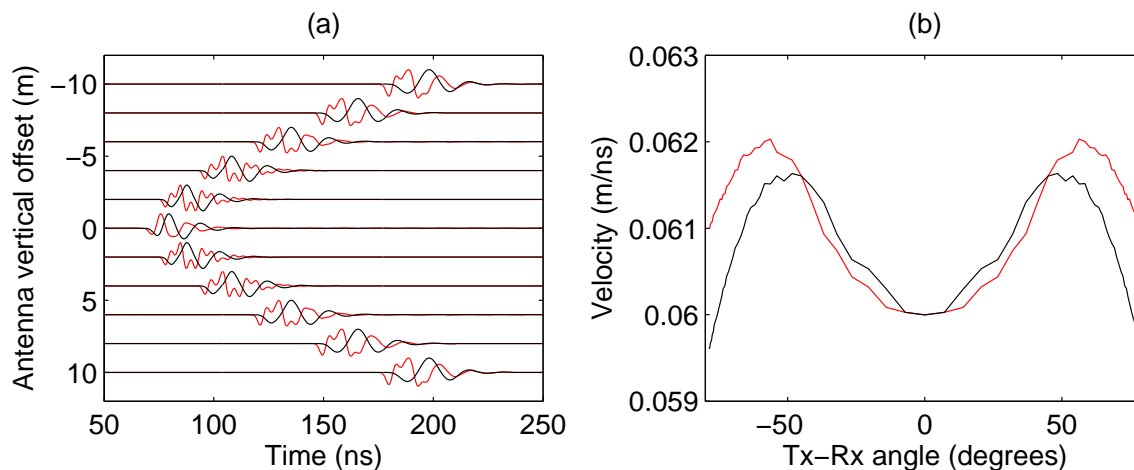


Figure 5.10: Example waveform gathers and velocity-versus-angle plots comparing the non-dispersive case from Figure 5.9 (in red) with the case of constant $Q = 15$ dispersion (in black).

for the BHRS data in Figure 5.4 appear to be more dispersed at high angles, this phenomenon may be the cause of the relatively sudden decrease in velocity beyond 60 degrees that can be seen in Figure 5.6.

5.5 Improved inversion procedure

We outlined in the previous section a number of factors that we believe contribute to the incompatibilities experienced with high-angle ray data in crosshole GPR tomography. All of these factors together result in errors in measured velocities that vary as a function of transmitter-receiver angle; these errors are most significant at close borehole spacings because small errors in travel time have a greater impact on velocities for shorter path lengths. Understanding the nature and causes of the high-angle incompatibility problem now allows us to formulate an inversion methodology for crosshole GPR that can make use of all available data.

Initially, our approach to this problem involved attempting, through numerical

modeling, to accurately estimate the errors associated with all of the factors that we have discussed, such that crosshole GPR travel-times and ray geometries could be adjusted to remove these errors before inverting. Although we found this approach to work very well with synthetic data where the effects of all factors can be easily quantified (i.e., Irving and Knight (2005a)), we have determined that it requires too much knowledge about specific GPR system and antenna details, along with borehole and external medium properties, to be a useful approach for field data. Indeed, all of our attempts to estimate these sources of error for the BHRS data in Figure 5.6 met with little success. As a result, the approach that we have decided upon to invert all available data in crosshole GPR tomography is much simpler. Because we believe the high-angle incompatibility problem to result from a number of factors that together result in an apparent (but incorrect) trend in velocity with transmitter-receiver angle, we set up our inversion to estimate, in addition to subsurface velocities, parameters that describe a travel-time ‘correction curve’ as a function of angle. In other words, we allow the inversion to determine a small number of parameters that should largely correct for the angle-related errors in the data.

Standard ray-based travel-time tomography is based upon the following equation linking perturbations in travel time to slowness (inverse of velocity) changes in the subsurface:

$$\Delta \mathbf{t} = \mathbf{L} \Delta \mathbf{s}, \quad (5.1)$$

where $\Delta \mathbf{t}$ is a vector containing the difference between observed travel times and those obtained by ray-tracing through a reference slowness model, $\Delta \mathbf{s}$ is a vector containing the slowness perturbations that must be added to the reference model to fit the observed travel-time data, and \mathbf{L} is the ray-based tomographic sensitivity matrix whose rows contain the length of each ray in every model cell, assuming center-to-center antenna coupling. In our modified inversion procedure, we simply augment

equation (5.1) in the following manner:

$$\Delta \mathbf{t} = \begin{bmatrix} \mathbf{L} & \mathbf{A} \end{bmatrix} \begin{bmatrix} \Delta \mathbf{s} \\ \Delta \mathbf{p}_a \end{bmatrix}, \quad (5.2)$$

where the parameters contained in vector $\Delta \mathbf{p}_a$ are the values of the travel-time correction curve at a set of reference angles, and the rows of matrix \mathbf{A} contain linear interpolation weights to obtain, from these parameters, the travel-time correction for each ray. In using equation (5.2) for tomography, we implicitly assume that measured travel times, once they have been suitably corrected as a function of angle, satisfy equation (5.1).

To solve equation (5.2) for $\Delta \mathbf{s}$, we form the least-squares normal equations and solve the resulting system using the conjugate-gradient method (e.g., Scales, 1987; Squires et al., 1992). We explicitly impose regularization on the slowness model in this system using second-derivative (smoothness) constraints in the x - and z -directions. If desired, smoothness or symmetry constraints could also be imposed on the travel-time correction curve, although we have generally found such constraints to be unnecessary if the number of parameters describing the curve is kept small. The only constraint on $\Delta \mathbf{p}_a$ that we have found to be absolutely necessary in crosshole GPR inversions is the enforcement of a zero travel-time correction for horizontal (zero-angle) rays. This is because, without such a constraint, velocities in the model could be adjusted by some constant value and the offset compensated by an angle-dependent travel-time correction. In forming this constraint, we make the assumption that low-angle travel times in the data are accurate. Generally, this should be the case because our travel-time data are calibrated in the field using waveforms that are recorded when the antennas are parallel and separated in air by some known amount.

As we will see in the next section, the modified inversion strategy described by equation (5.2) allows us to successfully invert high- and low-angle crosshole GPR data

together to obtain tomograms with improved horizontal resolution. This is despite the fact that, in using this strategy, only travel times are adjusted as a function of angle and we thus neglect any errors in source and receiver locations caused by tip-to-tip antenna coupling. One important limitation to applying angle corrections in this manner is that the technique is not suitable for the inversion of data collected in strongly anisotropic environments. In such environments, large-scale velocity variations as a function of angle are not errors, and an anisotropic inversion code would be necessary to obtain a proper subsurface image. In our experience, however, strong EM-wave velocity anisotropy in unconsolidated sediments is uncommon. This observation is supported by Peterson (2001).

5.6 Examples

5.6.1 Synthetic data

We now show the results of applying our modified inversion strategy to synthetic crosshole GPR data generated using the antenna modeling approach of Irving and Knight (2006b). Figure 5.11a shows the velocity model that we constructed for this example. The model consists of a number of blocks of various sizes having dielectric constants of $\kappa = 22$ (red, 0.064 m/ns) and $\kappa = 28$ (blue, 0.057 m/ns) embedded in a homogeneous background medium having $\kappa = 25$ (green, $v=0.06$ m/ns). Electrical conductivity throughout the model was set to a constant value of 1 mS/m, and magnetic permeability was assumed to equal its value in free space, μ_0 . These electrical properties were chosen to represent a saturated zone scenario. Although the model in Figure 5.11a is clearly not geologically realistic, its blocky structure allows us to effectively examine the differences in resolution attainable using different inversion strategies.

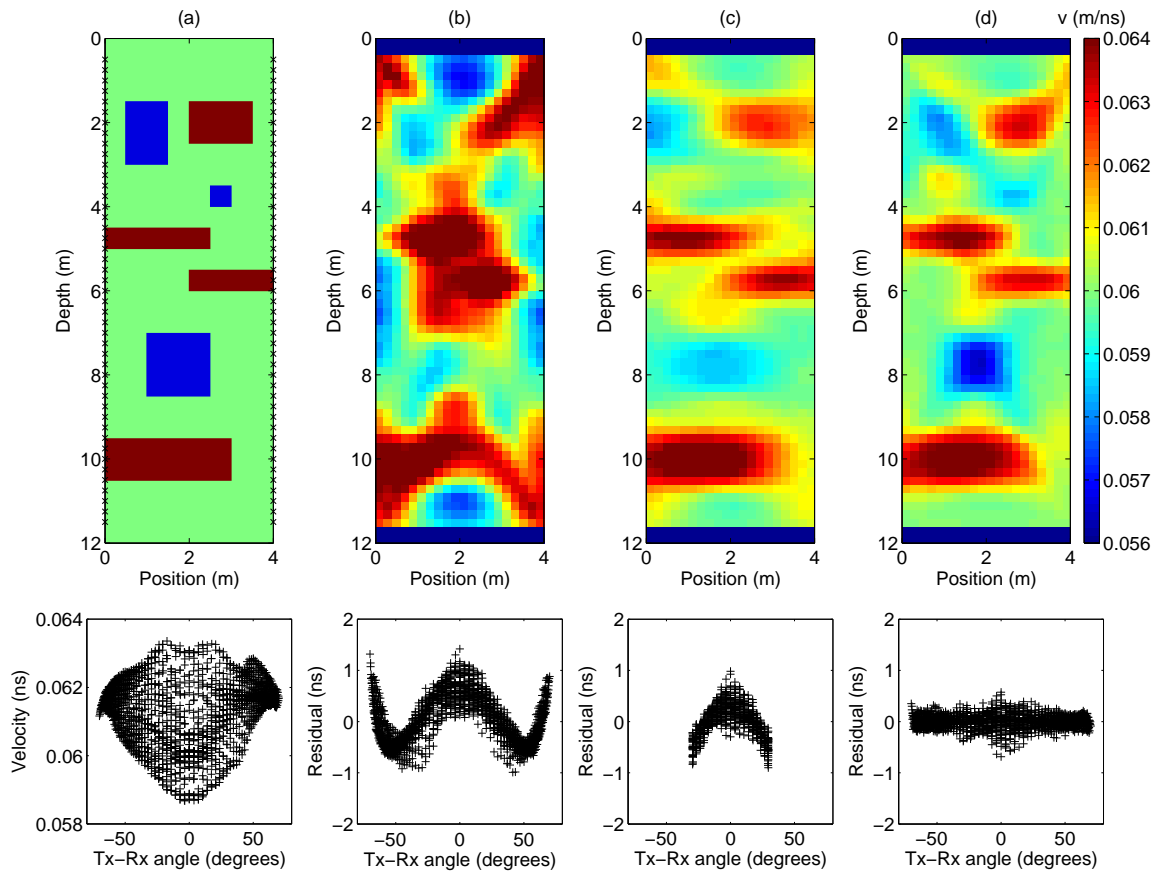


Figure 5.11: Synthetic data results. (a) Input velocity model and velocity-versus angle plot for the synthetic data. Transmitter and receiver locations are marked with an 'x'; (b) Result of applying the standard crosshole GPR inversion strategy to all available data; (c) Result of applying the same standard inversion strategy to an aperture-limited (< 30 degree) subset of the data; (d) Result of allowing an angle-dependent travel-time correction in the inversion of all available data. Dark blue areas represent regions with no ray coverage.

To create the synthetic data, we simulated crosshole GPR transmission and reception through the model in Figure 5.11a. The boreholes, located along the left and right sides of the model, were spaced 4 m apart and the transmitter and receiver antennas were located every 0.25 m from 0.5 to 11.5 m depth. Realistic antenna behavior was accounted for in the simulations by replicating, using a superposition of point-electric-dipole source and receiver responses, the antenna current distribution obtained from a finely discretized FDTD simulation (Irving and Knight, 2006b). The borehole in the detailed simulation was modeled as a 4-inch-diameter, water-filled cylinder. The antenna model that we considered is a 0.8-m-long, insulated, center-fed dipole, and is described in detail by Irving and Knight (2006b). Constant resistive loading was included along the antenna elements such that the waveforms that were produced approximately resembled those that we have recorded in field surveys with a similar antenna. The approximate velocity of energy along the model antenna, when located in the water-filled borehole, was 0.11 m/ns. To feed the transmitter antenna, we used a short Gaussian pulse having a -20 dB width of approximately 10 ns.

Once the FDTD simulations were complete, the synthetic crosshole gathers were automatically picked (a trivial procedure in the case of noise-free data) and the first breaks were calibrated so that the travel times for horizontal ray paths were accurate. At the bottom of Figure 5.11a, the velocity-versus-angle plot for the resulting data set is shown. Because there are travel-time data for angles up to 70 degrees from the horizontal, we should, in theory, be able to perform very high-resolution tomographic imaging of the inter-borehole region. However, like the plot for the BHRS data in Figure 5.6, there appears to be a general trend in this figure towards greater velocities at high angles. This trend, again, is the result of assuming that first-arriving energy always travels directly between the antenna centers, when in fact we have tip-to-tip coupling at high angles, and also the effects of interference between feed- and end-radiated pulses. Note that dispersion was not considered in this synthetic example.

Figure 5.11b shows the tomogram and residuals that were obtained when all of the available travel-time data (for high- and low-angle rays) were incorporated into a standard crosshole GPR tomographic inversion (i.e., based on equation (5.1)). For this and each inversion result to follow, regularization parameters were kept constant so that differences in the tomograms would truly reflect differences between the inversion strategies used. Also, because velocity contrasts in the synthetic model are less than 15% and the travel paths are relatively short, straight rays were assumed in the inversions; this assumption has no impact on the generality of our findings, but significantly simplifies the tomographic imaging. The tomogram in Figure 5.11b is clearly dominated by numerical artifacts as a result of the incorrect assumption about the travel path of first-arriving energy. In fact, the artifacts are so strong in this case that they completely obscure any reliable subsurface information. In the travel-time residuals plot, the problem appears as a ‘W’-shaped trend with angle. It is this angular dependence that we address in our modified inversion strategy to allow for the successful incorporation of all available data.

The usual means of dealing with the high-angle incompatibility problem in cross-hole GPR tomography is to simply exclude high-angle data from inversions. Figure 5.11c shows the tomogram and residuals obtained by inverting an aperture-limited (< 30 degree) subset of the synthetic data set. Once again, the standard crosshole GPR inversion strategy was employed. Here, a reasonable representation of the input velocity model is clearly obtained. However, because we have not incorporated high-angle rays into the inversion, horizontal resolution is significantly compromised. Most noticeably, the high- and low-velocity anomalies around 2 m depth in Figure 5.11a are not separated from the edges of the grid in Figure 5.11c, the small, low-velocity anomaly around 4 m depth cannot be identified, and the large, low-velocity anomaly around 8 m depth is significantly smeared in the horizontal direction. Although more horizontal structure could be added to this tomogram by increasing the cutoff angle

for aperture limitation, we found that 30 degrees yielded the best trade-off between an image containing horizontal structure and one with a minimal number of inversion artifacts. Significant angular dependence is also seen in the travel-time residuals in Figure 5.11c.

In Figure 5.11d, we see the results of applying our modified inversion procedure to all available travel times in the synthetic data set. As mentioned, this involves estimating, in addition to subsurface velocities, a set of parameters describing a travel-time correction curve as a function of angle. Notice that, in this case, we obtain a significantly improved result over aperture limitation. All anomalies in the input velocity model can now be seen, and there is far less horizontal smearing present in the tomogram. In addition, the amplitudes of the anomalies in Figure 5.11d are closer to the true block velocities in Figure 5.11a. Clearly, by allowing for an angle-dependent travel-time correction in the inversion, we are able to effectively use the high-angle data to improve tomographic resolution. Further, because of the parameterization with angle, there is no longer an angular trend seen in the travel-time residuals in Figure 5.11d, and the absolute magnitude of these residuals is significantly less than in Figure 5.11b. This is not surprising, but it does show that, after the travel-time correction, our synthetic data are much better fit by the model described by equation (5.1). Finally, Figure 5.12 shows the angle correction parameters that were obtained with our modified inversion strategy. In this example, we inverted for 30 parameters that were evenly spaced over the angle range of the data, from -70 to 70 degrees. Although no regularization (aside from enforcing a zero travel-time correction at zero angle) was imposed on these parameters, we see that the travel-time correction curve is smooth and reasonable.

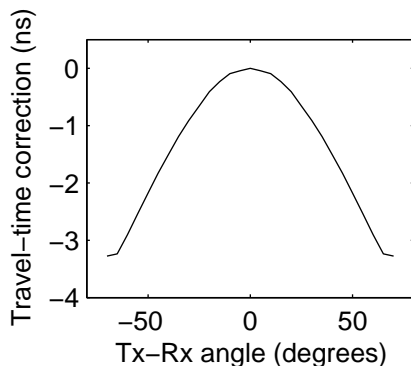


Figure 5.12: Angle-dependent travel-time correction parameters obtained in the inversion of the synthetic data in Figure 5.11d.

5.6.2 BHRS field data

As a field-data example, we now show the application of our modified inversion strategy to the 250-MHz BHRS data set considered earlier and picked using cross-correlations. As mentioned, all steps were taken with these data to determine as accurately as possible the transmitter fire time and borehole positions in the subsurface. In addition, for the tomography, we applied a slight coordinate rotation to the data to minimize borehole deviations in the out-of-plane dimension; after this coordinate adjustment, all transmitter and receiver locations were contained within 3 cm of the tomographic plane. As with the synthetic example, straight rays were used in all of the inversion results to follow because velocity contrasts in the subsurface were believed to be less than 20%. Also, regularization parameters were again kept constant between inversions so that the relative effectiveness of the different inversion strategies could be evaluated.

Figure 5.13a shows the tomogram and travel-time residuals obtained when all of the available BHRS data (for ray angles up to 75 degrees from the horizontal) were inverted using the standard crosshole GPR inversion approach. Although numerical artifacts in this image are clearly not as severe as in Figure 5.11b (likely a result of

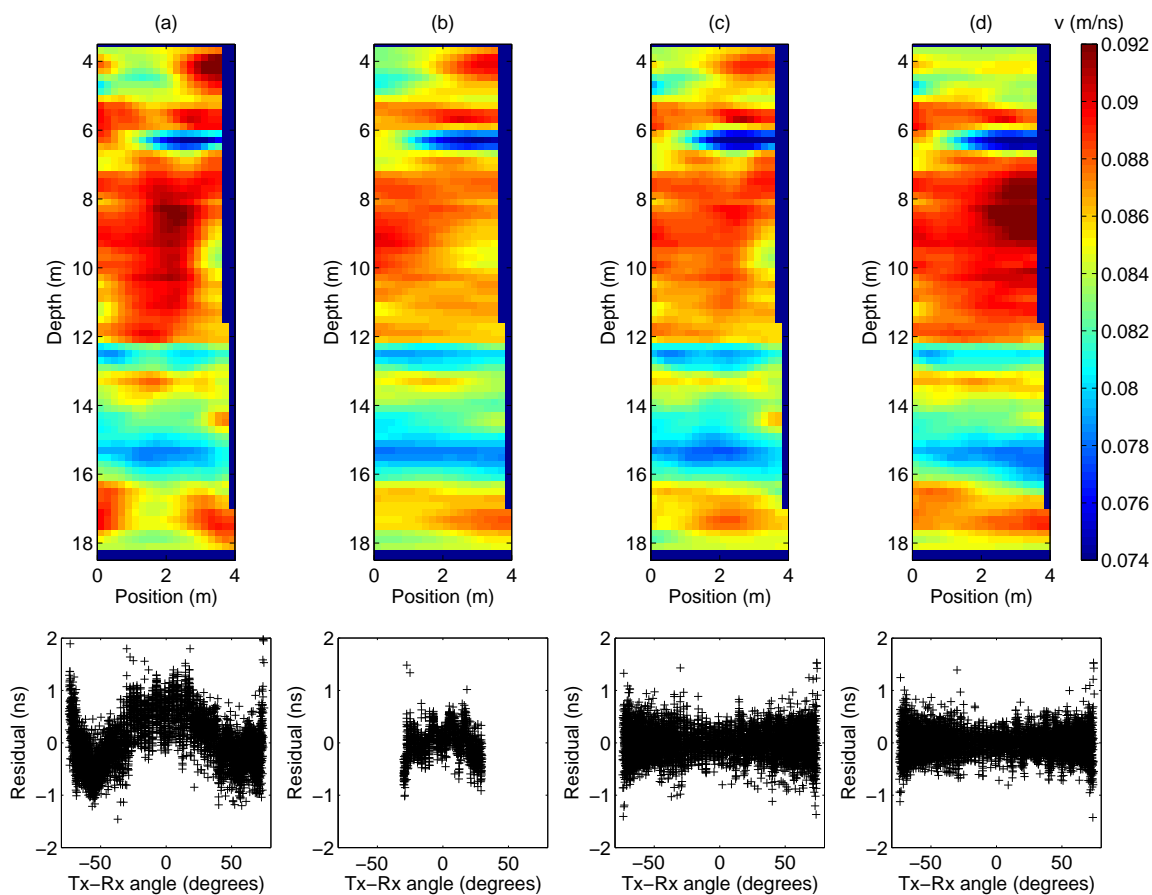


Figure 5.13: Application to the BHRS field data set. (a) Result of applying the standard crosshole GPR inversion strategy to all available data; (b) Result of applying the same standard inversion strategy to an aperture-limited (< 30 degree) subset of the data; (c) Result of allowing an angle-dependent travel-time correction in the inversion of all available data; (d) Result of allowing both angle- and receiver-position-dependent travel-time corrections in the inversion of all available data. Dark blue areas represent regions with no ray coverage.

the fact that shorter, higher-frequency antennas were used for this survey), we see a number of features in Figure 5.13a that are geologically unreasonable, and indicate problems with the inversion. Specifically, in a number of places in the image, there are horizontal discontinuities where it appears that continuity should exist. Most notable of these are the high-velocity layer between 16 and 18 m (which fades out in the center of the tomogram), and the thick, high-velocity zone between 7 and 12 m (which contains a central zone of significantly higher velocity). As with the synthetic example, these problems appear in the plot of travel-time residuals as a distinct, ‘W’-shaped trend with angle.

In Figure 5.13b, we see the result of applying aperture-limitation to the BHRS data set. Again, a cutoff angle of 30 degrees was used to obtain the best trade-off between horizontal resolution and a minimal number of obvious inversion artifacts. In this case, we see that the tomogram has become much more geologically reasonable. Layers are now more horizontally continuous and the image lacks the obvious problems seen in Figure 5.13a. However, because we discarded the high-angle ray data to produce this inversion result, we are left wondering whether such horizontal continuity is real, or simply a product of the aperture limitation.

Figure 5.13c shows the tomogram and residuals obtained when all available BHRS travel times were incorporated into our modified inversion procedure. Notice that we are now able to obtain a very reasonable subsurface image that is quite similar in appearance to the aperture-limited result in Figure 5.13b. For this example, it seems that the addition of the high-angle data does not provide much additional structure to the tomogram (i.e., the geology between the boreholes is such that it can be largely captured by the low-angle-ray data). However, because we have used all available travel times to create the image in Figure 5.13c, we have greater confidence that the features seen here are representative of the true subsurface. Again, the travel-time residuals obtained using our modified inversion procedure are approximately flat with

angle.

Although we consider Figure 5.13c to be a much improved subsurface image over Figure 5.13a, there are still a number of features in this tomogram that cause concern given geological knowledge at the BHRS (a very well characterized site). Specifically, the thick, high-velocity zone between 7 and 12 m depth, which is known to be a poorly sorted sediment layer, shows significant lateral variability in Figure 5.13c, when it is well known that this layer is relatively homogeneous and continuous across the BHRS. Also, the lateral change from low to high velocity in the upper 2 m of the tomogram is not supported by other site data. As a result, we investigated adding a further parameterization to the inverse problem to account for possible static travel-time shifts at the receiver locations.

When collecting each gather in the BHRS data set, the receiver antenna was kept fixed while the transmitter antenna was moved down its borehole. Because of this, the potential exists for many travel times to be affected by a single error in the location of the receiver antenna in its well, or by differences in coupling of this antenna with its surroundings. For example, a movement of the receiver antenna in its well by only 1 inch will result in a shift in measured travel time of approximately 1 ns, which is significant when the borehole spacing of 3.5 m is considered. In addition, possible drift in the transmitter fire time over the crosshole survey can result in time shifts that will affect all traces in a receiver gather.

To estimate travel-time shifts at each receiver location in addition to velocities and angle-correction parameters, we further augmented equation (5.2) as follows:

$$\Delta \mathbf{t} = \begin{bmatrix} \mathbf{L} & \mathbf{A} & \mathbf{R} \end{bmatrix} \begin{bmatrix} \Delta \mathbf{s} \\ \Delta \mathbf{p}_a \\ \Delta \mathbf{p}_r \end{bmatrix} \quad (5.3)$$

where the vector $\Delta\mathbf{p}_r$ contains the receiver position travel-time corrections, and matrix \mathbf{R} selects, for each ray, which correction to use. Inverting for statics in this manner was shown by Vasco et al. (1997) to be a valuable tool in crosshole GPR tomography. Because there is no reason why such static travel-time shifts should be smooth in depth, we add no smoothness regularization to the inversion.

Figure 5.13d shows the tomogram and residuals for the complete BHRS data set, after both receiver-position- and angle-dependent travel-time corrections were estimated in addition to subsurface velocities. We now see that the thick, high-velocity zone between 7 and 12 m depth is more uniform and horizontally continuous, and that the lateral velocity change in the upper 2 m of the section has disappeared. In addition, the thin, high-velocity layer at approximately 13 m depth is more pronounced than in Figure 5.13c, and the dipping interface between the low- and high-velocity layers near the bottom of the section can be seen more clearly. In our opinion, the results in Figure 5.13d appear to be more geologically reasonable than those shown in Figure 5.13c, and they are more consistent with the other data from the BHRS. Figure 5.14 shows the angle- and receiver-position-dependent travel-time corrections that were estimated by the inversion procedure. In the plot of the receiver static corrections versus depth (Figure 5.14b), we see a general trend that may result from a drift in the transmitter fire time over the period of the crosshole survey, inaccuracies in the borehole deviation measurements, or possibly stretching of the receiver cable from repeated use. The cause of this trend is currently under further investigation.

5.7 Conclusions

We have presented two strategies for improving the resolution of crosshole GPR tomography at close borehole spacings. Together, these strategies allow us to take full advantage of the excellent angular coverage that such borehole spacings can provide.

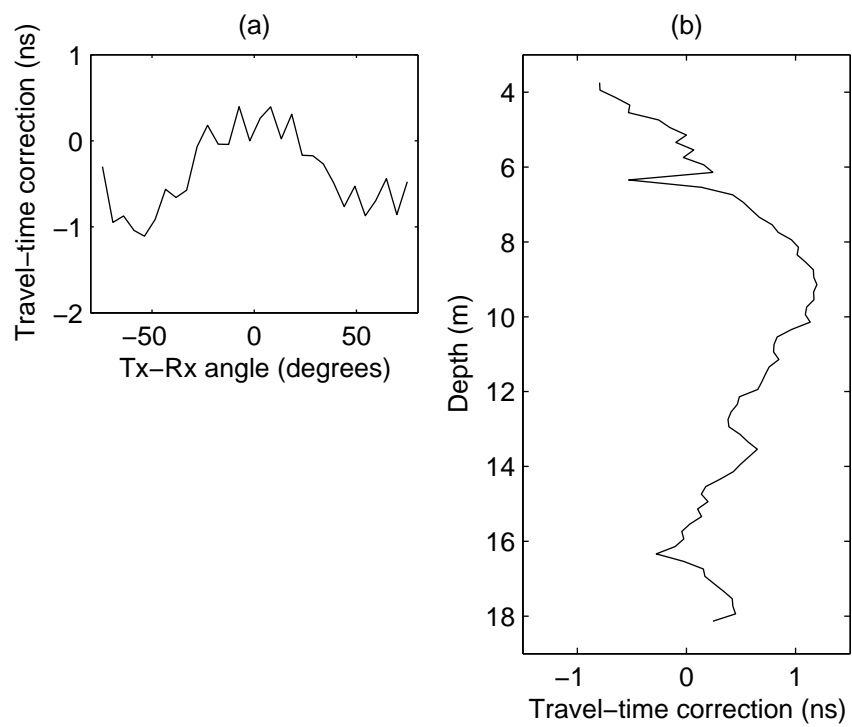


Figure 5.14: (a) Angle- and (b) receiver-position-dependent travel-time corrections obtained in the inversion of the BHRS data in Figure 5.13d.

For picking first breaks on very noisy traces at high angles, we have shown that a cross-correlation approach using angle-dependent reference waveforms can be very effective. An important application of this picking method, not considered here, may be time-lapse crosshole GPR surveying, where S/N is commonly very low because stacking of each trace is minimized. As mentioned previously, our picking method performs best when strong scattering in the data (interfering with the direct arrivals) is not present. Future work includes investigating whether such an approach could be modified for effective use on data containing strongly scattered events.

To incorporate high-angle data into crosshole tomographic inversions, we have shown that inverting for a small number of parameters that describe an angle-dependent travel-time correction curve, in addition to subsurface velocities, can be very effective. The reason for this is that the factors causing the problems with high-angle data result in errors in measured velocities that vary as a function of transmitter-receiver angle. These errors are most significant when borehole spacings are small. We note again that our modified inversion procedure provided improved results with both synthetic and field data, despite the fact only travel times were altered, and changes in survey geometry due to tip-to-tip coupling were thus ignored. If desired, the tomographic sensitivity matrix in equations (5.1) through (5.3) could also be adjusted to account for end-to-end coupling above a certain threshold angle. This may be a necessary step with lower-frequency (i.e., longer antennas) data.

Finally, we must stress that angular coverage is one of many factors that affect resolution in crosshole GPR tomography. By allowing for improved angular coverage with the methods presented here, we have seen that significant increases in tomographic resolution are possible. However, resolution with ray-based tomography can only be improved to a certain point, as ray-based techniques have an upper resolution limit of approximately the first Fresnel zone associated with the GPR pulse bandwidth (Williamson and Worthington, 1993). In order to improve resolution past this

limit, full-waveform inversion methods must be employed. This is another topic of future research.

Chapter 6

Directions for future research

A number of possible avenues for future research have opened as a result of the work presented in this thesis. First and foremost, the crosshole GPR waveform modeling code presented in Chapter 3 now allows us to fully investigate how radar system, antenna, and borehole details affect the measurements that we make with crosshole GPR, and the subsurface parameters that are estimated from these measurements. One topic that falls into this category, of course, is the work presented in Chapters 4 and 5, where the effects of the antenna length, borehole diameter, borehole filling material, and transmitter feed pulse on crosshole GPR travel-time tomography were investigated, and an inversion strategy was tailored to fit these findings. However, many other questions remain to be answered. Perhaps the most interesting of these involves the effects of the same parameters on crosshole GPR attenuation tomography. Whereas travel-time tomography can yield estimates of subsurface water content, crosshole GPR attenuation tomography offers the prospect of providing another very useful parameter to hydrogeologists: electrical conductivity, which is often very dependent upon clay content in the subsurface, and thus possibly hydraulic conductivity.

Recently, Holliger and Bergmann (2002) questioned the robustness of crosshole

GPR attenuation tomography because they found, through basic FDTD modeling using an infinitesimal dipole source, that guided waves in water-filled boreholes can significantly alter crosshole GPR radiation patterns from the patterns that are usually assumed for the tomography (those of a half-wave dipole antenna in a homogeneous medium). However, preliminary work that I have done with the antenna modeling code presented in Chapter 3 suggests that such effects may only play an important role when the voltage pulse fed into the transmitter antenna is very short. That is, if the transmitter feed pulse is of low-enough frequency, guided waves may have a minimal effect on the radiation patterns of the antennas. Consequently, further research should investigate what types of feed pulses are typical of commercial crosshole GPR systems, and if borehole guided modes are excited by these pulses, whether attenuation tomography could be made more robust through low-pass filtering the data before analysis.

Another logical research direction that follows from the work presented in Chapter 3 of this thesis is the full-waveform inversion of crosshole GPR data. With ray-based tomography, resolution cannot exceed a limit approximately equal to the Fresnel zone associated with the propagating pulse bandwidth, because scattering from subsurface heterogeneities is neglected (Williamson and Worthington, 1993). This resolution limitation can be overcome with full-waveform inversion techniques (which account for all forms of scattering in the data), but this comes at the cost of (i) severe non-linearity of the problem and thus great sensitivity to the starting model, and (ii) great computational expense because a full numerical simulation must be performed for each iteration. One finding in this thesis that has important implications for full-waveform inversion is the sensitivity of crosshole GPR waveforms to antenna design, radar system details (such as the form of the transmitter feed pulse), and borehole properties. In order to forward model waveforms that are similar to those obtained in the field, we must be able to obtain all of these parameters very accurately.

Finally, a topic of research that was planned for this thesis, but was eventually left out after the realization that it could fill an entire thesis on its own, is the joint inversion of crosshole and surface-based GPR data for tomography. As mentioned, at close borehole spacings, it is possible to obtain excellent angular coverage of the subsurface with crosshole GPR tomography. However, when the boreholes are further apart, we have a strong bias towards horizontal raypaths, and we thus lack the vertical rays necessary to constrain lateral subsurface variability. Similarly, when using multi-offset surface-based reflection data for tomography, there is a strong bias towards vertical raypaths, and we lack the horizontal rays necessary to properly constrain variability in the vertical direction. Through jointly inverting these two types of data for tomography, it may be possible to significantly improve tomographic resolution.

References

- Alumbaugh, D., and Chang, P.Y., 2002, Estimating moisture contents in the vadose zone using cross-borehole ground-penetrating radar: A study of accuracy and repeatability: *Water Resources Research*, **38**, 1309, doi:10.1029/2001WR000754.
- Annan, A.P., 1996, Transmission dispersion and GPR: *Journal of Environmental and Engineering Geophysics*, **0**, 125–136.
- Arcone, S.A., 1995, Numerical studies of the radiation patterns of resistively loaded dipoles: *Journal of Applied Geophysics*, **33**, 39–52.
- Asprion, U., and Aigner, T., 1999, Towards realistic aquifer models: Three-dimensional georadar surveys of Quaternary gravel deltas (Singen basin, SW Germany): *Sedimentary Geology*, **129**, 281–297.
- Baño, M., 1996, Constant dielectric losses of ground-penetrating radar waves: *Geophysical Journal International*, **124**, 279–288.
- Balanis, C.A., 1997, *Antenna Theory: Analysis and Design*: Harper & Row.
- Berenger, J.P., 1994, A perfectly matched layer for the absorption of electromagnetic waves: *Journal of Computational Physics*, **114**, 185–200.
- Beres, M., Huggenberger, P., Green, A.G., and Horstmeyer, H., 1999, Using two-

and three-dimensional georadar methods to characterize glaciofluvial architecture: *Sedimentary Geology*, **129**, 1–24.

Bergmann, T., Robertsson, J.O.A., and Holliger, K., 1996, Numerical properties of staggered finite-difference solutions of Maxwell's equations for ground-penetrating radar modeling: *Geophysical Research Letters*, **23**, 45–48.

Bergmann, T., Robertsson, J.O.A., and Holliger, K., 1998, Finite-difference modeling of electromagnetic wave propagation in dispersive and attenuating media: *Geophysics*, **63**, 856–867.

Bergmann, T., Blanch, J.O., Robertsson, J.O.A., and Holliger, K., 1999, A simplified Lax-Wendroff correction for staggered-grid FDTD modeling of electromagnetic wave propagation in frequency-dependent media: *Geophysics*, **64**, 1369–1377.

Bourgeois, J.M., and Smith, G.S., 1996, A fully three-dimensional simulation of a ground-penetrating radar: FDTD theory compared with experiment: *IEEE Transactions on Geoscience and Remote Sensing*, **34**, 36–44.

Buechler, D.N., Roper, D.H., Durney, C.H., and Christensen, D.A., 1995, Modeling sources in the FDTD formulation and their use in quantifying source and boundary condition errors: *IEEE Transactions on Microwave Theory and Techniques*, **43**, 810–814.

Cai, J., and McMechan, G.A., 1995, Ray-based synthesis of bistatic ground-penetrating radar profiles: *Geophysics*, **60**, 87–96.

Cai, W., Qin, F., and Schuster, G.T., 1996, Electromagnetic velocity inversion using 2-D Maxwell's equations: *Geophysics*, **61**, 1007–1021.

Carcione, J.M., 1996, Ground-penetrating radar: Wave theory and numerical simulation in lossy anisotropic media: *Geophysics*, **61**, 1664–1677.

- Casper, D.A., and Kung, K.S., 1996, Simulation of ground-penetrating radar waves in a 2-D soil model: *Geophysics*, **61**, 1034–1049.
- Chen, Y.H., Chew, W.C., and Oristaglio, M.L., 1997, Application of perfectly matched layers to the transient modeling of subsurface EM problems: *Geophysics*, **62**, 1730–1736.
- Chew, W.C., and Weedon, W.H., 1994, A 3-D perfectly matched medium from modified Maxwell's equations with stretched coordinates: *IEEE Microwave and Optical Technology Letters*, **7**, 599–604.
- Day-Lewis, F.D., Lane, J.W., Harris, J.M., and Gorelick, S.M., 2003, Time-lapse imaging of saline tracer transport in fractured rock using difference radar attenuation tomography: *Water Resources Research*, **39**, 1290, doi:10.1029/2002WR001722.
- Deutsch, C.V., and Journel, A.G., 1992, *GSLIB: Geostatistical Software Library and User's Guide*: Oxford University Press.
- Ellefsen, K.J., and Wright, D.L., 2005, Radiation pattern of a borehole radar antenna: *Geophysics*, **70**, K1–K11.
- Ellefsen, K.J., 1999, Effects of layered sediments on the guided wave in crosswell radar data: *Geophysics*, **74**, 1698–1707.
- Eppstein, M.J., and Dougherty, D.E., 1998, Efficient three-dimensional data inversion: Soil characterization and moisture content monitoring from cross-well ground-penetrating radar data at a Vermont test site: *Water Resources Research*, **34**, 1889–1900.
- Ernst, J.R., and Holliger, K., 2005, Full-waveform inversion of crosshole georadar

- data: Proceedings of the 75th Annual Meeting of the Society of Exploration Geophysicists, Houston, TX.
- Ernst, J.R., Holliger, K., and Maurer, H., 2005, Realistic FDTD modelling of borehole georadar antenna radiation: methodology and application: Near Surface Geophysics, *In press*.
- Fang, J., and Wu, Z., 1996, Generalized perfectly matched layer for the absorption of propagating and evanescent waves in lossless and lossy media: IEEE Transactions on Microwave Theory and Techniques, **44**, 2216–2222.
- Fullagar, P.K., Livelybrooks, D.W., Zhang, P., and Calvert, A.J., 2000, Radio tomography and borehole radar delineation of the McConnell nickel sulphide deposit, Sudbury, Ontario, Canada: Geophysics, **65**, 1920–1930.
- Gedney, S., 1998, The perfectly matched layer absorbing medium, *in* Taflove, A., Ed., Advances in Computational Electrodynamics: The Finite-Difference Time-Domain Method: Artech House.
- Georgakopoulos, S.V., Birtcher, C.R., Balanis, C.A., and Renaut, R.A., 2002, Higher-order finite-difference schemes for electromagnetic radiation, scattering, and penetration, Part 1: Theory: IEEE Antennas and Propagation Magazine, **44**, 134–142.
- Goodman, D., 1994, Ground-penetrating radar simulation in engineering and archeology: Geophysics, **59**, 224–232.
- Greaves, R.J., Lesmes, D.P., Lee, J.M., and Toksoz, M.N., 1996, Velocity variations and water content estimated from multi-offset ground-penetrating radar: Geophysics, **61**, 683–695.
- Harris, F.J., 1978, On the use of windows for harmonic analysis with the discrete Fourier transform: Proceedings of the IEEE, **66**, 51–83.

- Holliger, K., and Bergmann, T., 2002, Numerical modeling of borehole georadar data: *Geophysics*, **67**, 1249–1257.
- Hubbard, S.S., Rubin, Y., and Majer, E.L., 1997, Ground-penetrating radar assisted saturation and permeability estimation in bimodal systems: *Water Resources Research*, **33**, 971–990.
- Hubbard, S.S., Chen, J., Peterson, J., Majer, E.L., Williams, K.H., Swift, D.J., Mailloux, B., and Rubin, Y., 2001, Hydrogeological characterization at the South Oyster Bacterial Transport Site using geophysical data: *Water Resources Research*, **37**, 2431–2456.
- Irving, J.D., and Knight, R.J., 2003, Removal of wavelet dispersion from ground-penetrating radar data: *Geophysics*, **68**, 960–970.
- Irving, J.D., and Knight, R.J., 2005a, Accounting for the effect of antenna length to improve crosshole GPR velocity estimates: *Proceedings of the 75th Annual Meeting of the Society of Exploration Geophysicists*, Houston, TX.
- 2005b, Effect of antennas on velocity estimates obtained from crosshole GPR data: *Geophysics*, **70**, K39–K42.
- Irving, J.D., and Knight, R.J., 2006a, Numerical modeling of ground-penetrating radar in 2-D using MATLAB: *Computers and Geosciences*, *In press*.
- 2006b, Numerical simulation of antenna transmission and reception for cross-hole ground-penetrating radar: *Geophysics*, **71**, K37–K45.
- Irving, J.D., Knoll, M.D., and Knight, R.J., 2006, Strategies for improving cross-hole GPR travel-time tomography at close borehole spacings: *In preparation for Geophysics*.

- King, R.W.P., and Smith, G.S., 1981, *Antennas in Matter: Fundamentals, Theory, and Applications*: MIT Press.
- King, R.W.P., Trembly, B.S., and Strohbehn, J.W., 1983, The electromagnetic field of an insulated antenna in a conducting or dielectric medium: *IEEE Transactions on Microwave Theory and Techniques*, **MTT-31**, 574–583.
- Kuzuoglu, M., and Mittra, R., 1996, Frequency dependence of the constitutive parameters of causal perfectly matched anisotropic absorbers: *IEEE Microwave and Guided Wave Letters*, **6**, 447–449.
- Lampe, B., and Holliger, K., 2005, Resistively loaded antennas for ground-penetrating radar: A modeling approach: *Geophysics*, **70**, K23–K32.
- Lampe, B., Holliger, K., and Green, A.G., 2003, A finite-difference time-domain simulation tool for ground-penetrating radar antennas: *Geophysics*, **68**, 971–987.
- Lesmes, D.P., Decker, S.M., and Roy, D.C., 2002, A multiscale radar-stratigraphic analysis of fluvial aquifer heterogeneity: *Geophysics*, **67**, 1452–1464.
- Liu, Q.H., and Fan, G., 1999, Simulations of GPR in dispersive media using a frequency-dependent PSTD algorithm: *IEEE Transactions on Geoscience and Remote Sensing*, **37**, 2317–2324.
- Liu, S., and Sato, M., 2005, Transient radiation from an unloaded, finite dipole antenna in a borehole: Experimental and numerical results: *Geophysics*, **70**, K43–K51.
- Luebbers, R.J., and Hunsberger, F., 1992, FDTD for Nth-order dispersive media: *IEEE Transactions on Antennas and Propagation*, **40**, 1297–1301.

- Maloney, J.G., Shlager, K.L., and Smith, G.S., 1994, A simple FDTD model for transient excitation of antennas by transmission lines: *IEEE Transactions on Antennas and Propagation*, **42**, 289–292.
- McMechan, G.A., Loucks, R.G., Mescher, P., and Zeng, X., 2002, Characterization of a coalesced, collapsed paleocave reservoir analog using GPR and well-core data: *Geophysics*, **67**, 1148–1158.
- Menke, W., 1984, The resolving power of cross-borehole tomography: *Geophysical Research Letters*, **11**, 105–108.
- Moghaddam, M., Yannakakis, E.Y., and Chew, W.C., 1991, Modeling of subsurface interface radar: *Journal of Electromagnetic Waves and Applications*, **5**, 17–39.
- Molyneux, J.B., and Schmitt, D.R., 1999, First-break timing: Arrival onset times by direct correlation: *Geophysics*, **64**, 1492–1501.
- Moran, M.L., and Greenfield, R.J., 1993, Radar signature of a 2.5-D tunnel: *Geophysics*, **58**, 1573–1587.
- Moysey, S., and Knight, R.J., 2004, Modeling the field-scale relationship between dielectric constant and water content in heterogeneous systems: *Water Resources Research*, **40**, W03510, doi:10.1029/2003WR002589.
- Moysey, S., Caers, J., Knight, R.J., and Allen-King, R.M., 2003, Stochastic estimation of facies using ground-penetrating radar data: *Stochastic Environmental Research and Risk Assessment*, **17**, 306–318.
- Oldenborger, G., Schincariol, R., and Mansinha, L., 2003, Radar determination of the spatial structure of hydraulic conductivity: *Groundwater*, **41**, 24–32.

- Olhoeft, G.R., 1988, Interpretation of hole-to-hole radar measurements: 3rd Symposium on Tunnel Detection, Proceedings, 616–629.
- Olsson, O., Falk, L., Forslund, O., Lundmark, L., and Sandberg, E., 1992, Borehole radar applied to the characterization of hydraulically conductive fracture zones in crystalline rock: *Geophysical Prospecting*, **40**, 104–116.
- Peraldi, R., and Clement, A., 1972, Digital processing of refraction data: Study of first arrivals: *Geophysical Prospecting*, **20**, 529–548.
- Peterson, J.E., 2001, Pre-inversion corrections and analysis of radar tomographic data: *Journal of Environmental and Engineering Geophysics*, **6**, 1–18.
- Pipan, M., Forte, E., and Finetti, I., 2002, Pre-stack processing of multi-fold GPR data to study the stratigraphy of shallow unconsolidated sediments: Proceedings of the 72th Annual Meeting of the Society of Exploration Geophysicists, Salt Lake City, UT.
- Powers, M.H., and Olhoeft, G.R., 1994, Modeling dispersive ground-penetrating radar data: Proceedings of the 5th International Conference on Ground-Penetrating Radar, 173–183.
- Pratt, R.G., and Gouly, N.R., 1991, Combining wave-equation imaging with travel-time tomography to form high-resolution images from crosshole data: *Geophysics*, **56**, 208–224.
- Pratt, R.G., and Worthington, M.H., 1988, The application of diffraction tomography to cross-hole seismic data: *Geophysics*, **53**, 1284–1294.
- Rector, J.W., and Washbourne, J.K., 1994, Characterization of resolution and uniqueness in crosswell direct-arrival travelttime tomography using the Fourier projection-slice theorem: *Geophysics*, **59**, 1642–1649.

- Roden, J., and Gedney, S., 2000, Convolution PML (CPML): An efficient FDTD implementation of the CFS-PML for arbitrary media: *IEEE Microwave and Optical Technology Letters*, **27**, 334–339.
- Sato, M., and Thierbach, R., 1991, Analysis of a borehole radar in cross-hole mode: *IEEE Transactions on Geoscience and Remote Sensing*, **29**, 899–904.
- Scales, J.A., 1987, Tomographic inversion via the conjugate gradient method: *Geophysics*, **52**, 179–185.
- Sengupta, D.L., and Liu, Y., 1974, Analytical investigation of waveforms radiated by a resistively loaded linear antenna excited by a Gaussian pulse: *Radio Science*, **6**, 621–630.
- Sengupta, D.L., and Tai, C.T., 1976, Radiation and reception of transients by linear antennas, *in* Felsen, L.B., Ed., *Transient Electromagnetic Fields*: Springer.
- Shlivinski, A., Heyman, E., and Kastner, R., 1997, Antenna characterization in the time domain: *IEEE Transactions on Antennas and Propagation*, **45**, 1140–1149.
- Smith, G.S., 1997, *An Introduction to Classical Electromagnetic Radiation*: Cambridge University Press.
- Smith, G.S., 2001, Teaching antenna radiation from a time-domain perspective: *American Journal of Physics*, **69**, 288–300.
- Smith, G.S., 2004, A direct derivation of a single-antenna reciprocity relation for the time domain: *IEEE Transactions on Antennas and Propagation*, **52**, 1568–1577.
- Squires, L.J., Blakeslee, S.N., and Stoff, P.L., 1992, The effects of statics on tomographic velocity reconstructions: *Geophysics*, **57**, 353–362.

- Sudicky, E.A., 1986, A natural gradient experiment on solute transport in sand aquifers: Spatial variability of hydraulic conductivity and its role in the dispersion process: *Water Resources Research*, **22**, 2069–2089.
- Taflove, A., 1995, *Computational Electrodynamics: The Finite-Difference Time-Domain Method*: Artech House.
- Teixeira, F.L., and Chew, W.C., 1997, Systematic derivation of anisotropic PML absorbing media in cylindrical and spherical coordinates: *IEEE Microwave and Guided Wave Letters*, **7**, 371–373.
- Teixeira, F.L., Chew, W.C., Straka, M., Oristaglio, M.L., and Wang, T., 1998, Finite-difference time-domain simulation of ground-penetrating radar on dispersive, inhomogeneous, and conductive soils: *IEEE Transactions on Geoscience and Remote Sensing*, **36**, 1928–1936.
- Tronicke, J., and Holliger, K., 2004, Effects of gas- and water-filled boreholes on the amplitudes of crosshole georadar data as inferred from experimental evidence: *Geophysics*, **69**, 1255–1260.
- Tronicke, J., Dietrich, P., and Appel, E., 2001, Improved crosshole radar tomography by using direct and reflected arrival times.: *Journal of Applied Geophysics*, **47**, 97–105.
- Tronicke, J., Dietrich, P., Wahlig, U., and Appel, E., 2002, Integrating surface georadar and crosshole radar tomography: A validation experiment in braided stream deposits.: *Geophysics*, **67**, 1516–1523.
- Tronicke, J., Holliger, K., Barrash, W., and Knoll, M.D., 2004, Multivariate analysis of cross-hole georadar velocity and attenuation tomograms for aquifer zonation: *Water Resources Research*, **40**, W01519, doi:10.1029/2003WR002031.

- Turner, G., and Siggins, A.F., 1994, Constant Q attenuation of subsurface radar pulses: *Geophysics*, **59**, no. 8, 1192–1200.
- VanDecar, J., and Crosson, R., 1990, Determination of teleseismic relative phase arrival times using multi-channel cross-correlation and least squares: *Bulletin of the Seismological Society of America*, **80**, 150–159.
- Vasco, D.W., Peterson, J.E., and Lee, K.H., 1997, Ground-penetrating radar velocity tomography in heterogeneous anisotropic media: *Geophysics*, **62**, 1758–1773.
- Wang, T., and Tripp, A.C., 1996, FDTD simulation of EM wave propagation in 3-D media: *Geophysics*, **61**, 110–120.
- Williamson, P.R., and Worthington, M.H., 1993, Resolution limits in ray tomography due to wave behaviour: *Geophysics*, **58**, 727–735.
- Woodward, R.L., and Masters, G., 1991, Global upper mantle structure from long-period differential arrival times: *Journal of Geophysical Research*, **96**, 6351–6377.
- Wu, T.T., and King, R.W.P., 1964, The cylindrical antenna with nonreflecting resistive loading: *IEEE Transactions on Antennas and Propagation*, **AP-12**, 369–373.
- Xu, T., and McMechan, G.A., 1997, GPR attenuation and its numerical simulation in 2.5 dimensions: *Geophysics*, **62**, 403–414.
- Yee, K.S., 1966, Numerical solution of initial boundary value problems involving Maxwell's equations in isotropic media: *IEEE Transactions on Antennas and Propagation*, **14**, 302–307.
- Zeng, X., McMechan, G.A., Cai, J., and Chen, H.W., 1995, Comparison of ray and Fourier methods for modeling monostatic ground-penetrating radar profiles: *Geophysics*, **60**, 1727–1734.

Zhou, C., Cai, W., Luo, Y., Schuster, G., and Hassanzadeh, S., 1995, Acoustic wave-equation travelttime and waveform inversion of crosshole seismic data: *Geophysics*, **60**, 765–773.